

Hydro-morphological Study of Braided River with Permeable Bank Protection Structure

A dissertation submitted in partial fulfilment for the requirement of
Doctoral Degree in Civil and Earth Resources Engineering

By

Shampa

Supervised by Prof. NAKAGAWA Hajime



Laboratory of Hydrosience and Hydraulic Engineering

Department of Civil and Earth Resources Engineering

Graduate School of Engineering

Kyoto University

March 2019

Abstract

Braided rivers are characterized by simultaneous reworking of numerous channels and bars as an adjustment of the variable discharge and sediment load during a flood. Very rapid bed deformation process during the flooding time induces major changes in area, shape and spatial distribution of the major morphological features (bar and channels) of the river. These processes add uncertainty in the management of river induced disasters e.g. bank erosion. Moreover, the flow features produced by any countermeasure of riverbank erosion sometimes lead to unexpected bed deformation through local scouring which ultimately ended up by the failure of the structure. Hence, prior to any intervention in such type of river, a proper understanding of the bed deformation phenomena of the river reach, as well as the flow modification induced by the structure, should be the key river management issue for the braided river system.

Diverse types of mid-channel bars add uniqueness to the braided river system. But the responses of all types of bar especially the compound type of bars are not extensively investigated previously. As an example, the bifurcations play a major role in shaping the braided river system, the previous studies of bifurcation comply simplification of bifurcation unit by not considering the property of mid-channel bars. But the properties and erosiveness of a bank attached channel can be controlled by maintaining the bifurcation unit. On the contrary, there exist many failure examples of river bank protection structures in the sand-bed braided river only due to inadequate design because of the poor understanding of local flow field. Therefore, in this research attempts have been made firstly to understand the bed deformation process of a compound bar dominated sand-bed braided river. Consequently, optimal countermeasures for riverbank erosion “slit type spur dike field” have been suggested and the performance of this type of structure has been examined both experimentally and numerically. Nevertheless, the possibility of the management of bank attached channel through controlling the bifurcation unit has also

checked. And lastly the applicability of the “slit type spur dike field” has been checked in a small river reach of a sand-bed braided river.

In this study, two numerical models have been developed based on an open source library to predict the bed and flow feature. One is a two-dimensional morphology model and another is a three-dimensional hydrodynamic model. The performance and application of these models have also been tested by experiments and real field data during this study.

The bed evolution of braided river has been investigated by developing a model which solves a two-dimensional form of Navier-Stokes equations for incompressible free surface flow coupled with sediment transport and one-dimensional bed sorting. The adjustment of river bed due to unsteady flow for one wet period has been investigated in a compound bar dominated reach of Brahmaputra-Jamuna River. The study indicates that the frequency of deposition on the river bed or braided plain is higher compared to the erosion due to unsteady change of flow boundary conditions. The development processes of the braided bars are quite different from the bars of straight and meandering channels. The spatial growth of the bars seem to be dependent on the width-depth ratio of the river up to a certain range and the migration rate of the bar recedes with the spatial growth of the bar.

Assuming highly permeable spur dike will induce lowest flow modification “slit type” spur dike field is proposed and the suitability of different arrangements of permeable pile spur dike fields, laboratory experiments were conducted. Along with this a three-dimensional multiphase numerical model was developed using 3D RANS coupled with $k-\omega$ SST turbulence closures and the VOF method. Three types of angles of attack to the approach flow and two types of individual pile position arrangements were tested. It is observed that when using a highly permeable (slit-type) spur dike as a field, the approach velocity of flow can be reduced by a considerable amount within the spur dike zone. Using a different set of angle and installation positions, this type of permeable spur dike can be used more efficiently. The attractive type of spur dike is well suited for reducing the longitudinal velocity, turbulence intensity and bed shear stress in the near-bank area. It was also found that the deflecting type of permeable spur produces more transverse flow to the opposite bank. Arranging the pile in a staggered grid position within different spurs in a

spur dike field produces better functionality of the spur dike field by creating a quasi-uniform turbulence zone and reducing the bed shear stress.

The natural switching of bifurcation unit to a single channel has been analyzed using the above mentioned 2D model. Using several synthetic hydraulic conditions, triggering condition of switching phenomenon and the relationship with the mid-channel bar has been investigated. In the sanded braided river like Brahmaputra-Jamuna the cross-sectional variation of the water level has been observed but in case of switching this variation does not have any effect. The geometry of the upstream channel prior to bifurcation plays the major role in switching by distributing the discharge. However, the characteristics of mid-channel bar seem indirectly affect the switching but the geometry of the upstream channel influence greatly by the properties of mid-channel bar.

Lastly, the effectiveness of the structural countermeasure has been tested in a small river reach of Brahmaputra-Jamuna using the peak flood discharge by means of the above mentioned 3D model. This study indicates that in this type of river the transverse velocity induced by the structure is high enough to initiate the local erosion. Using this type of 3D model the area of the high velocity induced by the detached shear layer (DSL) can be identified. Therefore, this model can be used as an investigation tool for local flow problems with its capability of treating complex geometries and precise prediction of the free surface.

Keywords: braided river, bed deformation, compound bar, Slit-type permeable spur; Alluvial rivers; 3D RANS; $k-\omega$ SST; Multiphase flow; Turbulent flow.

Acknowledgments

I would like to express my sincere gratitude and acknowledge the enthusiastic supervisor Prof. Hajime NAKAGAWA, Disaster Prevention Research Institute (DPRI), Kyoto University who turns my mind to ‘scientific thinking’. He enlightens me by his thoughtful guidance, continuous encouragement and supports in a wide aspect which makes my study at Kyoto University extremely meaningful.

I am deeply grateful to my thesis reviewer, Associate Professor Dr. Hiroshi TAKEBAYASHI, DPRI, Kyoto University, for his valuable comments and suggestions to refine the thesis. I am also thankful to Associate Professor Dr. Kenji KAWAIKE, DPRI, Kyoto University, for his academic guidance during the research as well as comments and suggestions to refine the thesis.

Special thanks go to Associate Professor Dr. Yuji HASEGAWA, Hiroshima University for his excellent suggestions and guidance during the research. The Bangladesh Water Development Board (BWDB) and Center for Environmental and Geographic Information Services (CEGIS), Dhaka, Bangladesh are also acknowledged for support in data collection.

Thanks go to all of my friends of Ujigawa Hydraulics Laboratory who helped me to finish this work and made my life joyful during the experiments and simulation process. I am also thankful to my colleagues and students in the Institute of Water and Flood Management (IWFM) of Bangladesh University of Engineering and Technology (BUET) for their administrative support during the field data collection.

I am sincerely gratitude towards my little son Md. Arham Bin Asad who missed his mom a lot during her tough research days. Lastly, I am thankful to the Almighty for everything towards the completion of this research journey.

Table of Contents

Abstract.....	i
Acknowledgments.....	v
Table of Contents.....	vi
Chapter 1 Introduction.....	1
1.1 Background.....	1
1.2 Classifications of rivers.....	3
1.3 Key features of the braided river system.....	6
1.4 Research Problems and Objectives.....	8
1.5 Study Area.....	9
1.5.1. Flow and Sediment Regime.....	10
1.5.2. Bedform and Planform.....	13
a) Bedform.....	13
b) Planform Characteristics.....	15
1.6 Outline of the Dissertation.....	17
Chapter 2 Bed evolution process of the braided river network.....	19
2.1 Numerical modeling of braided rivers.....	19
2.2 Two dimensional morphodynamic model of bed evolution.....	22
2.2.1 Governing Equations.....	22
a) Hydrodynamic Equations.....	22
b) Sediment Transport Equations.....	23
c) Bed change.....	28
d) Discretization methods.....	31
2.2.2 Model Schematization.....	34
a) Bathymetry and Mesh generation.....	34
b) Boundary conditions.....	35
c) Model calibration and validation.....	38
2.3 Results and Discussions.....	39
Methods of Analysis.....	39

	a) Overall bed evolution and planform changes.....	42
	b) Migration of bars.....	44
	c) Location of bank erosion.....	45
	d) Bar properties.....	45
2.4	Summary.....	50
Chapter 3	Riverbank protection measures for braided river network.....	52
3.1	Problem identifications and countermeasures	52
3.2	Laboratory experiments with slit type permeable spur dikes	58
3.2.1	Experimental Set-up.....	58
3.2.2	Measurement techniques.....	61
3.2.3	Results and Discussions.....	62
	a) Longitudinal Velocity	62
	b) Transverse Velocity	64
	c) Flow Depth.....	65
3.3	Three dimensional numerical model for experimental results.....	68
3.3.1	Governing equations	68
3.3.2	Discretization Procedure.....	72
3.3.3	Pressure-Velocity Solution Procedure	75
3.3.4	Rough Wall Treatment.....	77
3.3.5	Model schematizationin	79
3.3.6	Model verification.....	80
3.3.7	Results and Discussions.....	84
	a) Longitudinal and Transverse velocity	84
	b) Spatial Velocity.....	84
	c) Reynolds Stresses: Consideration for Sediment Transport	89
	d) Bed Shear Stress	92
3.4	Non-structural measures of bank protection for braided network	94
3.4.1.	Managing the bifurcation to control bank attached channels.....	94
3.4.2.	Two dimensional Morphodynamic model of bifurcation	96
3.4.3.	Results and Discussions	98
	a) Switching of channel.....	98

b)	Relation between bifurcation switch and upstream channel geometry and hydraulic condition.....	99
c)	Bifurcation switch and downstream mid channel bar	101
3.5	Summary	104
Chapter 4	Field application of slit type permeable spur dike in Brahmaputra-Jamuna..	106
4.1	Background.....	106
4.2	Model Schematization	107
4.3	Boundary conditions	110
4.4	Results and Discussions.....	112
4.4.1	Longitudinal velocity	112
4.4.2	Transverse velocity	114
4.4.3	Dam-up	114
4.5	Summary	116
Chapter 5	Conclusions and recommendations	118
5.1	Conclusions.....	118
5.2	Recommendations for future study.....	121
Reference	123
List of Tables	134
List of Figures	135
List of symbols.....	139
Acronyms and abbreviations.....	145
Curriculum Vitae	147
Paper based on the Thesis	148

Chapter 1

Introduction

1.1 Background

Rivers by transporting the water and sediment from their catchments to the sea, form one of the most dynamic systems of the hydrosphere of the earth. While flowing, the water and sediment interact and being influenced by several physical factors i.e. the bed, banks, slope which result in diverse planforms (Fig.1.1). As the human life has been dependent on the river on various aspects e.g. sweet water, food, navigation from ancient ages, the behavior of various types of rivers and their response to any intervention intrigued scientists and engineers from the primeval time to present (Filip Schuurman 2015). On the other hand, the disasters caused by the river (e.g. flooding, avulsion, bank shifting) sometimes triggered serious devastation to the nearby civilization (Fig.1.2). Therefore, the scientific and engineering societies always try to maximize the benefits of the river and reduce the negative aspects of rivers which needs an intense understanding of the river dynamics (catchment or very long reach scale) as well as river response to any interventions (local reach scale) (Williams et al. 2016).

This study focuses the management of one of the major negative impact produced by several types of the river (braided type is considered in this study) - “river bank erosion” through the understanding of the morphodynamics of a long river reach and local flow modification induced by the hydraulic structure. Laboratory experimentations and numerical simulations have been used as the methodology of the study. In the following sections, a short literature review about the topic is presented and followed by the specific research questions.



Fig.1.1 Satellite image of the Rio Negro, Branco and Unini River representing the different distinct planform of the river nearly in the same location (location: Manaus, Brazil, Oct 2018)



Flooding and landslides have killed at least 60 people in western areas of Japan at mid-July, 2018 (source BBC)



Homeless at the age of 70 due to Sevier erosion of river bank of Brahmaputra-Jamuna in 2018 (P.C.: Gbm Akash)

Fig.1.2 Negative impact caused by river in different parts of the world in 2018

1.2 Classifications of rivers

A variety of types of the river are seen on the earth depending on the nature of the bed and bank materials, planform, temporal discharge variations, and sediment transport characteristics (Schumm 1960). River pattern and fluvial process evolved simultaneously through mutual adjustment unless they attain a self-stabilization state which results diverse planform (Rosgen 1994). An example of such different planform rivers in similar place of Brazil is shown in Fig.1.1. Although the basic physics governing the formation of a channel of a great river are the same that form a tinny one; different types of rivers are seen in the world based on external (e.g. catchment characteristics) and internal factors (e.g. channel geometry) (Leopold, L. B., Wolman 1957). However, the scientists tried to classify the river system based on their planform and characteristics. Leopold and Wolman (1957) classified the river into three major category – straight, meandering and braided based on planform. Brice et al. (1978) further enhanced this classification based on channel magnitude of sinuosity, the degree of braiding, types of anabranching and proposed twenty-five distinctly classified river system. The classification provided by Brice et al. (1978) connects a great range of hydrology, transport characteristics, and planform of the rivers of the world. Schumm (1963, 1985) further modified the classification from suspended load-dominated to bedload-dominated, from small to large width/depth ratios and high to low planform stability which is presented in

Fig.1.3 merging the anabranching rivers to the main three subthemes. Nanson and Knighton (1996) showed that when the bivariate plot of bankfull discharge and channel slope were plotted; the anabranching types do not significantly differ from the single thread one. Basically, by building anabranching system when there is no or little to increase the gradient, the river maximize the flow and transport (work per unit area)(Nanson and Knighton 1996). An example of braided and meandering anabranching river is shown in Fig.1.4. The bivariate plot of bankfull discharge and channel slope used by several researchers (i.e. (Leopold and Wolman 1957b; Nones and Di Silvio 2016; Simpson and Smith 2001)) are plotted in Fig.1.5. The Leopold-Wolman's morphological parameter, Ω ($= s * Q^{.44}$) was used to determine the river pattern here. If the Ω goes larger than 0.012 the meandering river tend to braiding while larger the value of Ω (0.046) inclines to be straight from braiding.

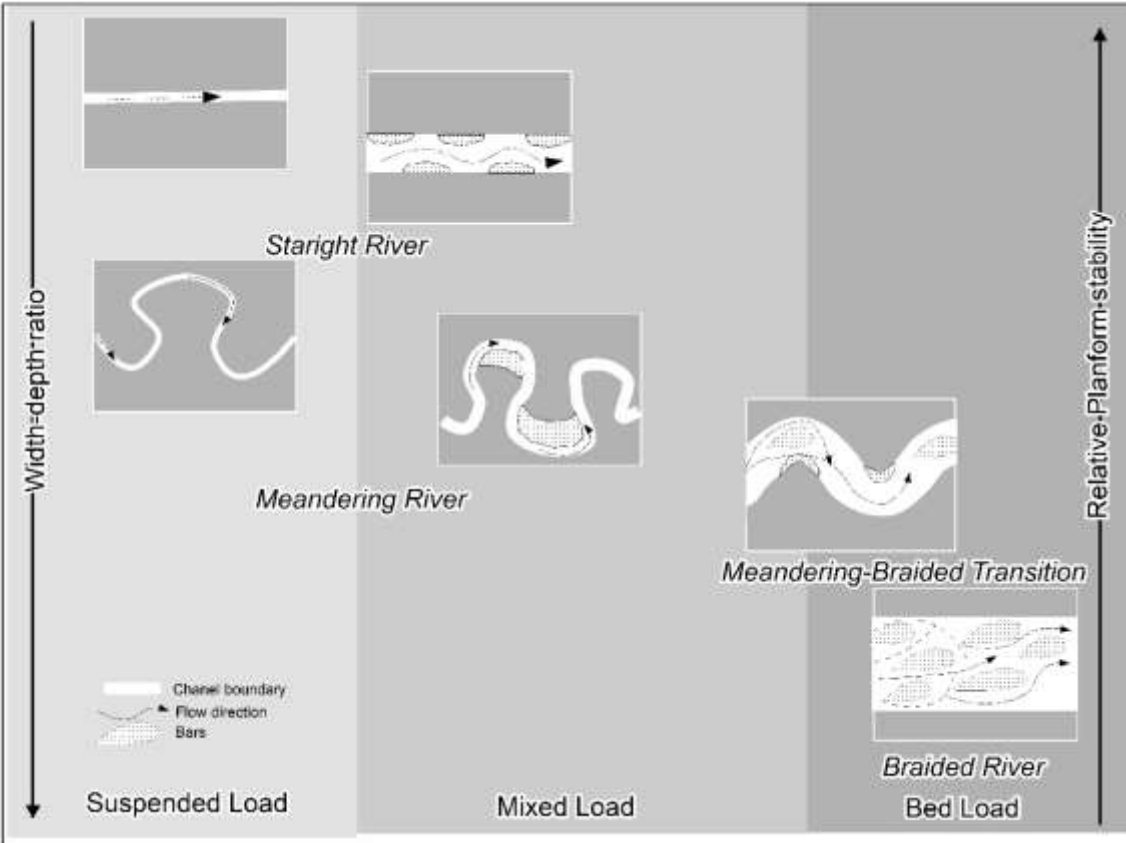


Fig.1.3 Classification of the river [based on Schumm (1963, 1985)]

Furthermore, in the Fig. 1.3, the distinction between the suspended, mixed and bedload dominancy is made based of the percentage bedload over the total load. If the percentage of bed load is $<3\%$ then the river falls into the suspended load category. The channel pattern in this zone is deep, bank-stable “straight channel” and small-width sinuous “meander”. The channels fell in this zone usually carries small amount of coarse sediment. The banks are relatively stable through the neck cut-off at meander bends are visible.

In the mixed load zone (the percentage of bed load varies from 3% to 11%) zone several channel patterns are observed. In the case of “mixed-load straight channel”, sinuous thalweg is observed and the river carries small load of coarse sediment which may move as alternate bars. In this zone “less stable meander” is seen with high channel width and alternate bend. The width of the channel tends to be wider at bend and point bars become larger. When the sediment loads become larger the transition of “meandering –braided” starts. The channel width becomes adaptable but relatively large compared with the depth

(high width-depth ratio) for this type of river. Chute cutoffs, meander shift, and bank erosion are all typical phenomenon of this pattern. Nonetheless, at this stage, the bars and islands modify the flow and bank erosion alignment.

In highly bedload dominated zone (bed load >11% of total load) the bar braided system is formed. The bars and thalweg shifts within the unstable banks frequently. Banks are easily erodible and bars and islands easily form and migrate throughout the channel. Avulsion becomes very common for this type of rivers. Another type of braiding- island-braiding which is relatively stable than the bar-braided system is also seen in some parts of the world (i.e. the Mississippi River before the confluence of the Missouri River).



Fig.1.4 Anabranching in braided (left: Brahmaputra-Jamuna River, Bangladesh) and meandering (right: Upper Meghna River, Bangladesh) river

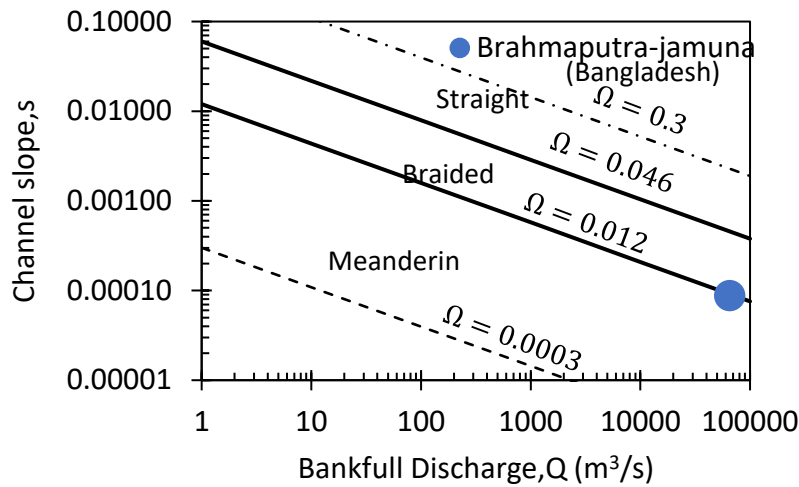


Fig.1.5 Discharge-slope relationship to identify the river pattern [after (Leopold and Wolman 1957a; Nones and Di Silvio 2016; Simpson and Smith 2001)]

1.3 Key features of the braided river system

Braided river is characterized by networks of channels splitting around bars and islands. Ashmore (1982, 1991) identifies six key unit processes governing the formation and development of the braided network. Nowadays the major morphological elements of a braided river e.g. bifurcation-confluence unit, several types of bars and channels can be easily identified from the satellite images of that river.

Fig.1.6 shows different elements of braided stream of a sand-bed braided river. Laboratory experiments with erodible banks confirm the role of initial bar formation in braided channel pattern development (Ashmore 1982; Bertoldi et al. 2009; Federici and Paola 2003; Fujita & Muramoto 1982; Ikeda 1984(based on earlier Japanese work of Kinoshita and others); Jang and Shimizu 2005). In general, the unit bars migrate in downstream direction by upstream erosion and deposition at their lee but the actual migration of compound bar is difficult to predict as they may interact and merge with other unit or compound bars or may be bisected by several channels (Schuurman et al. 2013; Shampa et al. 2017a).

Another important characteristic of the braided river is the bifurcation-confluence unit formed by the mid-channel bars or islands. Bifurcations act as the key element for



Fig.1.6 Major morphological element of the braided river (sand-bed, Brahmaputra)

distribution of the flow and sediment along the braided network (Klaassen et al. 1993; Kleinhans et al. 2012). Switching of bifurcation to the single channel may create a scope to merge multiple bars to form a new compound bar or new bifurcation splits old bars by creation or chute channels. These process may strongly affect the location of river bank erosion. The previously developed simple model of bifurcation (e.g. Bolla Pittaluga et al. (2003); Kleinhans et al. (2006); Wang et al. (1995)) were based on the simple distribution of sediment and flow did not consider the bar properties of an actual braided river.

Every process regarding the braided mechanism may affect the bank attached channel and cause the river bank erosion. In spite of huge progress of satellite image-based analysis and numerical analysis, still, the braided river is regarded the complicated and unpredictable to some extent (Klaassen et al. 1993; Schuurman et al. 2013).

1.4 Research Problems and Objectives

As described in the earlier paragraphs the process of adjustment of braiding to the flow induce frequent channel shifting and bar migration. This phenomenon may affect human life by causing bank erosion. As an example the Brahmaputra-Jamuna in Bangladesh itself erodes the river bank by 17.05 sq km/y for the last four decades and creates thousands of people homeless (Fig.1.7) (Bryant and Mosselman 2017). Any intervention in the braided river to protect the river bank especially in the sand-bed one induce huge modification of flow. Even the hydraulic structure can fail within the design discharge range due to the local variability of flow and the bed variation caused by the river (Nakagawa et al. 2013). Hence for the proper design of hydraulic structure, the understanding of the dynamic bed variation is crucial. Along with this such type of hydraulic structure should be selected which will produce lower bed shear stress. Based on these circumstances the following research questions have been addressed in this research:

How the river evolve its bed in a compound bar dominated reach of a sand-bed braided river due to monsoon flood? Is it possible to use the river key characteristics to manage the river? What is the best possible eco-friendly countermeasures of river bank erosion for the braided river?

Hence, the major objectives of this research is

- (1) Characterize the bed evolution induced by seasonal flood and quantify the interaction processes of flow and river morphology.

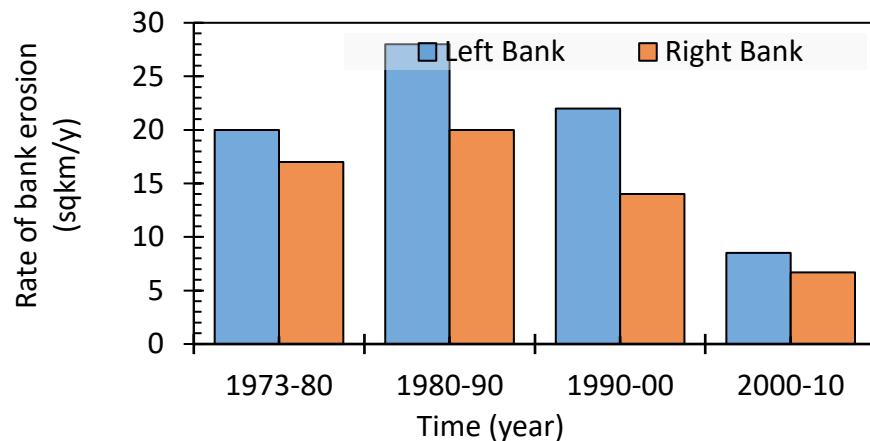


Fig.1.7 The decadal bank erosion of Brahmaputra-Jamuna River, Bangladesh

- (2) Assess the practicability of the permeable hydraulic structure as a bank protection measure and characterize the flow structure induced by permeable spur dikes.
- (3) Develop numerical models that can replicate the real scale spur-dike-induced flow properties in the braided river.

1.5 Study Area

As mentioned above the major focus of this study is to understand the behavior of a braided type of river and effectively manage the river in a sustainable manner. Hence as a study area a 225 km long river reach of sand-bed Brahmaputra river (downstream continuation of the Brahmaputra River in Bangladesh, see Fig. 1.8) was selected. The river is well known for its extremely dynamic nature, with high sediment transport rate, 550 m ton/y (Baki and Gan 2012; DHI and Hydraulics 1996; Sarker et al. 2014). The morphological features of the river (bars and channels) experience major changes in area, shape and spatial distribution each year to respond the variation of discharge and sediment load during the floods (annual fluctuation of discharge is more than 60,000 m³/s, see Fig.1.9)(Sarker et al. 2014).

The Brahmaputra-Jamuna is an international river draining almost 712,035 km² of China, India and Bangladesh prior to meet the Bay of Bengal (Jagers 2003). Being originated from Chemayungdung glacier of the Himalayas at altitude 5100 m from the mean sea level (MSL); the river flows about 1400 km in an easterly direction across the Tibetan plateau as Yarlung River then it descends to 3000 m MSL. At an altitude of 200 m MSL, it leaves the Himalayan range as the Dihang River and enters in Assam province of India taking its name as the Brahmaputra. The river flows to the west and near the international border between India and Bangladesh at the ninety degrees east meridian, it makes a sharp left turn, goes south and enters Bangladesh from where the river is known as the Brahmaputra-Jamuna in Fig. 1.8.

Then after flowing nearly 225 km within Bangladesh, it meets with the Ganges River and the combined flow named as the Padma which discharges to the Bay of Bengal. In this study, the river reach named as “Brahmaputra-Jamuna” (after entering to Bangladesh and prior to the confluence with the Ganges) is considered as the study region.

The hydro-morphological characteristics of this reach have been described in the next paragraphs.

1.5.1. Flow and Sediment Regime

The study reach contains only 8.1% of the total catchment area of the whole Brahmaputra River (almost 712,035 km²) which receives an average of 1900 mm rainfall year⁻¹ (Gupta 2007). The mean daily discharge varies from 5000 m³/s (during Dry season) to 50000 m³/s (during wet season) (Fig.1.9).

The average bed slope within the study reach of this river is 7.5 cm/km (Sarker 2008). In fact, bed slope varies from the upstream to the downstream reach within the study reach e.g. low water surface slope is varying between 8.8 cm/ km to 5.9 cm/km as shown in Fig.1.10 within the different water level measuring stations (the location of water level measuring station are shown in Fig.1.8)(Shampa 2015).

Similar to the bed slope, the size of the bed material also varies as the river flows to the downstream direction (Kabir and Ahmed 1996). As the river possess very active bed form, during downstream propagation of the bed or sand dune, the size of the transported sediment was found to be finer during the aggradation phase and coarser during the degradation phase (Bartley and Rutherford 2005). However, the time series distribution data of sediment size was sparser. FAP 24 (1996) collected 138 samples of bed material at Bahadurabad and Sirajganj which is listed in the first column of Table 1.1. Their measurement indicated that the range of mean sediment diameter, d_{50} of the river, varies from 304 to 221 μm . The other researchers mentioned the variation of d_{50} ranges from 40 to 250 μm (Goswami 1985; Nakagawa et al. 2013; Sarker 2008). Fig.1.11 showed an example of recent sediment size distribution curve measured at Sirajganj station which also indicates the mean sediment diameter of 150 μm . Due to such variation of sediment size difficulties arises to accurate prediction of vertical bar profile and channel bathymetry.

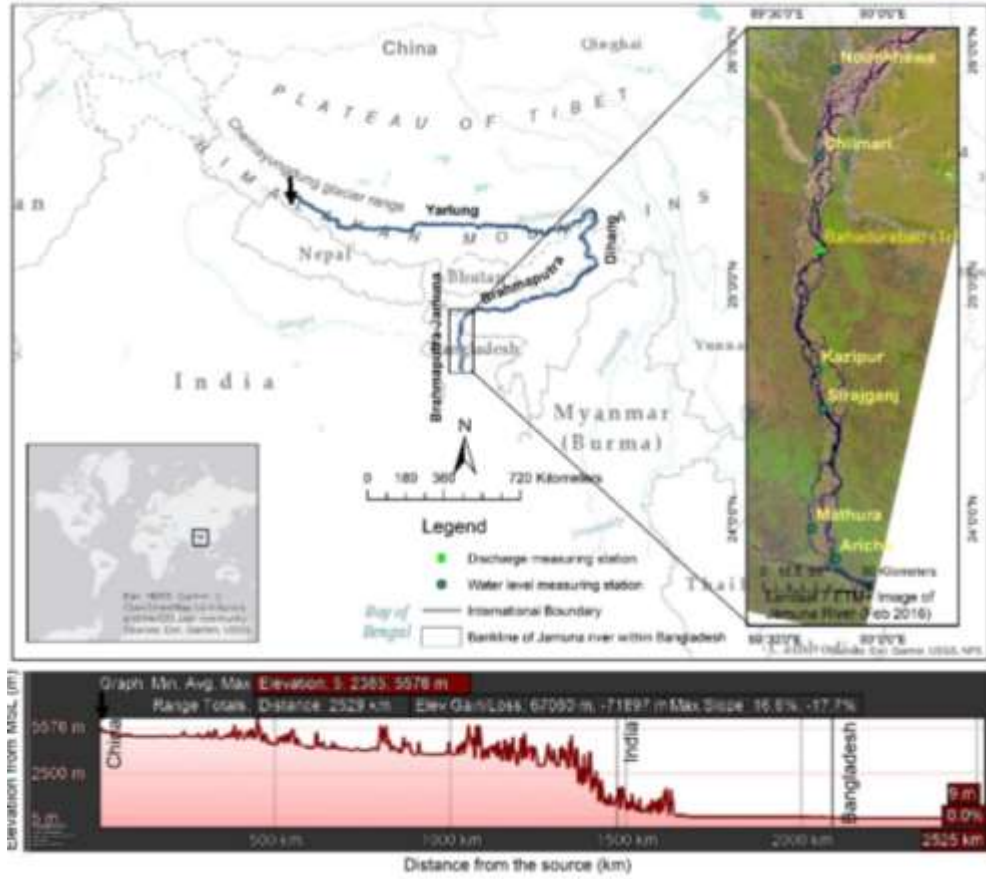


Fig.1.8 Map showing the study area (elevation data courtesy: Google Earth Pro v7.3.2.5491)

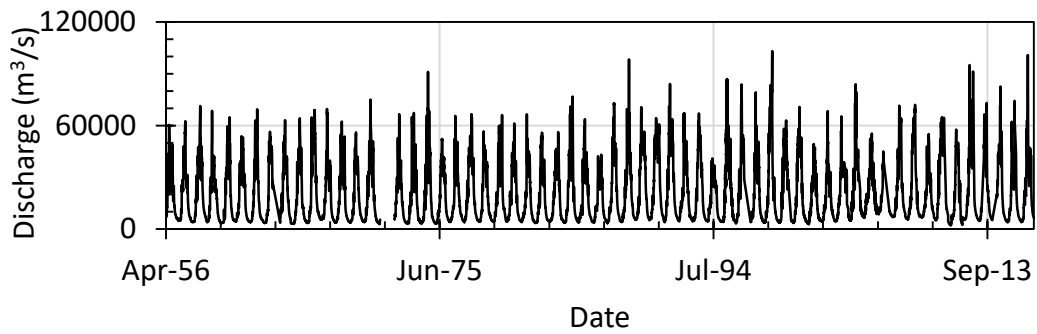


Fig.1.9 Time series representation of mean daily discharge of Brahmaputra-Jamuna at Bahadurabad station from the year 1956 to 2016

Table 1.1 The sediment size d_{50} of Brahmaputra-Jamuna

Time in 1993	FAP 24 (1996)	Sarker (2008)	Goswami (1985)	Coleman (1969)	Nakagawa et al. (2013)
Jan	304				
Feb	241				
Mar	221				
Apr	-				
May	-				
Jun	265	200	40	250	150
Jul	254				
Aug	273				
Sep	274				
Oct	272				
Nov	272				
Dec	271				

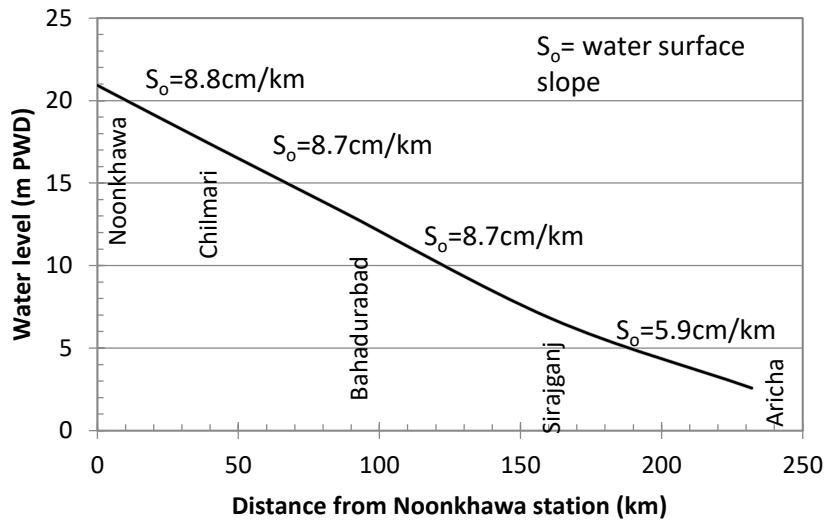


Fig.1.10 Average water surface slope at the date of the annual minimum water level [after (Shampa 2015)]

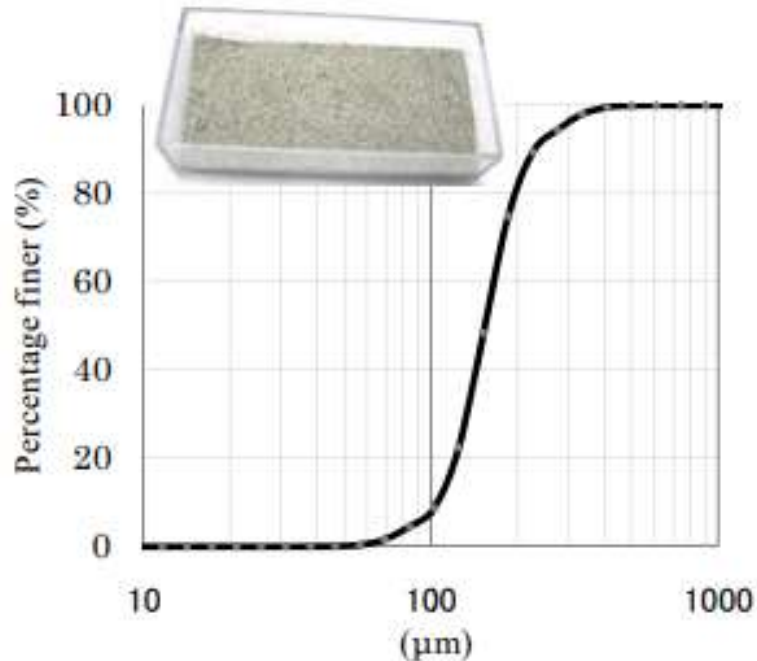


Fig.1.11 Sieve analysis of sediment sample at Sirajganj [after Zhang et al. (2011)]

1.5.2. Bedform and Planform

a) Bedform

Like all other alluvial rivers, the sediment is carried as the bed, suspended and wash load in the study river reach. However, the previous researchers indicated that the bed load, although whose fraction is only 10 % of the total sediment load, is crucial in generating a wide range of bedforms of different scale (Klaassen and Vermeer 1988). This acts as an external driving force of planform alteration. Generally, the transport of bed load occurs at all flow stages in the hydrograph of Brahmaputra-Jamuna River but the reworking or modification of the high-stage deposits becomes significant on the falling limb of the flood (Best 2005).

Among the smaller-scale bedforms, e.g. ripples and dunes; dunes are the main component of bedform within the river reach found in all flow stages (FAP 24 1996; Roden 1998). Sometimes this type of smaller bedform or their super-imposed form act as the nucleus of large bars (Best et al. 2003a). Best et al. (2006) mentioned the occurrence of

more than 40% of dunes over the bed near Bahadurabad and Sirajganj stations at any flow stages. The superimposing of ripples and smaller dunes are seen frequently but upper-stage plane beds are rare and found only on shallow flow zone on bar-tops. Dune height and wavelength range from 0.10 to 6 m and 2 to 331 m respectively. Fig.1.12 shows an example of typical bedform of the river. Several types of dunes ranges from 0.33 m to 2.3 m during May 2011 can be seen from this figure.

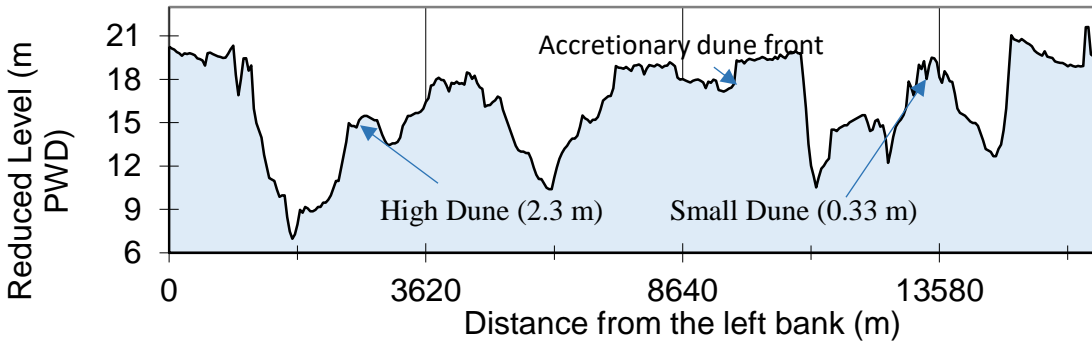


Fig.1.12 The bedforms along the cross-section of Bahadurabad station in May 2011

The large-scale bedforms - bars and islands found from 3 m to 15 km in length and with heights up to the adjacent floodplain level. According to the process of development, the bars of the Brahmaputra-Jamuna can be divided into two categories, compound bar and unit bar as shown in Fig.1.13 by CB and UB respectively. Compound bars are more frequent in the study reach compared to the unit ones. Though most of these compound and unit bars are free mid-channel bars, some forces bars are also found (as shown by FB in Fig.1.13). Generally, the bar dimensions depend on the width-depth ratio of the braided-plain, as revealed by many field observations, laboratory experiments, and linear analyses (Ashmore 1982; Ikeda and Parker 1989; Mosley 1983; Fujita & Muramoto 1982; Yalin 1992; Ashworth et al. 2011; Best et al. 2003, 2006). At a high width-depth ratio (like Brahmaputra-Jamuna) strong braiding initiates and midchannel bars form spontaneously from minor perturbations in the bed (Fujita Y. 1989; Ashmore 1991; Schuurman et al. 2013). On the other hand, lower width-depth ratio encourages weak braiding usually by chute cutoffs (Ashmore 1991; Federici and Seminara 2003; Bertoldi et al. 2009b; Kleinhans and van den Berg 2011; Schuurman et al. 2013).

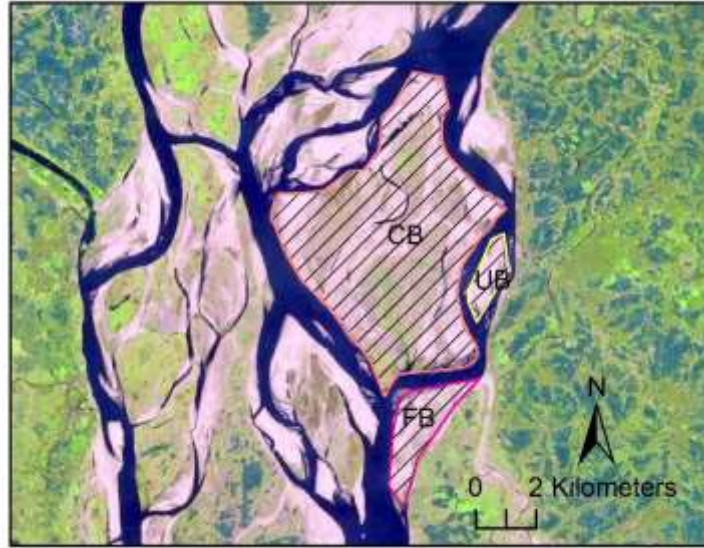


Fig.1.13 Examples of different types of the bar in Brahmaputra-Jamuna. CB: compound bar, UB: Unit bar and FB: Forced bar [after Shampa et al. (2017)]

b) Planform Characteristics

Several studies (Best et al. 2007; Goodbred and Kuehl 2000; Umitsu 1993) revealed the long-term development of the river. Significant century-scale change of the river is the gradual westward migration of the braided-belt of the river shown in Fig.1.14. It indicated that in the 1830s the Brahmaputra-Jamuna River had a thinner width and followed a course that was for most likely to the present east (left) bank. During the 1910s the river had shifted noticeably westward and the average width of the channel became wider. Between 1914 and 1953 the river continued its westward migration while widening significantly. By 1973, the average width of the rapid westward migration had continued. Between 1973 and 1992 the rate of increase of the average width accelerated to a very high level although the rate of westward migration slowed right down. The average westward migration rate of the centerline of the Brahmaputra-Jamuna River between 1830 and 1992 was 28 m y^{-1} , while the rate of migration of the west bank was about 50 m y^{-1} (Sarker et al. 2003). The river also shows significant morphological changes in the decadal-scale. As mentioned before, the total width of the river has been changing over time which has been hoped to be continued in recent time as well.

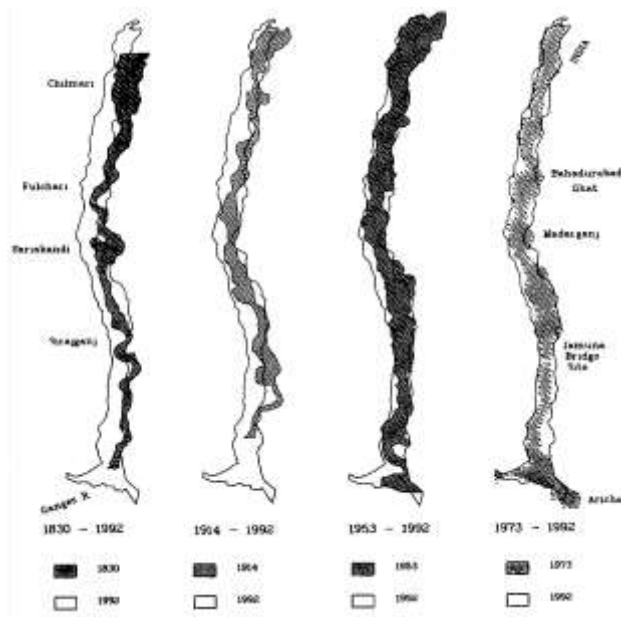


Fig.1.14 Westward migration of Brahmaputra-Jamuna-Jamuna [reproduced from Sarker et al. (2014)]

But Sarker et al. (2014) indicated that since the 1990s the rate of widening has been reduced substantially. During the process of widening, both banks have been migrating outwards (Fig.1.15). Migration of the left bank ceased from the early 1990s while the westward migration of the right bank has continued. Due to the construction of several bank protection works in the recent past, the rate of westward migration and widening has seemed to be retarded (Sarker et al. 2014).

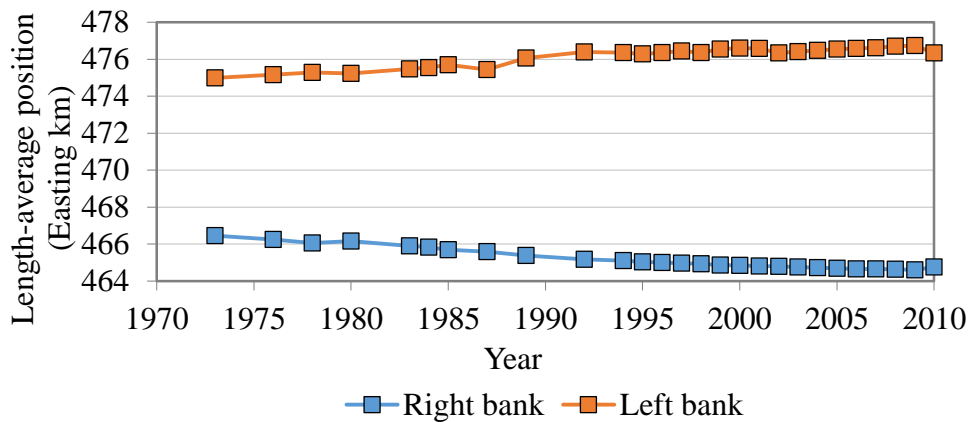


Fig.1.15 Length-averaged bankline migration of the Brahmaputra-Jamuna River [reproduced from Sarker et al. (2014)]

Even the yearly change of river planform due to flood is also significant (Shampa and Ali 2018). Fig.1.16 shows the change three year change of river planform from 2010-2013 near the Bahadurabad station. New bifurcation, decaying of channels, merging of bars, avulsion of major channels were the major planform changes during that time in this location.

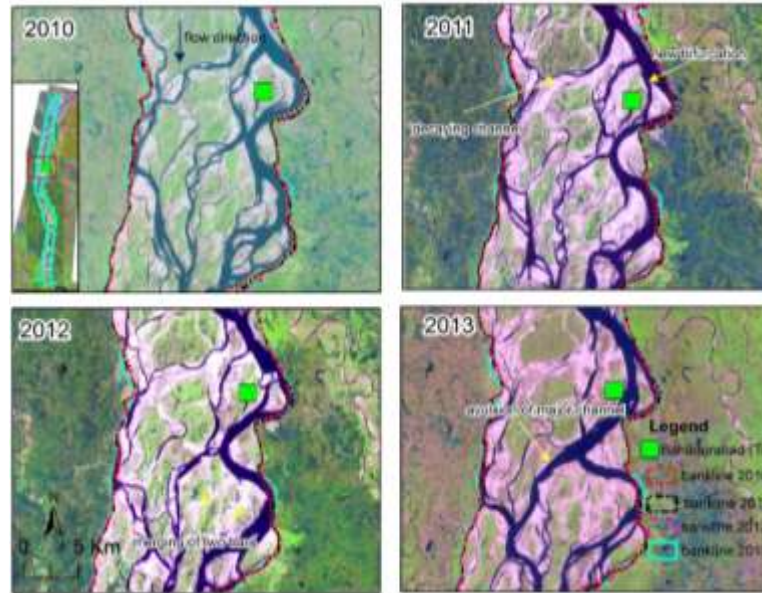


Fig.1.16 Yearly change of braided planform near the Bahadurabad station. The satellite images represents the month of February of the respected year

1.6 Outline of the Dissertation

This thesis contains five chapters. The contents of these chapters are discussed as follows:

Chapter 1 presents the background of the work, the research questions as well as objectives and a brief description of the study area.

Chapter 2 discusses the literature review and research gap about the present the numerical bed evolution calculation techniques of the braided river and followed by the detailed description of the two-dimensional numerical model used in this study.

Chapter 3 talks about the countermeasures of river bank protection used in the braided river. The experimental study done during this research has also discussed in this

chapter followed by the three-dimensional numerical model developed during this research. Lastly, it shows the application of the two-dimensional numerical model discussed in chapter 2 for of river bifurcation to manage the bank attached channel.

Chapter 4 presents the applicability of three-dimensional numerical model developed in chapter 3 at a small reach of Brahmaputra-Jamuna with the selected hydraulic structure.

Chapter 5 summarizes the conclusions based on the present study as well as limitations. And finally, it shows the dictions for future studies.

Chapter 2

Bed evolution process of the braided river network

2.1 Numerical modeling of braided rivers

The formative process of braided river bars and channels attracts the scientists and engineers for several decades. Since sixties extensive theoretical analysis were done to clarify the formative mechanism of bars and channels regarding the braided river (Anderson 1967; Colombini et al. 1987; Einstein and Shen 1964; Englund and Skovgaard 1973; Fredsøe 1978; Hansen 1967; Parker 1976; Reynolds 1965; Shen and Komura 1968; Watanabe et al. 2001; Werner 1951). Field surveys and flume experiments were also done to clarify the initiation and development process of bars and several braiding mechanisms i.e. bifurcation reproduction (Ashida and Shiomi 1966; Ashworth 1996; Bertoldi et al. 2009; Bertoldi and Tubino 2007; Best et al. 2006; Thorne et al. 1993). A broad scale summary of these attempts considering different scale and perspective is shown in Fig.2.1.

To reproduce the self-formed braided river to the natural one numerically, the researchers use synthesis approach (simplified rules of the system dynamics) to reductionist modelling approaches (classical continuum mechanics)(Williams et al. 2013). The reduced complexity-models or the cellular automata (Howard et al. 1970; Murray and Paola 1994; Thomas and Nicholas 2002) can reproduce the non-linear relationship of flow and sediment transport necessary to form the basic braided river despite the lack to physics. In one-dimensional modeling flow and sediment transport are simplified by assuming width-averaged variations. In case of braided network each channel can be assumed by one single channel by neglecting their transverse gradient of bed and 1D model can be applied to each channel. However, using 1D models with appropriate parametrization, the

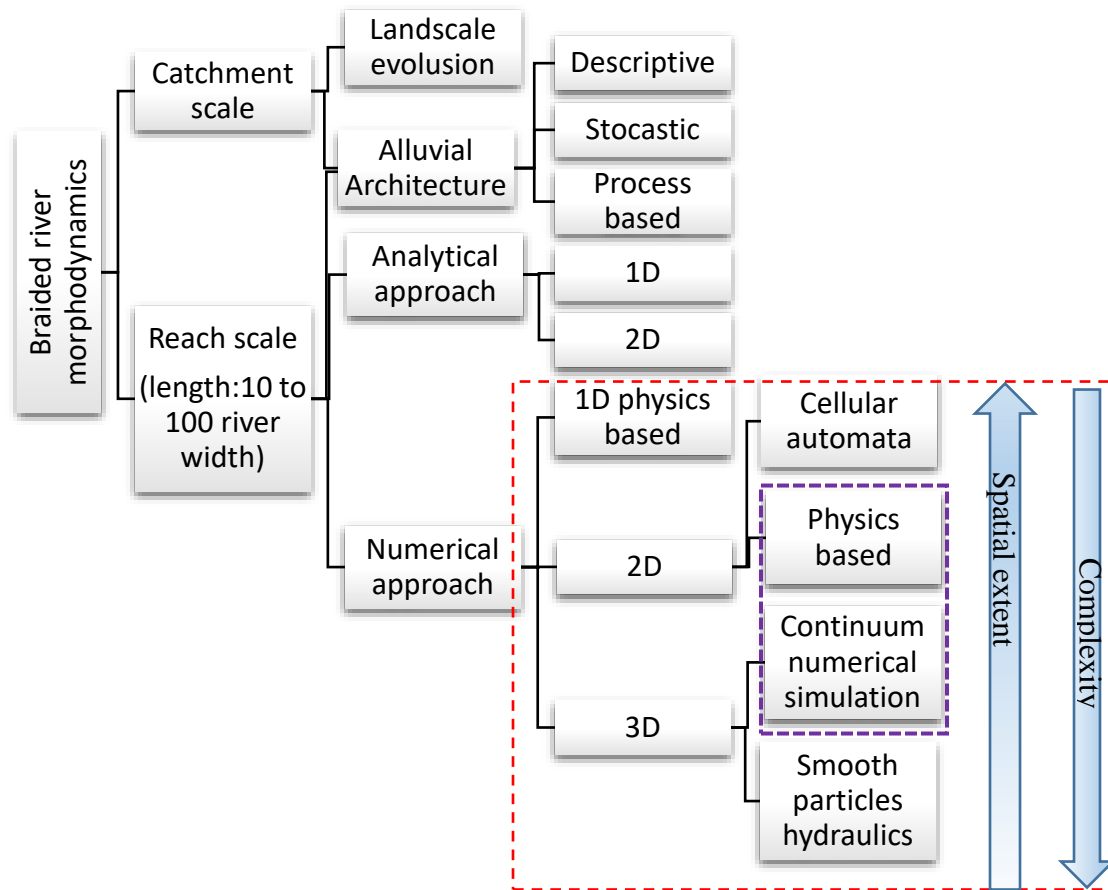


Fig.2.1 The types of model used to understand the braided river morphodynamics (Williams et al. 2016). The dashed purple-line indicate the numerical approaches which have conducted during this study

longitudinal morphological properties, and transport rate can be predicted but this type of model cannot be applied to predict bar-scale dynamics (Williams et al. 2016).

The limitations of 1D model in braided river can be overcome by using two-dimensional modeling approach which allow the lateral variation during bed evolution. “Shallow water equations models (SWE)” are widely used to model the 2D morphodynamics of braided river for both gravel bed (Jowett and Duncan 2012; Sambrook et al. 2009) and sand bed (Nicholas et al. 2013; Schuurman et al. 2018). The potentiality of SWE in reproduction of braided river dynamics have been discussed in Jang and Shimizu (2005) where they reproduce the laboratory braided model numerically considering erodible banks. However, in case of sandy braided river, sediment sorting is

quite common which has not been investigated so far extensively. Takebayashi et al. (2003) showed the effect of non-uniform sediment in braided stream and concluded that under unsteady flow conditions, mean diameter of sediment in trough of bar increases in the rising stage of flow while decreases in the falling stage. This process should process a great impact in the development process of bar in real river.

In general the three-dimensional flow models are used to predict heterogeneous flow fields especially near the hydraulic structure, including turbulence phenomenon to estimate the forces that influence the entrainment and deposition of individual sediment particles (Papanicolaou et al. 2008). Most 3D models solve the continuity and momentum equations of the Navier-Stokes, along with the sediment mass balance equation. The Reynolds average Navier-Stokes (RANS), Large Eddy Simulation (LES) and Direct Numerical Simulation (DNS) usually used to solve the turbulence and mean flow properties. Though DNS approach is produce very accurate results but it is considered computationally very expensive; not useable for everyday engineering problem (Rodi 2006). In case of LES, the computation domain or grid size play a significant role in model stability and the smaller-scale turbulent structures that are controlled by the momentum and mass exchange directed from and to the riverbed cannot be resolved directly with LES. Although the RANS models are criticized for averaging the equations while computing the turbulent properties, still this approach is computationally effective and widely used for everyday engineering problem (Papanicolaou et al. 2008). Nevertheless, for large scale modeling 3D modelling is not feasible computationally (van Rijn 1993).

Another approach used to analyze the braided river is the analysis of satellite images i.e. Baki and Gan 2012; Best et al. 2003b; Sarker et al. 2014). Though the analysis of satellite image produce quite good results especially in case of planform but still now these analysis has lacking of the proper relationship to the channel hydraulic property and planform changes.

From the above discussion it can be summarized that still now there exists the research gap to analysis the braided river focusing the compound bar. Nevertheless, the bed sorting method can be added to precise prediction of the vertical growth of the bar specially when the relatively bigger (>3 km) bar are formed. In the next sections of this

thesis is focused on overcoming such gaps by the numerical analysis of bed evolution during flood of sand-bed braided river, Brahmaputra-Jamuna.

2.2 Two dimensional morphodynamic model of bed evolution

2.2.1 Governing Equations

a) Hydrodynamic Equations

A two-dimensional depth averaged non-linear shallow water equations derived from of Navier-Stokes equations for incompressible free surface flow (shallow water equations) were solved with the consideration of Boussinesq approximations. The morphodynamic model was developed using open source Delft3D software (flow version 4.00.01.000000) by applying the following hydrodynamic equations.

Conservation of mass was calculated by using the continuity equation (2.1)

$$\frac{\partial h}{\partial t} + \frac{\partial(hu)}{\partial x} + \frac{\partial(hv)}{\partial y} = 0 \quad (2.1)$$

In the x-direction, conservation of momentum equation (2.2)

$$\frac{\partial u}{\partial t} + u \frac{\partial u}{\partial x} + v \frac{\partial u}{\partial y} + g \frac{\partial \zeta}{\partial x} + \frac{gn^2}{\sqrt[3]{h}} \left(\frac{u(u^2+v^2)}{h} \right) - v_h \left(\frac{\partial^2 u}{\partial x^2} + \frac{\partial^2 u}{\partial y^2} \right) = 0 \quad (2.2)$$

In the y-direction, conservation of momentum equation (2.3)

$$\frac{\partial v}{\partial t} + u \frac{\partial v}{\partial x} + v \frac{\partial v}{\partial y} + g \frac{\partial \zeta}{\partial x} + \frac{gn^2}{\sqrt[3]{h}} \left(\frac{v(u^2+v^2)}{h} \right) - v_h \left(\frac{\partial^2 v}{\partial x^2} + \frac{\partial^2 v}{\partial y^2} \right) = 0 \quad (2.3)$$

Where, ζ is water level elevation with respect to datum (here in m); h represents water depth (m) u, v is depth average velocity in the x and y directions, respectively (m/s); g is acceleration due to gravity (m/s²); v_h denotes kinetic eddy viscosity (m²/s); n represents the Manning's coefficient (sm^{-1/3}).

The term $v_h \left(\frac{\partial^2 u}{\partial x^2} + \frac{\partial^2 u}{\partial y^2} \right)$ and $v_h \left(\frac{\partial^2 v}{\partial x^2} + \frac{\partial^2 v}{\partial y^2} \right)$ in equation 2.2 and 2.3 basically represents horizontal Reynold's stress under eddy viscosity concept and neglecting the shear stress along the closed boundaries.

The transport equation (advection–diffusion equation) is given by equation (2.4)

$$\frac{\partial(hc)}{\partial t} + \frac{\partial(huc)}{\partial x} + \frac{\partial(hvc)}{\partial y} = h \left[\frac{\partial}{\partial x} \left(D_H \frac{\partial c}{\partial x} \right) + \frac{\partial}{\partial y} \left(D_H \frac{\partial c}{\partial y} \right) \right] + hS \quad (2.4)$$

Here, c is mass sediment concentration (kg/m^3) and the horizontal diffusivity is represented by D_H . S represents sediment source terms per unit area and calculated as follows

$$S = \frac{c_{eq} - c}{t_s} \quad (2.5)$$

Here c_{eq} and t_s denotes the depth-averaged equilibrium sediment concentration and an adaptation time-scale respectively. c_{eq} is calculated using the following formula

$$c_{eq} = \frac{\bar{S}_{sus}}{|u|h} \quad (2.6)$$

\bar{S}_{sus} is depth average suspended sediment transport vector and its calculation procedure is described on section 2.2.1 b. 2D turbulence quantities is not resolved by advection on the horizontal computational grid rather incorporated by user defined constant values.

In order to solve the equations 2.1 to 2.4, the horizontal viscosity and diffusivity are needed to be resolved. It is that assumed that the horizontal viscosity and diffusivity is the superposition of molecular viscosity and 2D turbulence. The molecular viscosity of the water at 20^0 C are considered and kept constant throughout the simulation. $k - \varepsilon$ turbulence model was used for turbulence closure in which both the turbulent kinetic energy k and the dissipation ε are produced by production terms representing shear stresses at the bed, surface, and in the flow. The mixing length l is determined by using the equation 2.7

$$l = c_d \frac{k\sqrt{k}}{\varepsilon} \quad (2.7)$$

Here, c_d denotes calibration constant.

b) Sediment Transport Equations

As described in the earlier chapter the braided rivers are basically remain bed-load dominated zones. Hence the calculations of bed load transport plays a significant role in the estimation of the bed evolution. Previous researchers used several formula to estimate the bed load (Ackers and White 1973; Ashida and Michiue 1972; Bagnold 1956; Engelund and Hansen 1967; Meyer-Peter and Müller 1948; Van Rijn 1993). However, the existing

sediment transport formulas has some limitations, almost all of the above mentioned formulas were established by using limited flume and field data. As an example, the Meyer-Peter and Müller (1948) formula was developed based on laboratory flumes with widths ranging between 15cm and 2m, having flow depth of 1 to 120cm, sediment ranges from 6.4 and 30 mm and specific weight of sediment particles varies from 1.25 to over 4. It is apparent that this formula is more applicable for coarse sediment. The suspended load transport should be calculated considering the convective and diffusive processes (Zang 2005). Furthermore, the braided river are characterize to transport a wide spectrum of sediment sizes. The behavior of braided bar with mixed sediment and uniform sediment is quite different. For instance, the erosion of particles with a certain size from the channel-bed and over the bar will depend on not only the flow conditions but also the amount of that size available in the bed surface. This process can be simplified in numerical simulation by using sediment size fractions. In this study such process has also investigated using series of size fractions.

Kabir and Ahmed (1996) showed a relative comparison of bed load computed using different formulas for Brahmaputra-Jamuna river and concluded that Van Rijn (1993) predicts well as compared with the observed data during the wet season. Hence for the numerical model Van Rijn (1993) was used to calculate the sediment transport.

Firstly, the settling velocity of sand sediment, ω_s is calculated by using the method of Van Rijn (1993) based on the nominal sediment diameter and the relative density of the sediment particles.

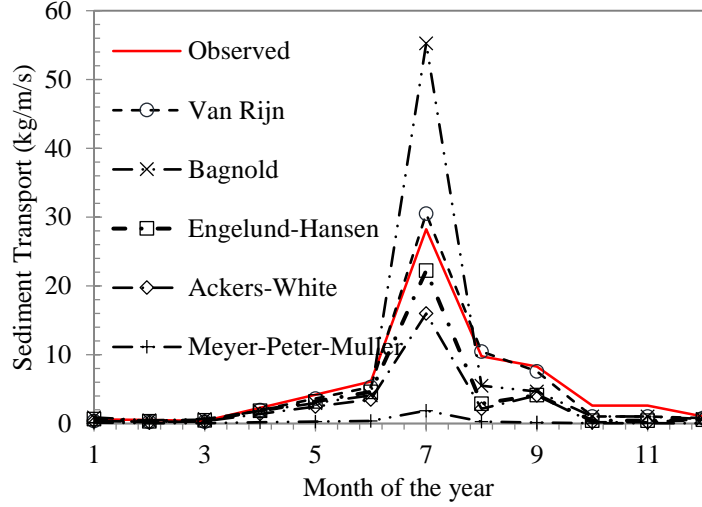


Fig.2.2 The comparison of bed-load computed using several formulas (Kabir and Ahmed 1996)

Bed-load sediment transport

The bed load transport rate $|\bar{S}_{bed}|$ is computed by equation 2.8

$$|\bar{S}_{bed}| = \begin{cases} 0.053\sqrt{(s-1)gd_{50}^3}D_*^{-0.3}\left(\frac{\mu_c\tau-\tau_c}{\tau_c}\right)^{2.1} & \text{if } \left(\frac{\mu_c\tau-\tau_c}{\tau_c}\right) < 3.0 \\ 0.1\sqrt{(s-1)gd_{50}^3}D_*^{-0.3}\left(\frac{\mu_c\tau-\tau_c}{\tau_c}\right)^{1.5} & \text{if } \left(\frac{\mu_c\tau-\tau_c}{\tau_c}\right) \geq 3.0 \end{cases} \quad (2.8)$$

Where, s is the specific density of sediment particle $\left(\frac{\rho_s}{\rho_f}\right)$, d_{50} denotes particle size τ and τ_c bed shear stress and critical bed shear stress respectively. μ_c is the ratio between the total bed roughness and the grain related bed roughness The dimensionless particle parameter D_* is defined by equation 2.9

$$D_* = d_{50} \left\{ \frac{(s-1)g}{\nu^2} \right\}^{1/3} \quad (2.9)$$

Here, ν is the kinematic viscosity coefficient $\left(\frac{\mu_m}{\rho}\right)$. Then the bed load vector components become

$$\bar{S}_{bed,u} = \frac{u_{b,u}}{|u_b|} |\bar{S}_{bed}| \quad (2.10)$$

$$\bar{S}_{bed,v} = \frac{u_{b,v}}{|u_b|} |\bar{S}_{bed}| \quad (2.11)$$

Here, $u_{b,u}, u_{b,v}$ and $|u_b|$ are local bottom-layer flow velocity components and magnitude. Then the bed load vector is modified to incorporate the slope of the river bed by using the method of Bagnold (1966).

$$\bar{S}_{bed,us} = \alpha_{bs} \frac{u_{b,u}}{|u_b|} |\bar{S}_{bed}| \quad (2.12)$$

$$\bar{S}_{bed,vs} = \alpha_{bs} \frac{u_{b,v}}{|u_b|} |\bar{S}_{bed}| \quad (2.13)$$

$$\alpha_{bs} = 1 + c_{d,bs} \left[\frac{\tan \theta}{\cos(\tan^{-1}(\frac{\partial z}{\partial s}))(\tan \theta - \frac{\partial z}{\partial s})} - 1 \right] \quad (2.14)$$

Here $c_{d,bs}$ is the tuning factor for bed slope effect, θ denotes the internal angle of friction of bed material (assumed 30° in this study), $\frac{\partial z}{\partial s}$ is the bed slope in the direction of the bed-load transport (downward positive). On the other hand, as the transverse bed slope is another characteristics of braided river, the effect of transverse bed slope is also added by using Ikeda (1982). Finally the modified bed load transport q_u and q_v vectors are calculated by using the following equations.

$$q_u = \bar{S}_{bed,us} - \alpha_{tr} \bar{S}_{bed,vs} \quad (2.15)$$

$$q_v = \bar{S}_{bed,vs} + \alpha_{tr} \bar{S}_{bed,us} \quad (2.16)$$

Where,
$$\alpha_{tr} = 1.5 \sqrt{\tau_{b,c}} \left(\frac{\partial z}{\partial s} \right) \quad (2.17)$$

α_{tr} defines transverse bed slope correction factor

Suspended-load sediment transport

The suspended load transport rate $|\bar{S}_{sus}|$ is computed by equation 2.18

$$|\bar{S}_{sus}| = |f_s C_a u h| \quad (2.18)$$

To calculate the distribution of u the depth averaged distribution is assumed which can be expressed as

$$u = \left[\frac{\bar{u}}{\frac{z_0}{h} - 1 + \ln \frac{h}{z_0}} \right] \ln \left(\frac{z}{z_0} \right) \quad (2.19)$$

\bar{u} is mean three dimensional velocity; z expressed vertical cartesian coordinate (m); z_0 expressed bottom cartesian coordinate, C_a is the sediment concentration at reference height a can is calculated by using equation

$$C_a = 0.015k_r\rho_s \frac{d_{50}}{a} \frac{T^{1.5}}{D_*^{0.3}} \quad (2.20)$$

In equation 2.20 k_r is a denotes the relative availability of the sediment fraction at the bed; T is nondimensional bed share stress determined by Van Rijn (1993) method; a is Van Rijn's reference height and is determined by equation 2.21

$$a = \min[\max\{f_a, k_e, \frac{\Delta_r}{2}, 0.01h\}, 0.20h] \quad (2.21)$$

In equation 2.21 f_a is Van Rijn's reference height proportionality factor, k_e is Current related effective roughness height and Δ_r is ripple height.

In equation 2.18 f_s is the shape factor for the vertical distribution of suspended sediment and is determined by equation 2.22

$$f_s = \frac{\left(\frac{a}{h}\right)^{s'} - \left(\frac{a}{h}\right)^{1.2}}{\left(1 - \frac{a}{h}\right)^{s'} (1.2 - s')} \quad (2.22)$$

$$s'_s = s_s + s_{s,r} \quad (2.23)$$

s_s is the suspension parameter and is determined by equation 2.24 and $s_{s,r}$ is the overall correction factor.

$$s_s = \frac{\omega_s}{\psi\kappa u_*} \quad (2.24)$$

Here ω_s is the particle fall velocity of suspended sediment, ψ is the coefficient related to the diffusion of sediment particles, κ is the constant of Von-Karman and u_* is the overall bed share velocity. The sediment source term, E_k and sink term, D_k are then calculated assuming a linear concentration gradient between the calculated reference concentrations at height a and the computed concentration in the reference cell expressed as follows

$$E_k = C_a \left(\frac{D_v}{\Delta z}\right) \quad (2.25)$$

$$D_k = C_{kmx} \left(\frac{D_v}{\Delta z} + \omega_s\right) \quad (2.26)$$

In which D_v is the vertical diffusion coefficient at the bottom of the reference cell, Δz is the vertical distance from the reference level a to the center of reference cell, and C_{kmx} is the concentration of the sediment fraction in the reference cell. Considering only sand transport D_v is expressed by

$$D_v = \beta_v \vartheta_v \quad (2. 27)$$

β_v is the van Rijn's β factor and can be expressed by

$$\beta_v = 1 + 2 \left(\frac{\omega_s}{u_*} \right) \text{ (Limited to the range } 1.0 \leq \beta_v \leq 1.5) \quad (2. 28)$$

c) Bed change

If the transport rate of bed load and suspended load is known, the bed elevation can be calculated by applying the mass-balance equation (Exner 1925) using equation (2.29). For a size fraction k during a mixed sediment transport

$$(1 - \lambda) \frac{\partial \eta_{bk}}{\partial t} + m_f \left(\frac{\partial q_{uk}}{\partial x} + \frac{\partial q_{vk}}{\partial y} \right) + m_f (E_k - D_k) = 0 \quad (2. 29)$$

Here, λ is porosity, q_{uk}, q_{vk} is bed load transport vector for the size fraction k , η_{bk} is the bed change due to size fraction k ; E_k, D_k are upward and downward suspended sediment transport flux near the bed for the size fraction k ; m_f is the morphological acceleration factor to reduce the computational time step to adapt the morphology. The summation of the bed changes, $\delta \eta_b$ due to all the size fractions is the resulted the total bed variation in one time step,

$$\delta \eta_b = \sum_{k=1}^M \delta \eta_{bk} \quad (2. 30)$$

Here M is the total size fractions.

Erosion of dry cell

In case of erosion of adjacent dry cell near the bank or bar a scheme used by Roelvink et al. (2006) has been implemented that allows the (partial) redistribution of an erosion flux from a wet cell to the adjacent dry cells. If the maximum fraction of erosion to reallocate from edge wet cells to surrounding dry cell(s) is $\theta_{dc,thr}$ and h_{dcmax} is the used defined water depth in the wet cell at which the full $\theta_{dc,thr}$ will be reallocated, the actual fraction of erosion in an edge, θ_{dc} can be expressed as

$$\theta_{dc} = \min\left(\frac{h-h_{dc,thr}}{h_{dcmax}-h_{dc,thr}}, 1\right) \theta_{dc,thr} \quad (2.31)$$

Where, $h_{dc,thr}$ is the minimum threshold flow depth for reallocating the erosion in dry cell.

Bed sorting

The methods used to track the of bed-sediment composition with bed-profile changes have been attempted by a number of researchers (Chang, 1988). Theses researches may be categorized into three kinds-mixed layer based approach (Hirano 1971), multi-layer approach (Ribberink 1987), sorting evolution approach (Blom 2008). However, no comparative study has been found which summarize the suitable possible bed sorting model. Here, modified multi-layer approach (Ribberink 1987) has been used. The natural river bed is discretized vertically into a series of layers including active, transition, under and base layer above a datum level z_0 as shown in Fig.2.3.

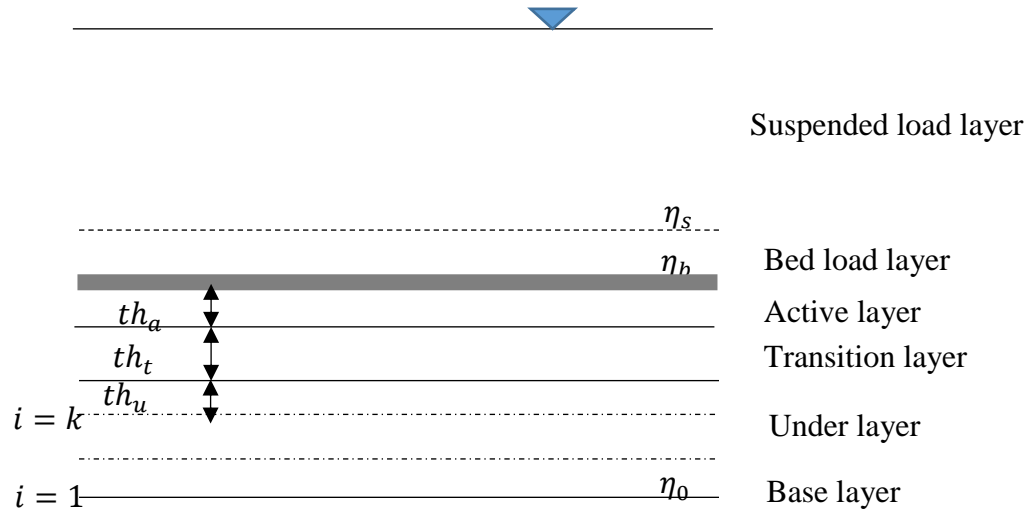


Fig.2.3 Definition Sketch of a Vertical bed Profile

Only the sediment contained in the active layer is available for erosion or deposition during a calculation time step. A transition layer is situated below the active layer, can exchange particles to the active layers. The under layers act as a reserve for the sediment. According to Fig.2.3 the bed level, η_b can be expressed as

$$\eta_b = \eta_0 + th_a + th_t + \sum_{i=1}^{i=k} th_u \quad (2.32)$$

Here, th_a, th_b, th_u represents the thickness of active, transition and under layers. During the sediment transport, the thickness of the transition layer should not be larger than that of the under layer $th_t \leq th_u$. The thickness of the active layer is controlled with a function of flow depth by ensuring relatively small $\delta\eta_b/th_a$. From a time step t to a new time step $t+1$, the ratio of each size fraction in different layers, f_{bk} , the thickness of the transition layer, th_t , and the total number of the under layers, n_u were updated using the equations 2.33 - 2.37 in case of deposition and equations 2.38 - 2.42 in case of erosion.

When $\delta\eta_b \geq 0$

$$f_{bk}^{t+1} = \left(1 - \frac{\delta\eta_b}{th_a}\right) f_{bk}^t + \frac{\delta\eta_{bk}}{th_a} \quad (2.33)$$

$$th_t^{t+1} = \begin{cases} th_t^t + \delta\eta_b & \text{if } th_t^t + \delta\eta_b \leq th_u \\ th_t^t + \delta\eta_b - th_u & \text{if } th_t^t + \delta\eta_b > th_u \end{cases} \quad (2.34)$$

$$f_{tk}^{t+1} = \begin{cases} \frac{th_t^t}{th_t^{t+1}} f_{tk}^t + \frac{\delta\eta_b}{th_t^{t+1}} f_{bk}^t & \text{if } th_t^t + \delta\eta_b \leq th_u \\ f_{bk}^t & \text{if } th_t^t + \delta\eta_b > th_u \end{cases} \quad (2.35)$$

$$n_u^{t+1} = \begin{cases} n_u^m & \text{if } th_t^t + \delta\eta_b \leq th_u \\ n_u^m + 1 & \text{if } th_t^t + \delta\eta_b > th_u \end{cases} \quad (2.36)$$

$$f_{n_u k}^{t+1} = \begin{cases} f_{n_u k}^t & \text{if } th_t^t + \delta\eta_b \leq th_u \\ \frac{th_t^t}{th_u} f_{tk}^t + \left(1 - \frac{th_t^t}{th_u}\right) f_{bk}^t & \text{if } th_t^t + \delta\eta_b > th_u \end{cases} \quad (2.37)$$

When $\delta\eta_b < 0$

$$f_{bk}^{t+1} = \begin{cases} f_{bk}^t + \frac{th_t^t}{th_a} f_{bk}^t - \frac{th_t^t + \delta\eta_b}{th_a} f_{n_u k}^t + \frac{\delta\eta_{bk}}{th_a} & \text{if } th_t^t + \delta\eta_b \leq 0 \\ f_{bk}^t - \frac{\delta\eta_b}{th_a} f_{th_t k}^t + \frac{\delta\eta_{bk}}{th_a} & \text{if } th_t^t + \delta\eta_b > 0 \end{cases} \quad (2.38)$$

$$th_t^{t+1} = \begin{cases} th_t^t + th_u + \delta\eta_b & \text{if } th_t^t + \delta\eta_b \leq 0 \\ th_t^t + \delta\eta_b & \text{if } th_t^t + \delta\eta_b > 0 \end{cases} \quad (2.39)$$

$$f_{tk}^{t+1} = \begin{cases} f_{n_u k}^t & \text{if } th_t^t + \delta\eta_b \leq 0 \\ f_{tk}^t & \text{if } th_t^t + \delta\eta_b > 0 \end{cases} \quad (2.40)$$

$$n_u^{t+1} = \begin{cases} n_u^m - 1 & \text{if } th_t^t + \delta\eta_b \leq 0 \\ n_u^m & \text{if } th_t^t + \delta\eta_b > 0 \end{cases} \quad (2.41)$$

$$f_{n_u^k}^{t+1} = \begin{cases} f_{(n_u-1)k}^t & \text{if } th_t^t + \delta\eta_b \leq 0 \\ f_{n_u^k}^t & \text{if } th_t^t + \delta\eta_b > 0 \end{cases} \quad (2.42)$$

Where subscript a denotes the active layer; subscript t is for the transition layer; subscript u expresses the deposited layer; subscript k defines the k th size fraction; subscript b is for riverbed; f is for the percentage of one size fraction; th is for the thickness of one layer.

d) Discretization methods

The gridding system used for simulation is curvilinear. Hence, prior to discretize the 2D shallow water equations the model domain is divided into curvilinear gridding system. The governing equations 2.1 to 2.3 were modified to fit the curvilinear gridding system. The geometrical quantities J_ξ , J_η have been introduced to the governing equation described in 2.43, 2.44 and 2.45. The modified equations are following:

The depth-averaged continuity equation is given by:

$$\frac{\partial \zeta}{\partial t} + \frac{1}{J_\xi J_\eta} \frac{\partial [(d+\zeta)uJ_\eta]}{\partial \xi} + \frac{1}{J_\xi J_\eta} \frac{\partial [(d+\zeta)vJ_\xi]}{\partial \eta} = 0 \quad (2.43)$$

The momentum equations in ξ and η coordinate system are

$$\frac{\partial u}{\partial t} + \frac{u}{J_\xi} \frac{\partial u}{\partial \xi} + \frac{v}{J_\eta} \frac{\partial u}{\partial \eta} + \frac{g}{J_\xi} \frac{\partial \zeta}{\partial \xi} + \frac{gn^2}{\sqrt[3]{(d+\zeta)}} \left[\frac{u(u^2+v^2)}{(d+\zeta)} \right] - F_\xi = 0 \quad (2.44)$$

$$\frac{\partial v}{\partial t} + \frac{u}{J_\xi} \frac{\partial v}{\partial \xi} + \frac{v}{J_\eta} \frac{\partial v}{\partial \eta} + \frac{g}{J_\eta} \frac{\partial \zeta}{\partial \eta} + \frac{gn^2}{\sqrt[3]{(d+\zeta)}} \left[\frac{v(u^2+v^2)}{(d+\zeta)} \right] - F_\eta = 0 \quad (2.45)$$

Here, J_ξ , J_η is the coefficients used to transform curvilinear to rectangular coordinates (m); $F_\xi = v_h \left(\frac{1}{J_\xi J_\eta} \frac{\partial^2 u}{\partial \xi^2} + \frac{1}{J_\xi J_\eta} \frac{\partial^2 u}{\partial \eta^2} \right)$, $F_\eta = v_h \left(\frac{1}{J_\xi J_\eta} \frac{\partial^2 v}{\partial \xi^2} + \frac{1}{J_\xi J_\eta} \frac{\partial^2 v}{\partial \eta^2} \right)$ are turbulent momentum flux in ξ and η direction respectively d the depth below the reference plane ($h = d + \zeta$).

The discretization method for equation 2.43 to 2.45 can be done by explicitly or implicitly. However, the time integration of these shallow water equations for the explicit method are subjected to satisfy the Courant–Friedrichs–Lewy (CFL) condition as follows:

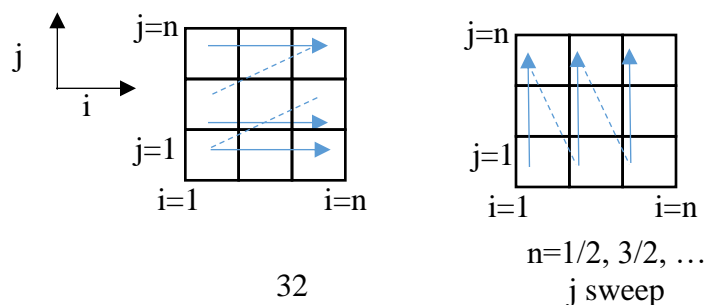
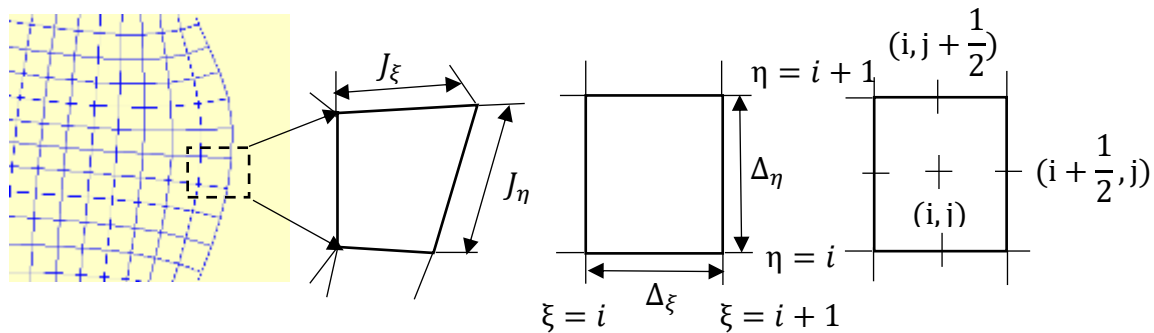
$$\text{CFL} = 2\Delta t \sqrt{gH \left(\frac{1}{\Delta x^2} + \frac{1}{\Delta y^2} \right)} < 1 \quad (2.46)$$

Where Δt is the time step and in curvilinear gridding system $\Delta x = J_\xi$ and $\Delta y = J_\eta$ are the smallest grid space in ξ and η coordinate system. Exceeding the time step Δt will introduce instability to the model when subjected to practical use. Therefore an implicit method is necessary. Crank-Nicholson method can be a solution in this regard but in Crank-Nicholson method a large system of matrix needed to be solved i.e. the linearized depth-averaged form of equations without advection and bottom friction in Crank-Nicholson method is shown in equation 2.47

$$\frac{U^{n+1} - U^n}{\Delta t} + \frac{1}{2}AU^n + \frac{1}{2}AU^{n+1} = \vec{0} \quad (2.47)$$

With

$$U = (u, v, h)^T \text{ And } A = \begin{pmatrix} 0 & 0 & g \frac{\partial}{\partial x} \\ 0 & 0 & g \frac{\partial}{\partial y} \\ h \frac{\partial}{\partial x} & h \frac{\partial}{\partial y} & 0 \end{pmatrix}$$



n=0, 1, 2, ...
i sweep

Fig.2.4 Mapping of physical space to computational space

The solution after one time step is given by

$$\mathbf{U}^{n+1} = \frac{(I - \frac{1}{2}\Delta t A)}{(I + \frac{1}{2}\Delta t A)} \mathbf{U}^n \quad (2.48)$$

After discretization in both grid directions generates a system of differential equations with a band matrix with at least five non-zero matrices with implicitly coupled grid points which require large computational efforts. To solve such problems Alternating Direction Implicit (ADI) method (Peaceman and H. H. Rachford 1955) was introduced for shallow water equations by Leendertse et al. (1977) and Leendertse and Gritton (1971). This method has been followed in this study. Using this method one time steps splits into two different stages. The equation 2.47 can be written in ADI form as equation 2.49 and 2.50. If in one stage the variable has taken in implicitly (i sweep in Fig. 2.4) then in the next stage that variables have considered explicitly (j sweep in Fig. 2.4).

Step 1:

$$\frac{\vec{U}^{n+\frac{1}{2}} - \vec{U}^n}{\frac{1}{2}\Delta t} + \frac{1}{2}A_x \vec{U}^{n+\frac{1}{2}} + \frac{1}{2}A_y \vec{U}^n = \vec{0} \quad (2.49)$$

Step 2:

$$\frac{\vec{U}^{n+1} - \vec{U}^{n+\frac{1}{2}}}{\frac{1}{2}\Delta t} + \frac{1}{2}A_x \vec{U}^{n+\frac{1}{2}} + \frac{1}{2}A_y \vec{U}^{n+1} = \vec{0} \quad (2.50)$$

With

$$A_x = \begin{pmatrix} 0 & 0 & g \frac{\partial}{\partial x} \\ 0 & u \frac{\partial}{\partial x} + v \frac{\partial}{\partial y} & 0 \\ h \frac{\partial}{\partial x} & 0 & u \frac{\partial}{\partial x} \end{pmatrix} \quad \text{and}$$

$$A_y = \begin{pmatrix} u \frac{\partial}{\partial x} + v \frac{\partial}{\partial y} & 0 & 0 \\ 0 & 0 & g \frac{\partial}{\partial y} \\ 0 & h \frac{\partial}{\partial y} & v \frac{\partial}{\partial y} \end{pmatrix}$$

In the first stage $t = n$ to $t = n + \frac{1}{2}$, v -momentum equation is solved followed by u - momentum equation which is implicitly coupled with continuity equation. In the next step, $t = n + \frac{1}{2}$ to $t = n + 1$ u -momentum equation is solved followed by v -momentum equation (equation 2.24) which is implicitly coupled with continuity equation. The pressure term and advection and viscosity terms are coupled explicit and implicit alternately. The non-linear in the coupled continuity equation, and momentum equation, i.e. $\frac{\partial[(d+\zeta)uJ_\eta]}{\partial \xi}$ requires an iterative procedure to solve but here the iteration is removed by multiplying the free surface gradient in the discretized momentum equation by a factor which converge to 1. The Reynolds' stress term i.e. $v_h \left(\frac{1}{J_\xi J_\eta} \frac{\partial^2 u}{\partial \xi^2} + \frac{1}{J_\xi J_\eta} \frac{\partial^2 u}{\partial \eta^2} \right)$ results a Laplace operator along grid lines which is integrated fully implicitly by using operator splitting.

For spatial discretization of normal advection term, $u \frac{\partial u}{\partial \xi}$ and cross advection term, $v \frac{\partial u}{\partial \eta}$ dissipative reduced phase error scheme (Stelling and Leendertse 1992) was used. The advection terms are integrated implicitly in the stage of the ADI-method. The upwind discretization is used. The resulting linear system of equations has eleven diagonals which is solved efficiently by a Red Black Jacobi iterative scheme. The approximation of vertical viscosity, $v_h \left(\frac{\partial^2 u}{\partial x^2} + \frac{\partial^2 u}{\partial y^2} \right)$ was discretize using central difference method.

2.2.2 Model Schematization

a) Bathymetry and Mesh generation

For the numerical model, a 225-km long curvilinear grid was constructed with an average width of 13 km; starting from almost 10 km downstream of the Noonkhawa water level measuring station and ending near Aricha (Fig 2.5). The reach was discretized by 1117x73 grid cells. This grid resolution was chosen to cover every bar by at least two grid cells (grid cell size 201x178 m²) because the bar size ranges from 549.83x205 m² to 28635x10475 m² within study reach of Brahmaputra-Jamuna. The measured river cross-section by the Bangladesh Water Development Board (BWDB) in 2011 was used as the bathymetry data

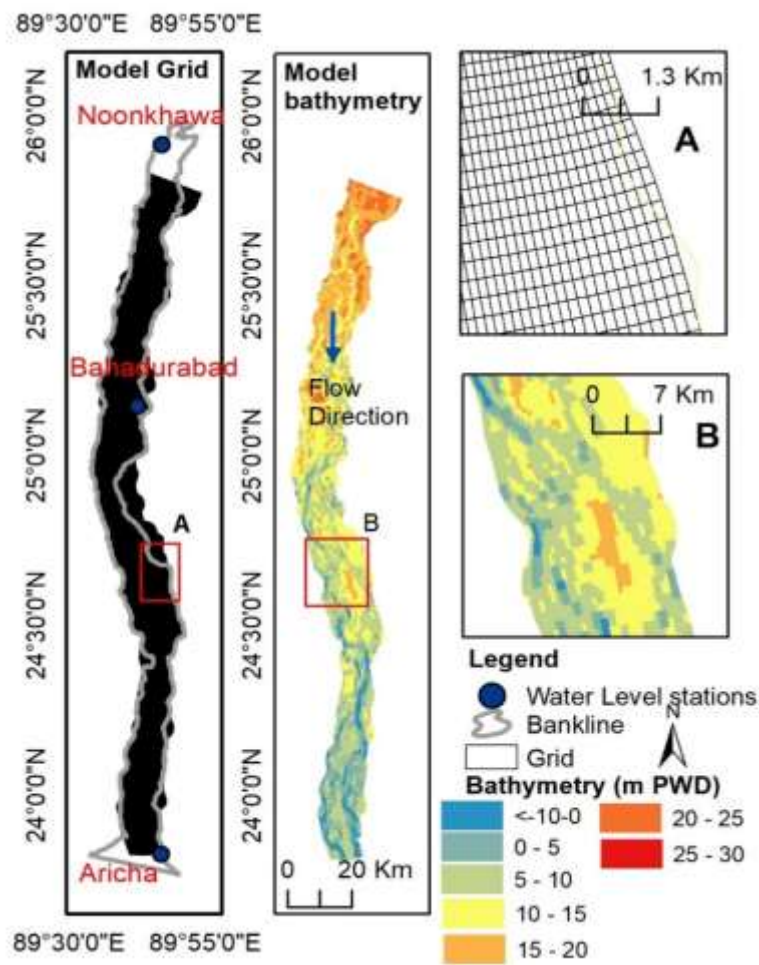


Fig.2.5 The model domain and bathymetry

Along with this, for bar-top topography, Shuttle Radar Topography Mission (SRTM) data was used in some places.

b) Boundary conditions

The simulation period of our model was the 1st of June, 2011 to the 15th of October, 2011 and the boundary conditions are shown in Fig.2.6. As the upstream boundary condition discharge data was used. The river Brahmaputra-Jamuna has only one discharge measuring station at Bahadurabad Fig.1.8 which is situated almost at the middle part of the study reach, and one major contributing tributary, Teesta, also lies within the upper part of the study reach.

Hence, for estimating the discharge at the upstream boundary, a 1D model was used and the model was calibrated to the flow data at Bahadurabad. As the discharge data for Teesta, daily average time series data was used. As the downstream boundary, the water level data of Aricha of the year 2011 was used. The water level was measured with respect to Public Works Datum (PWD), which is widely used datum in Bangladesh. It represents 0.46 m below the Mean Sea Level (MSL) datum. For bed sorting, in case of uniform bed, the diameter of sediment was assumed $277 \mu\text{m}$. For mixed bed case initially; for upper layer 70% of $150 \mu\text{m}$ and 30% of $277 \mu\text{m}$ and underlayer 70% of $277 \mu\text{m}$ and 30% of $150 \mu\text{m}$ with an substrate of $277 \mu\text{m}$ diameter of sediment was assumed. The other parameters used in the model are described in Table 1.

As the initial condition, the space varying water level, which confirms the minimum water depth of 1m in all channels, was given. The equilibrium sand concentration (VanRijn, 1984) was considered at the inflow boundary for sediment calculation. The initial sediment layer thickness was assumed to be 5 m at the bed. The minimum depth for sediment calculation was considered to be 0.1 m.

The morphological acceleration factor (m_f) ranges from 1 to 500 (Jang and Shimizu, 2005; Crosato et al., 2011, 2012; Roelvink, 2006; Van der Wegen and Roelvink, 2008 and Lesser et al., 2004). However, the m_f value was chosen for a braided river and finalized it through trial and error to best match with the real river planform and bathymetry.

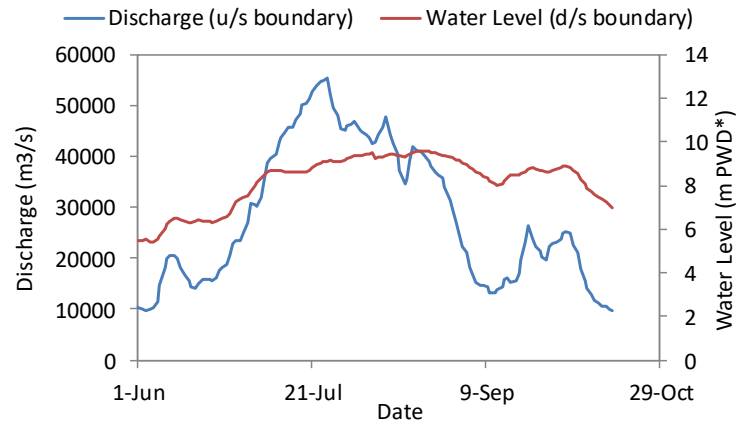


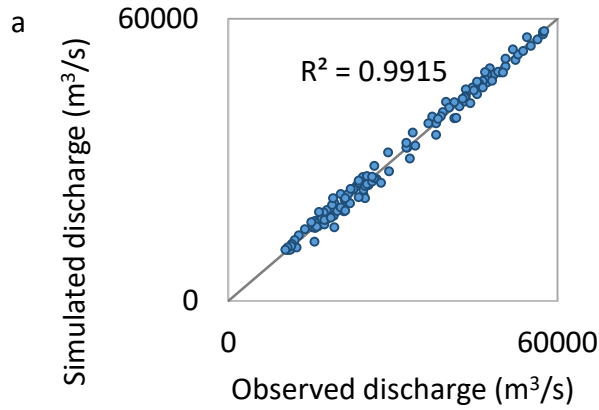
Fig.2.6 Boundary condition of the Model

Table 2.1 Model Parameters

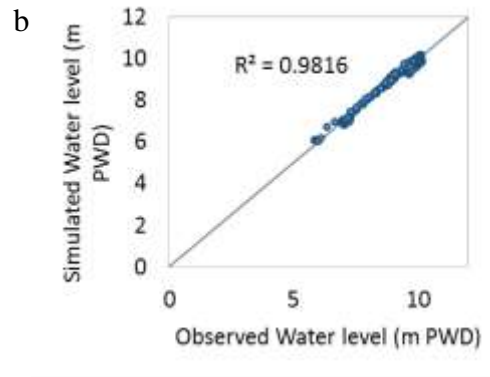
Parameter	Unit	Value
Mean grain size, d_{50}	μm	150-277
Density of sediment, ρ_s	kg/m^3	2650
Density of water ρ_f	kg/m^3	1000
Submerged specific density of sediment, s	-	1.65
Van Rijn's reference height factor, f_a	-	2
Horizontal eddy viscosity, ν_h	m^2s^{-1}	1
Hydrodynamic time step, t	s	48
Morpho-dynamic time step	s	144
Grid cell dimension	m^2	201*178
Roughness (manning's) n	$\text{s}/[\text{m}^{1/3}]$	0.027
Morphological acceleration factor, m_f	-	3
Calibration parameter, $c_{d,bs}$	-	0.70
Calibration parameter, α_{tr}	-	0.5
Threshold sediment thickness,	m	0.005
Thickness of the transport layer	m	0.2
Max Number of exchange layers		30
Horizontal eddy diffusivity, D_h	m^2s^{-1}	10

c) Model calibration and validation

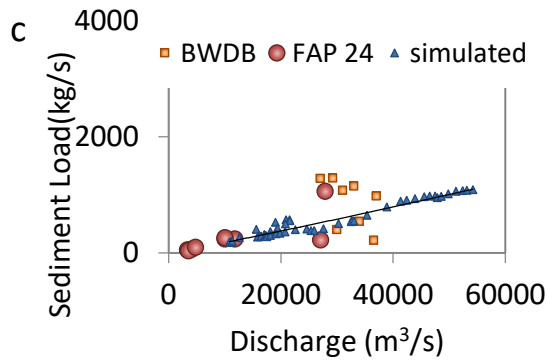
The water level calibration was performed along four points Chilmari, Kazipur, Sirajganj and Mathura respectively while the discharge and sediment calibration were performed only for Bahadurabad station (Locations are shown in Fig.1.8). Fig.2.7a and Fig.2.7b show the discharge, water level calibration results of the model at Bahadurabad and Mathura, respectively. The calibration of sediment was performed using the data set of sediment from 1968 to 2001 measured by BWDB and by the Flood Action Plan-24 (FAP-24) study due to the lack of recent data, which is shown in Fig.2.7c. In FAP-24 study, sediment data represents the river conditions for a particular period (mainly the year 1993). For this reason, some discrepancies are found in this dataset. As mentioned earlier, using the equilibrium sediment concentration profile at the inflow boundary and using the Van Rijn sediment transport formula we calculated the sediment load at Bahadurabad. A comparison between the calculated and the observed sediment load is shown in Fig.2.7c. A verification of the model for the water level at Sirajganj is shown in Fig.2.7d. In this study, the model was verified for the hydraulic conditions of the year 2012.



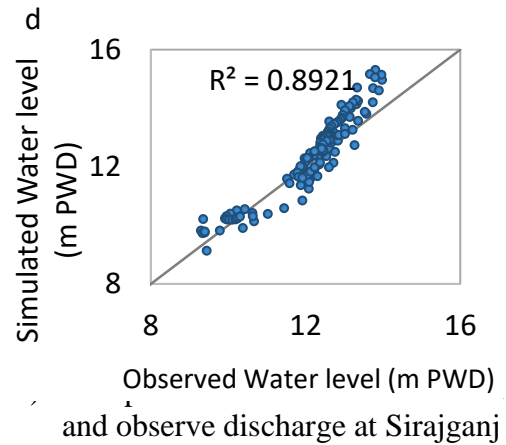
a) Comparison between simulated and observe discharge at Bahadurabad



b) Comparison between simulated and observe water level at Mathura



c) Comparison between simulated and observe sediment load at Bahadurabad



and observe discharge at Sirajganj

Fig.2.7 Calibration of the model for the hydraulic condition of the year 2011 (a,b and c) and validation of the model for the hydraulic condition of the year 2012 (d)

2.3 Results and Discussions

Methods of Analysis

Bar Migration

In this research, the migration rate for compound bars is defined and calculated. As the growth of the compound mid-channel bar is not unidirectional; merging of two or three

bars during the high flood is very common, we consider the highest lateral distance from the old one to newly developed one in a particular direction as the migration amount of that particular bar per unit time, ω_m for that particular year using the equation 2.51. The analysis was carried out considering the every bar as an individual object and it only reflects the annual alteration of the bar shape.

$$\omega_m = \frac{1}{l_{bn}} (a_{max})_{bn} \quad (2.51)$$

Where,

$(a_{max})_{bn}$ is the area of minimum bounding rectangle of determined by using Freeman and Shapira (1975), l_{bn} denotes the longer side length of the minimum bounding rectangle of determined by using Freeman and Shapira (1975)

a_{max} is determined by using the following algorithm equation 2.52 to 2.54

$$a_{max} = \max_j \{a_j\} \quad (2.52)$$

$$\Delta A = \sum_{j=1}^n a_j \quad (2.53)$$

[j =number of segments=1, 2, ..., n]

$$\Delta A = A_f - \sum_{i=1}^n A_i \quad (2.54)$$

Here,

A_f is area of new compound bar; A_i denotes area of old bars from which the compound bar is formed; ΔA defines newly accredited area of that particular compound bar; a_j is equal width segmented area to the mean flow direction; a_{max} Area of the largest segment a_j

Fig.2.8 shows a simple example of bar migration calculation definitions of a compound bar. Here, b_1, b_2 and b_3 (Fig.2.8a) are the old bars from which a new compound bar b_f (Fig.2.8 b) has been formed Fig.2.8c and d show the definition terms using in equation 2.32 and 2.33.

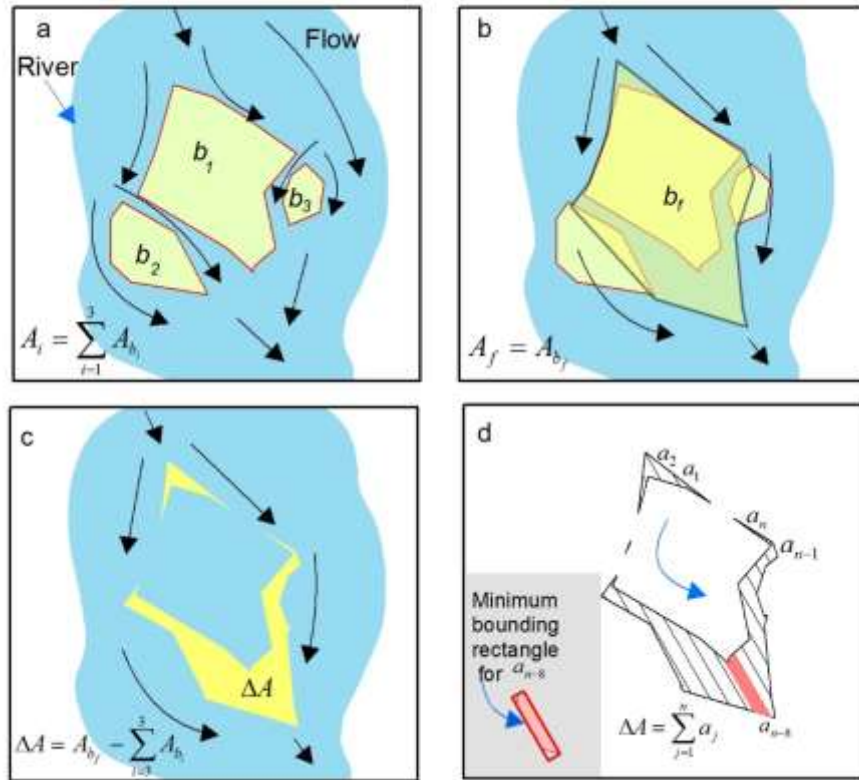


Fig.2.8 A schematic definition figure for bar migration calculation from satellite images

Bar properties

In the case of defining bar properties, we followed the definitions used by previous researchers, Garcia and Nino (1993), Schuurman et al. (2013) and Eaton and Church (2011). For determining bar length, one bar was treated as an individual object and the longest axis gave the length of the bar, L and the difference between trough and crest levels gave the value of bar amplitude, H . For dimensional analysis, dimensionless bar height H_b was calculated by dividing the Bar amplitude H by the maximum scour depth S_0 (S_0 represents the general scour due to fluvial erosion). The constant channel width of the river, W was determined by measuring the width of the bankline of the river of the year 2011 at every 10 km and calculating their average. This constant channel width, W was considered for estimating river's width/depth, β_b and it is defined by dividing this width by the monthly maximum water depth h_m within the simulation area. The relative migration rate, ω_m was defined by the ratio of migration rate of that particular bar to the monthly mean

flow velocity, U_o . Aspect ratio, α_b is defined by the bar length to width ratio, $\frac{L}{W}$. The

dimensionless stream power Ω^* was calculated by equation 2.55

$$\Omega^* = \frac{gh_m S U_o}{[g s d_{50}]^{3/2}} \quad (2.55)$$

a) Overall bed evolution and planform changes

The Planform from the satellite image and simulated one is shown in Fig.2.9a and b respectively and it can be said that the model can predict the main anabranch but in the case of the small scale morphology, there are some discrepancies as an example it could not predict well the alignment of chute channels Fig.2.9 c and d.

As the model was simulated only for one peak season, not huge bed level change was observed except in some confluence, huge scour (like 23.66 m PWD in Sirajganj) was observed (Fig.2.9b). Fig.2.10 shows an example of the cross-sectional change of river during the simulation period (cross-section was taken along Mathura water level measuring station). This figure indicates that higher erosion was observed in mixed bed case along the channel. However, the deposition over the bartop was quite smooth using the mixed bed model which represents better accuracy in vertical growth of bars.

Fig. 2.11 shows the histogram of bed level change by the calculation of model result. The distribution of bed level change data is bimodal type as it represents the distribution of two processes (erosion and deposition) combined into one dataset. This figure indicates the maximum frequency of deposition is around 0 to 1m. But the maximum frequency is 4m to 5m for erosion.

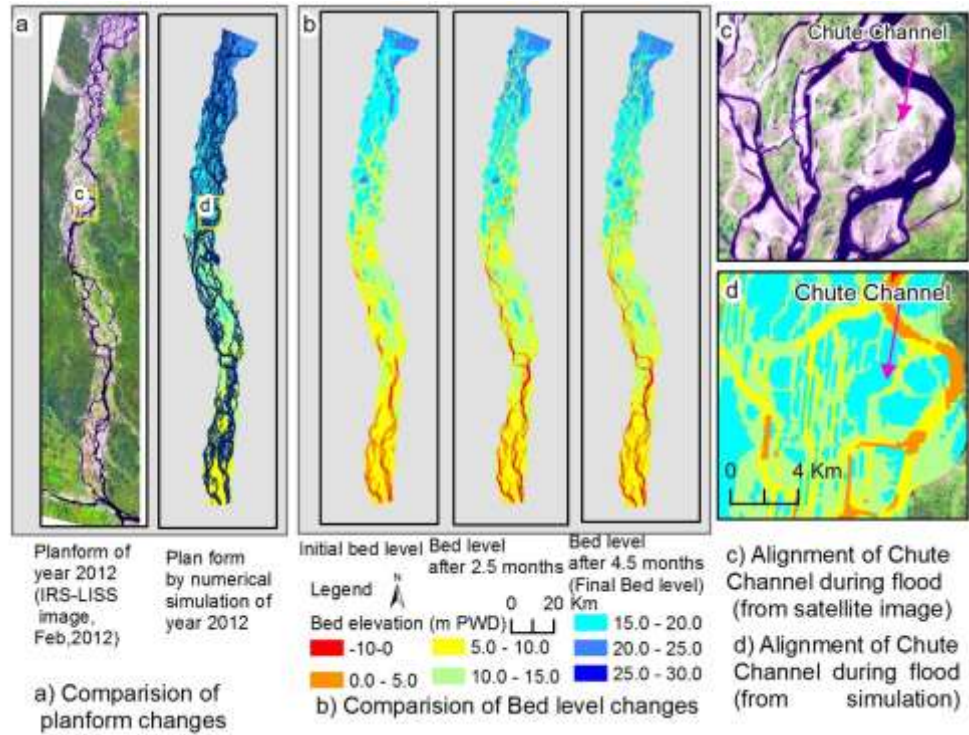


Fig.2.9 Comparison of real and simulated plan form and time series bed level change

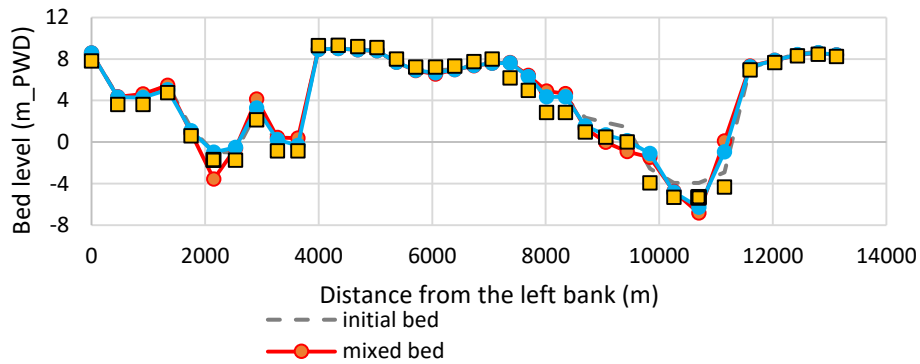


Fig.2.10 The comparison between initial and final bed level at Mathura due to mixed and uniform bed.

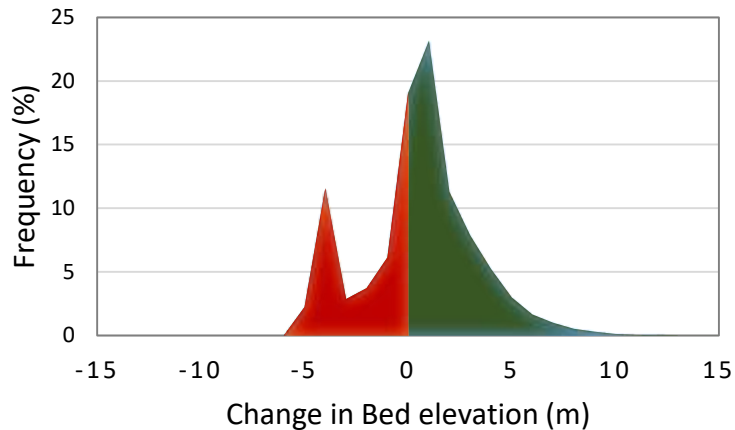


Fig.2.11 Histogram of bed level change

b) Migration of bars

An example of bar migration is shown in Fig. 2.12. Here the black line shows the area of the bar in 2011 or starting of simulation and the red line shows the area of the bar in 2012 or end of the simulation. The satellite image analysis indicates that the migration rate was 1.18 km while the simulation results indicate 1.10 km for that particular bar.

For the overall calculation of bar migration rate, all the bars (over 300 bars) were considered. Fig.2.13 shows the comparison of bar migration rate derived from satellite image and simulation. This figure indicates that the prediction of spatial bar growth by simulation is comparable to the actual one. Both the simulation results and satellite imagery analysis showed the migration rate of bar recedes with the growth of bar. The higher migration rate observed when the bar area was less than 25 square km. This rate is very high (3 or 2.5 km/year) when the bar area is less than 6 square km but after that, it becomes to 1.5 to 1 km/year. The average migration rate of bars is 1.05 km/year (standard deviation is 0.65 km/year) but satellite image analysis showed this rate was 0.04km/year (standard deviation is 0.21 km/year). In the case of estimating the migration rate from satellite images, the images represent the situation for dry period. The bars may experience some erosion during the end of monsoon to the dry period especially the small bars. But in the case of simulation, the migration rate was measured just after the monsoon season. Another reason behind this discrepancy is selecting the MF value. As mentioned earlier, this value has a very wide range and bed level adaptation or morphological changes depend on it.

c) Location of bank erosion

Fig.2.15 shows the comparison of river erosion location between the satellite image and model. During 2011 flood 27 locations are affected due to bank erosion. Among them 25 areas can be indentified by the model result from the magnitude of bed shear stress.

d) Bar properties

Here, bar properties have been analyzing considering the monthly change. From the simulation result, the dimensionless Bar height and Bar length are plotted in Fig.2.14 a and b (the data represents the monthly data). The results of the dimensionless Bar height, H_b analysis indicates that their good linear correlation with width/depth ratio, β_b .

But the dimensional less Bar length showed a nonlinear relationship with β_b and it seems there exist a critical value of L/W (here is 15000) beyond this the bar do not elongate laterally (Fig.2.14b). But the linear theory of bar indicates no such phenomenon for straight channel and meandering channels and according to this theory, this value increases with the increment of β_b .

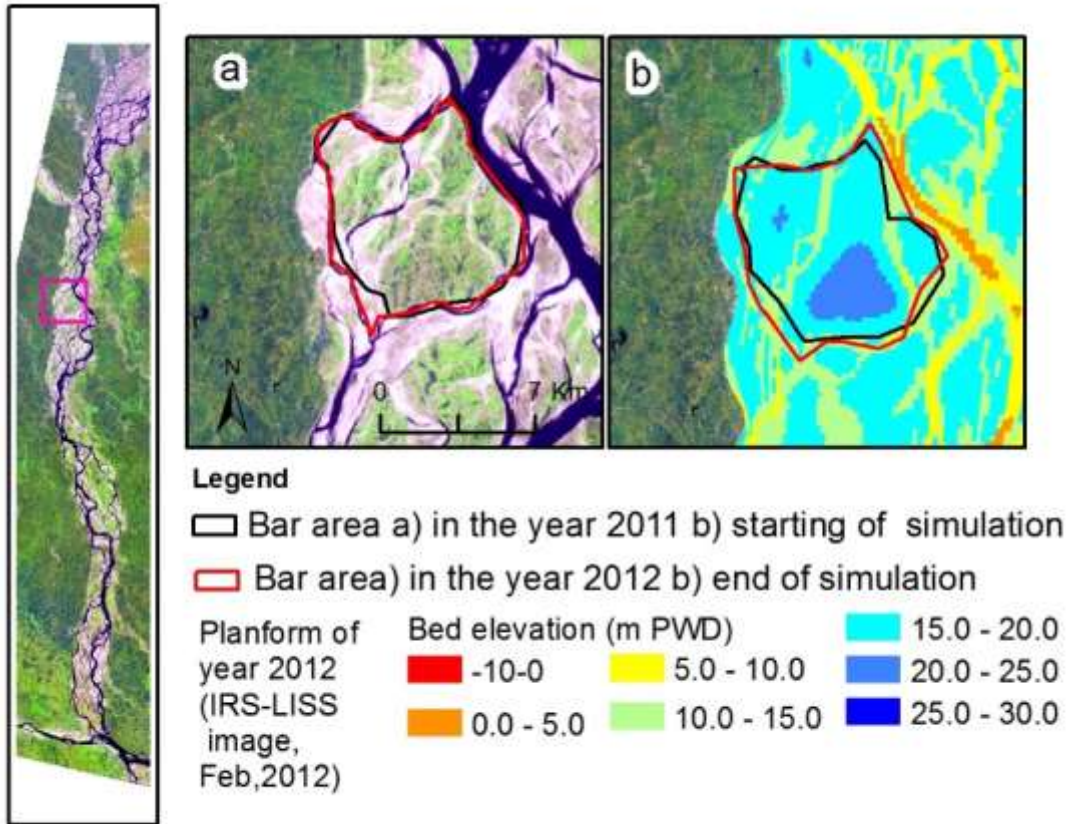


Fig.2.12 Map showing an example of bar migration of one bar.

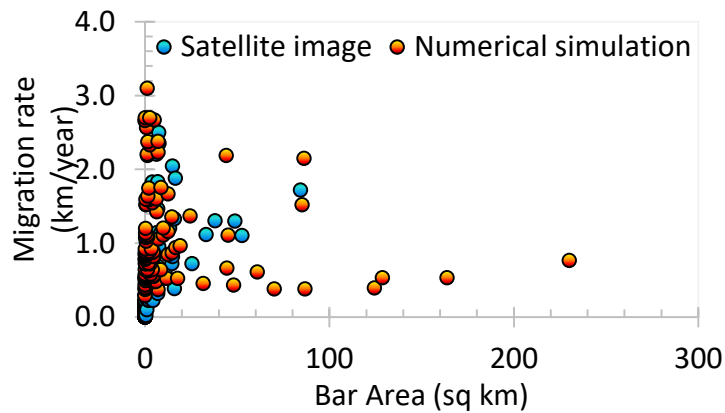


Fig.2.13 Comparison of Bar migration rate derived from satellite image analysis and numerical simulation

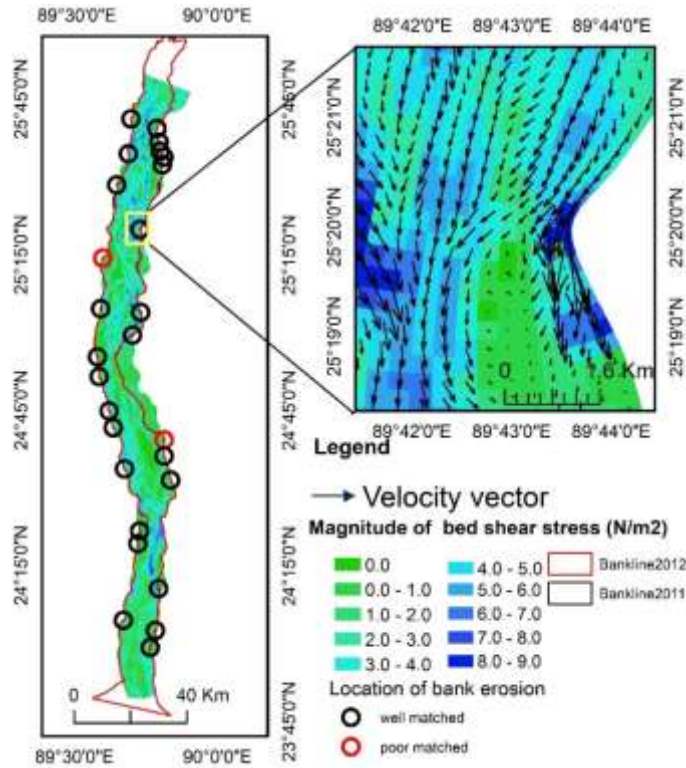


Fig.2.15 Comparison of river erosion location between the satellite image and model

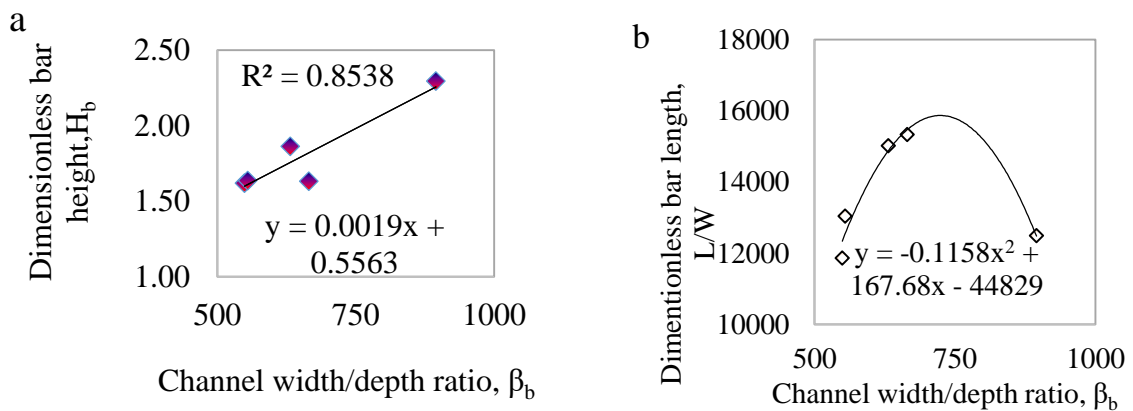


Fig.2.14 Relation between dimensionless width-depth ratios to a) dimensionless bar height b) dimensionless bar length

Fig.2.16 a, b and c show the relationship among dimensionless migration speed of bar as the function width/depth ratio β_b , bar aspect ratio, α_b and the dimensionless stream power, Ω^* (the data represents the monthly propagation). Fig.2.16 a indicates that with the

increase of width/depth ratio β_b from 549 to 665 the dimensionless migration rate also increases from 0.0024 to 0.019. Fig.2.16b reveals that the dimensionless migration rate is higher (0.019) for relatively low aspect ratio bar. Fig.2.16c indicates that with the increase of dimensionless stream power Ω^* , dimensionless migration decrease maintaining a nonlinear relationship.

Doeschl et al (2009) and Ashmore (2013) showed the change of bed elevation of other braided river using physics based model, laboratory experiment, and field data and summarized the similar type distribution which we got in bed elevation change histogram shown in Fig. 2.11. The rate of migration seems to be higher compared with the previous researches; Bridge (1993) estimated this rate was 500 m per year. But they considered only one mid channel bar in Brahmaputra-Jamuna for their analysis. The dimensionless analysis indicates that the bar height of braided bar behaves similarly as the bars in the straight channels or meandering one shown by Garcia and Nino (1993) but it shows the critical point in case of dimensionless bar length. This analysis indicates there may also exist suppression point

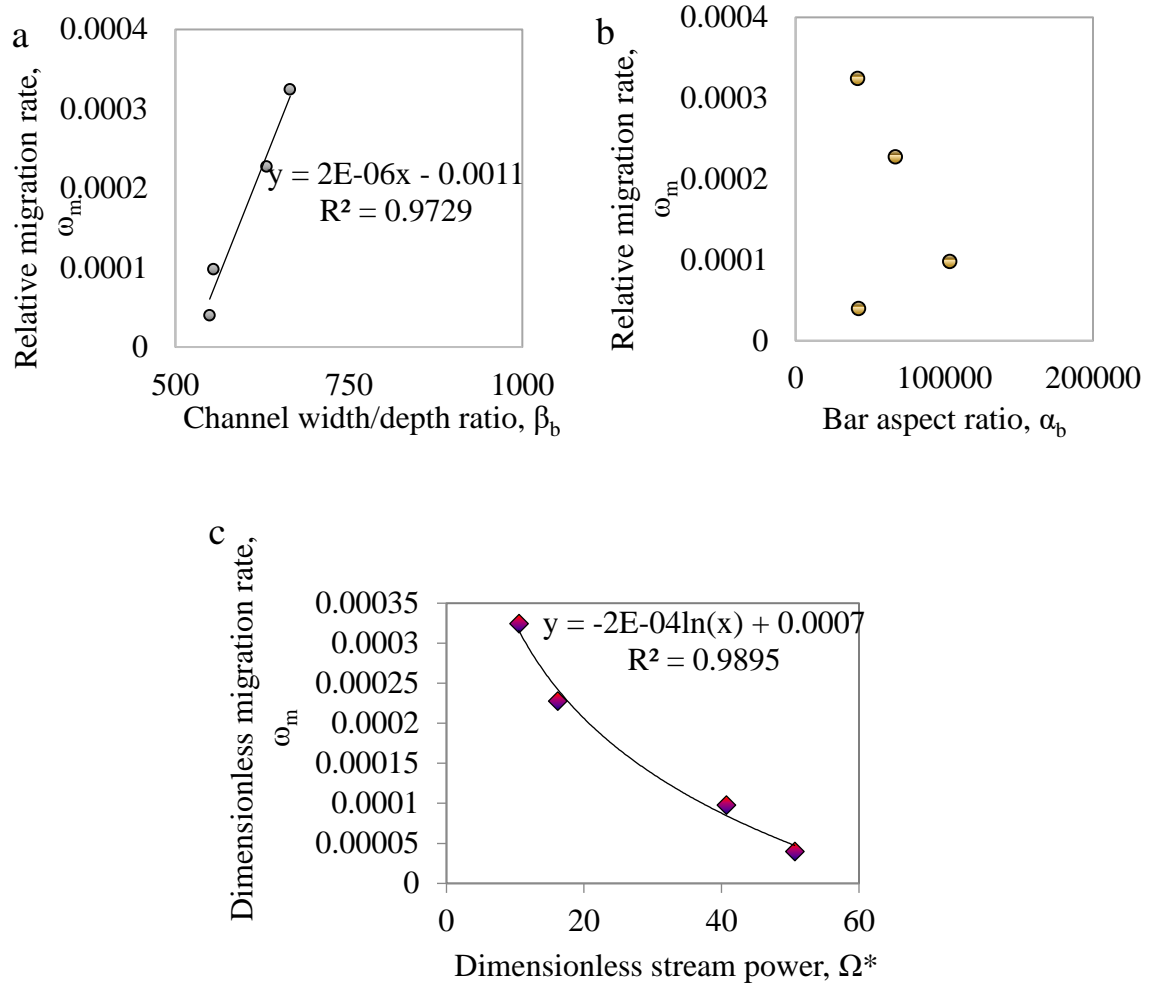


Fig.2.16 Relationship between Dimensionless migration speed to a) width-depth ratio b) bar aspect ratio and c) channel speed stream power for the braided bar in terms of $\frac{L}{W}$ ratio

These simulation results also indicate the bars in the upper part of the river experience lower average depth (Fig.2.9). This part also shows higher braiding intensity (Sarker et al.,2003). Sarker et al. (2003). Bertoldi et al. (2009) and Sarker et al. (2014) showed that the braiding intensity increases with the increasing of discharge both for gravel bed and sand bed braided river and our result of dimensionless migration rate and stream power analysis also indicated that higher stream power is less favorable for the spatial growth of bar. Therefore, it can be said that in this situation bar splitting process governs rather than migration process in case of bars with the relatively higher spatial area.

2.4 Summary

Using the 2D morphological model including the bed sorting phenomenon the prediction of the complex growth of compound bar dominated river reach can be done. However, finer bathymetry data is needed for simulating some small-scale property (e.g. formation of chute channel over the bar). Using the mixed bed model the vertical growth prediction over the bar were better than the uniform bed model.

The frequency of deposition on the river bed or braided plain was higher compared to the erosion due to the response of unsteady discharge and water level change in the study reach of the Brahmaputra-Jamuna for that particular year.

The dimensionless bar height behaves similar to the straight or meandering river but dimensionless bar length behaves differently. The dimensionless bar property analysis indicates the spatial growth of braided bar can be skillfully controlled by controlling the width-depth ratio and channel discharge. The migration rate of the bars naturally recedes with its growth. Hence, this phenomenon can also be used for better management of the braided river.

Chapter 3

Riverbank protection measures for braided river network

3.1 Problem identifications and countermeasures

The rapid change of braided channel geometry by changing the flow boundaries as a response of the interventions is the key management questions of the braided river (Piégay et al. 2006). Till now, the management techniques that are used in different parts of the world to manage the braided river include protecting the river bank by engineered structures, dredging or mining gravel from braided channels, regulating sediment from contributing tributaries, and destabilization of the bar by removing vegetation and afforestation the catchment. Piégay et al. (2006) examined different management techniques used all over the world to manage the braided river and suggest no unique solution to the problem. Now if the focus is made to study river reach of Brahmaputra-Jamuna, the most documented problem is river bank erosion (Baki and Gan 2012; Sambrook et al. 2009; Sarker et al. 2011a). Several countermeasures have already made to protect the river bank e.g. revetment with rip-rap different materials, hard point, permeable and impermeable spur as shown in Fig.3.1 (Nakagawa et al. 2013; Sambrook et al. 2009). In the next sections of this chapter a brief description about the performance of these structures are presented followed by the flow characteristics of the proposed countermeasure of this research. Table 3.1 shows a comparative analysis of the performance of the different type of structures. This analysis indicates that almost all type of structure partly or totally damaged when exposed to the main channel (Sarker et al. 2011a). However, compared to other type of structure protruding type structure (e.g. impermeable/permeable spur) experienced more damage (Nakagawa et al. 2013). But

Sambrook et al. (2009) showed that in Brahmaputra-Jamuna the structure cost per protected length (US\$/m) is almost 95% lower in case of spur-type structure. (Nakagawa et al. 2013).



Revetment with rip-rap

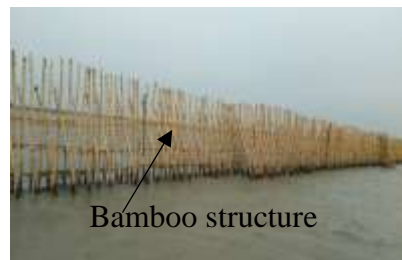


Revetment with Geo-bags

Hard point



Impermeable spur



Permeable spur

Bandal type structure (prototype)

Fig.3.1 River bank protection structure used in Brahmaputra-Jamuna (Nakagawa et al. 2013; Sambrook et al. 2009)

Table 3.1 Performance of bank protection structure of Brahmaputra-Jamuna (till 2011)
(Sarker et al. 2011a)

Category	Name of the structure	Construction period	Exposure		Damage
			Minor channel	Major channel	
Revetment	Titpara Revetment	2005-06		2005-11	Minor damage, effective
	Devdanga Revetment	2005-06		2005-08	Minor damage
	Sirajganj Revetment	1997-98		1998-11	Minor damage, effective
	PIRDP, Geobag revetment				effective
Hard point	Sariakandi	1997-98		1997-11	effective
	Sirajganj	1997-98		1998-11	effective
Guide bund	Bangabandhu Bridge guide bund	1996-98		1996-11	effective
Impermeable spur/groin	Hasnapur spur (No. of spur: 2)	2001-02	2002-03		Not exposed to main channel
	Kalitola groin	1997-98		1997-11	Minor and major damage but effective
	Chandanbaisa (bellmouth) groin	2001-02		2002-08	Damaged
	Baniajan spur	2001-02	2002-03		Not exposed
	Meghai Spur (No. of spur: 3)	1999-00	2000-01	2004	Damaged
	Singrabari spur (No. of spur: 2)	1998-99		2002-03	Damaged
	Shuvagacha spur (No. of spur: 2)	1999-00		2002-03	Damaged
	Simla spur (No. of spur: 3)	1999-01		2002-2005	Damaged
	Betil spur	2000-02	2001-04		Damaged
	Enayetpur	2000-02	2001-04		Damaged
Permeable spur	Kamarjani	1994-95		1995	Damaged

Spur dikes, the structures made to direct the flowing water as well sedimentation pattern, have already established their effectiveness in river management by protecting

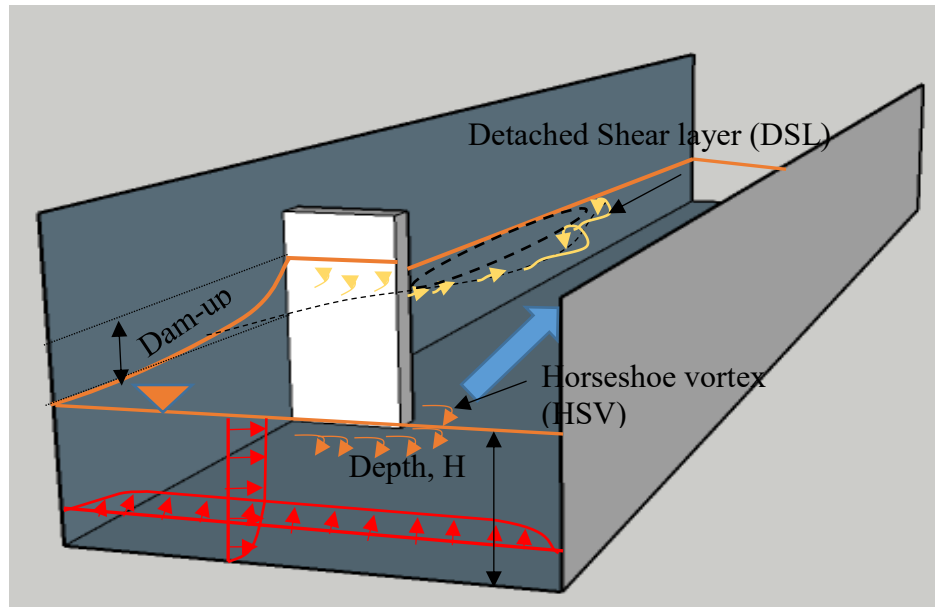


Fig.3.2 Conceptual description of flow distribution around a spur dike

riverbanks, improving navigation and providing eco-habitat both in gravel bed and alluvial rivers (Gisonni and Hager 2008; Gu et al. 2011; Kang et al. 2011; Koken and Constantinescu 2008; Nakagawa et al. 2013; Rajaratnam and Nwachukwu 1983; Uijtewaal 2005a). This type of structures also showed their efficiency in low land meandering rivers (Bhuiyan et al. 2002; Mosselman 2009; Przedwojski et al. 1995). But in case of highly sediment-laden alluvial braided river like Brahmaputra-Jamuna, these types of structures are not always successful due to the dynamic characteristics of the river and instability of the structure itself (Bhuiyan et al. 2002; Nakagawa et al. 2013; Paper et al. 2011; Sarker et al. 2011a). As mentioned in Table 3.1, the failure of spur/groin type of structures is quite frequent compared to other high-cost river training structures e.g. long embankment (Bhuiyan et al. 2002; Paper et al. 2011; Sarker et al. 2011a).

Generally, the presence of spur dike type of structures induces modification of flow by creating large-scale energetic flow features. Adverse pressure gradient immediately upstream of spur-dike, recirculation zone, formation of horseshoe vortex (HSV) system at the base of spur dike, development of wake zone, a fully turbulent and dynamic detached shear layer (DSL), vortex shedding phenomenon at the tip of the spur dike make the flow around the spur dike very complex as shown in Fig.3.2 (Ettema et al. 2006; Ettema and Muste 2004; Koken and Constantinescu 2008; Safarzadeh et al. 2016). These phenomena

particularly the HSV system accelerated flow at the tip, DSL produce large shear stress and turbulence at the spur tip which may undermine the spur in the river by producing large scour hole (Dey and Barbhuiya 2005; Klingemann et al. 1984; Li et al. 2006). Moreover, due to the highly dynamic nature of the braided channels, the river itself is scour-prone which exacerbated the local scour (Bhuiyan et al. 2002). Therefore, the detailed understanding of flow around such structure is crucial for the optimum design of spur dikes to manage this type of dynamic river.

Previous studies documented the use of spur dike in a particular river to achieve the specific purposes e.g. to ensure navigation depth, to protect the bank erosion, land reclamation or ecological richness by creating a stagnant zone (Ali et al. 2017; Cao et al. 2013; Gissoni and Hager 2008; Li and Altinakar 2016; Sarker et al. 2011b; Uijttewaal 2005b; Wu et al. 2005). However, field experiences and a number of laboratory studies recognized the occurrence of relatively large scour hole produced by totally impermeable spur dike field where the exchange of mass and momentum of sediment mainly occurred through the lateral turbulence exchange with the mainstream. But in case of impermeable spur in braided river due to the angled flow, bedform movement and rapid siltation or erosion in the downstream part create favorable condition of enlargement of the local scour (Bhuiyan et al. 2002; Copeland 1983; Duan 2009; Ghodsian and Vaghefi 2009; Gissoni and Hager 2008; Gu et al. 2011; Kang et al. 2011; Koken and Constantinescu 2008; Kuhnle et al. 2002; Kuhnle and Alonso 2013). As an alternate solution permeable spur dikes are introduced which produced less severe morphological consequences and become popular in the India, Bangladesh, USA, Netherlands etc. (Bakker et al. 1984; Raudkivi 1996a; Uijttewaal 2005a). However, this type of spur dike is reported very well for some rivers but in case of the wider one (high width depth ratio), the performance was questionable (Sarker et al. 2011a).

To overcome the above-mentioned situation, slit type (highly permeable pile spur; the width of the individual pile is very small compared to the channel width, the ratio of channel width/pile width is 200) permeable pile spur dike field is proposed in this research for secondary bank attached channel of braided river.

Raudkivi (1996b) investigated the permeable pile groin at the Baltic Sea and reported its efficiency by reducing turbulence intensity on the bed and large-scale

recirculation. Fukuoka et al. (2000) investigate the permeable groin considering the vegetation itself as permeable groin and focused to find its effectiveness on flood control and environment. Li et al. (2005) examined permeable groin as rubble mound structure using laboratory experiment and two-dimensional model focusing rubbles' geometry of the group of groins on the flow structure and flow force. Mioduszewski and Maeno (2005) examined the three-dimensional flow feature around a porous spur dike by developing the three-dimensional analytical model using the $k-\varepsilon$ model as turbulence closer and found some discrepancy at the downstream of the spur dike. Gu et al. (2011) using laboratory experiment compared the suspended sediment transport on a permeable spur dike field and impermeable one and concluded that the suspended sediment concentration decrease in the downstream direction due to sedimentation in the transition zone in case of permeable spur dike. They used a staggered-positioned group of poles as an individual spur dike. Kang et al. (2011) examined the permeability effect on a single groin by laboratory experiment and recommended a proper permeability to reduce velocity at groin tip. Therefore, it can be said that the definition of permeable spur dike differs in literature and study as a pile spur dike field is relatively low.

Hence, the main objective of this part of research is to identify the three-dimensional flow behaviors around a series of slit type spur dike field due to different installation arrangements. For this purpose, six experimental cases had been conducted which is described in next sections.

3.2 Laboratory experiments with slit type permeable spur dikes

3.2.1 Experimental Set-up

In our present science laboratory experiment plays a significant role for our understanding the physics act behind the permeable spur. In order to understand the flow property around a slit-type spur dike field, experiments were carried out under fixed bed condition in Ujigawa Open Laboratory, Kyoto University under fixed bed conditions. The flume was 10 m long with 0.8 m width and having a longitudinal slope of 1/300. The details of the experimental setup shown in Fig.3.3. Fig.3.3 (a), (b) and (c) describe the plan and sections of the flume. Fig.3.3 (d) shows a photograph of the flume for case 1. A continuous discharge of $0.01\text{m}^3/\text{s}$ was supplied from the upstream end of the flume. The five spur dikes were installed after 7m from the upstream end of the right bank. Each spur dike was made of a brass cylindrical piles having the diameter of 0.004 m. The spacing between two individual piles was 0.001m and longitudinal interval of each was 0.30 m. Total five spur dikes were installed having the permeability of 71% for all cases. Two types of installation were considered; one was setting the pile as squared grid type and the second was setting

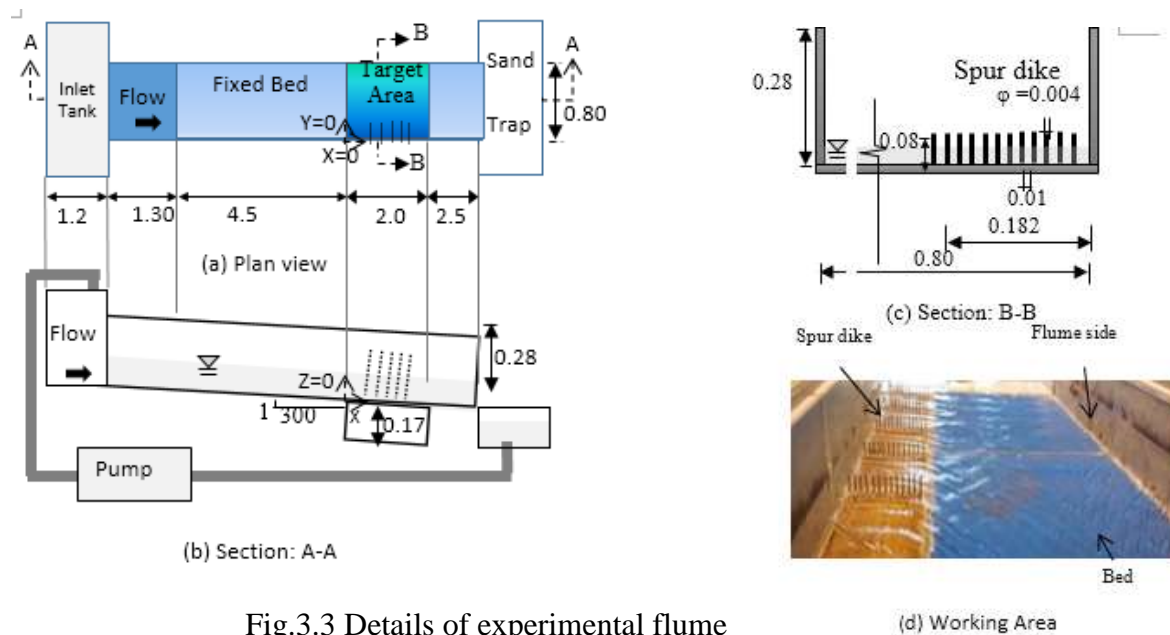


Fig.3.3 Details of experimental flume

them as staggered type (Table 3.2 and Fig.3.4). The approach flow depth was 0.032m and uniform flow was confirmed by adjusting the flume-end weir height. The details of the hydraulic condition of the flume were described in Table 3.3.

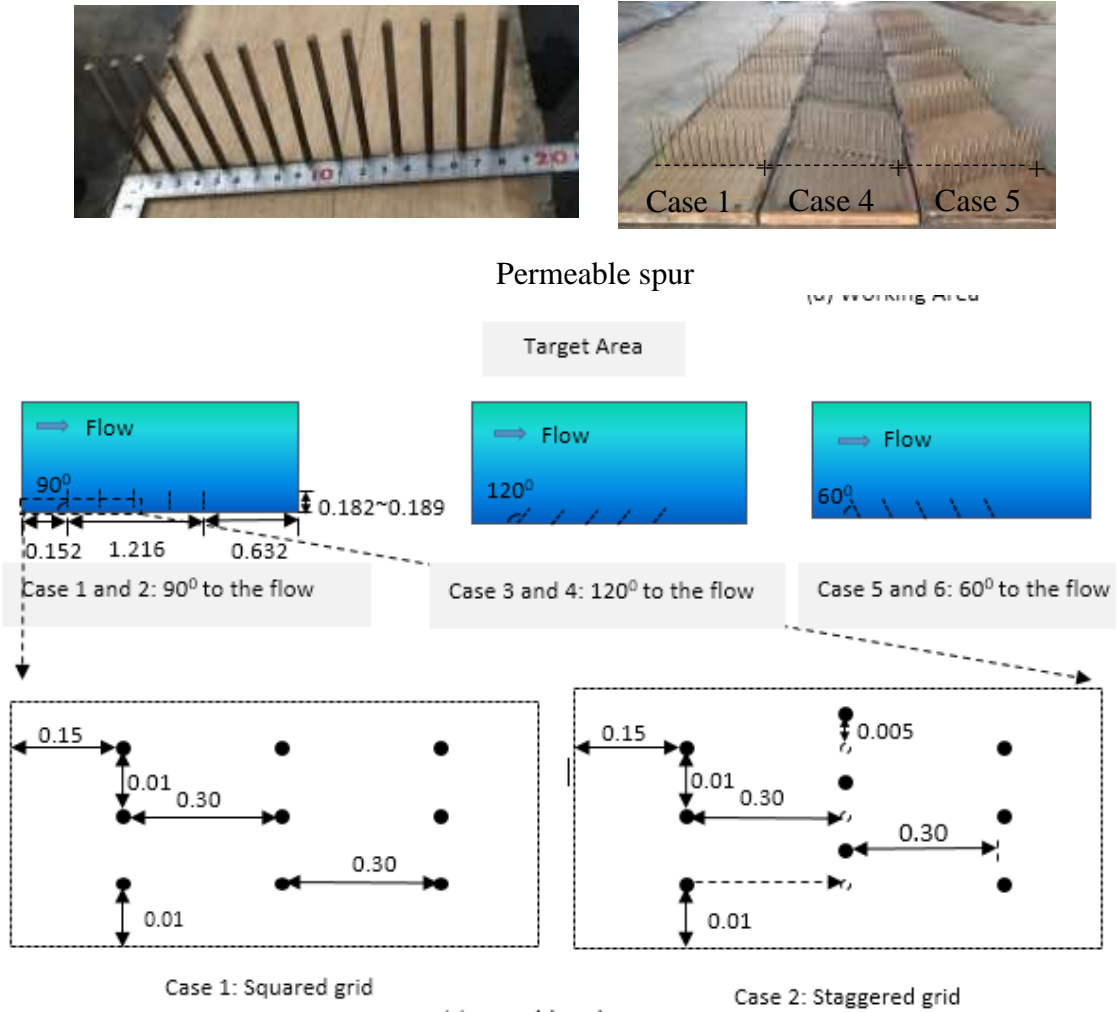


Fig.3.4 Spur dike model details

Table 3.2 Details of Experimental cases

Cases	Angles to the u/s flow (degree)	Installation Arrangement	Number of Spur dike	Number of piles in each Spur dike
1	90	Squared	5	13
2	90	Staggered	5	13
3	120	Squared	5	15
4	120	Staggered	5	15
5	60	Squared	5	15
6	60	Staggered	5	15

Table 3.3 Details of Experimental Conditions

Parameter	Unit	Values
Discharge, Q	m^3/s	0.01
Channel slope, S	-	1/300
Channel width, W	m	0.80
Approach Flow depth, h	m	0.032
Approach Flow Velocity, U	m/s	0.40
Friction Velocity, U_*	m/s	0.0323
Reynolds number, R	-	34430
Froude number, F	-	0.71
Approach Flow bed shear stress, τ_o	N/m^2	1.0464
Manning's n	$s/m^{1/3}$	0.015

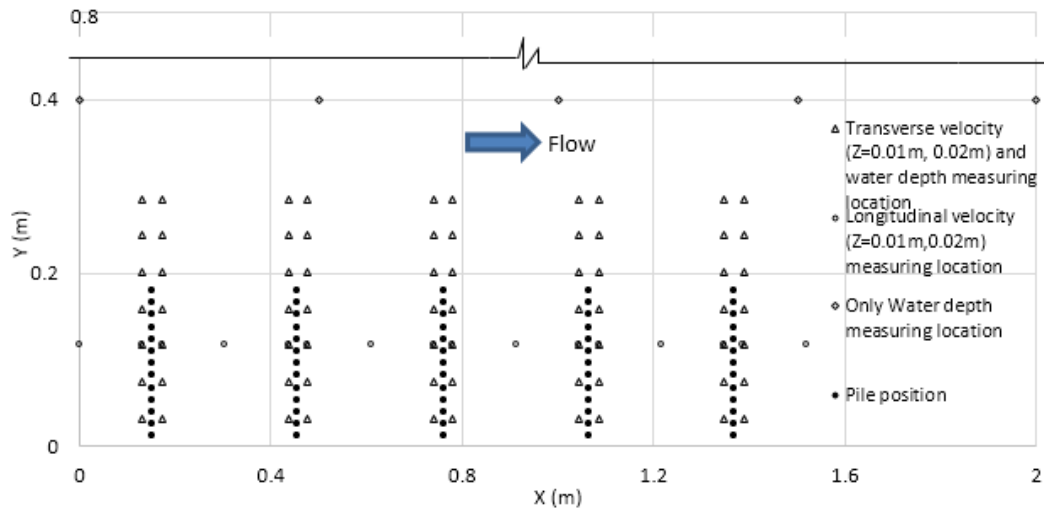


Fig.3.5 An example of experimental data measuring location (case 1)

3.2.2 Measurement techniques

The water depth was measured by using OMRON's ultrasonic water level sensor and Particle Image Velocimetry (PIV) method was used to measure the surface flow velocity. KENECK's L type electromagnetic velocity meter was used to measure the three-dimensional velocity (\bar{u} , \bar{v} , \bar{w}) components. An example of data measuring location for case 1 is shown in Fig.3.5. All types of velocity data were measured at the depth of $Z=0.01$ m and $Z=0.02$ m depth. The longitudinal velocity (\bar{u} , \bar{w}) data were measured 0.117m away from the right bank at a distance of 0.02 m from each individual spur as well as the middle point (0.152m away) of two consecutive spurs. The transverse velocity (\bar{v} , \bar{w}) and water depth were measured 0.02 m from each spur away at the same projected perpendicular location from the right bank. In addition, the flow depth was also measured at the mid channel (0.40 m away from the channel). A snapshot of the measurement equipment is shown in Fig.3.6.

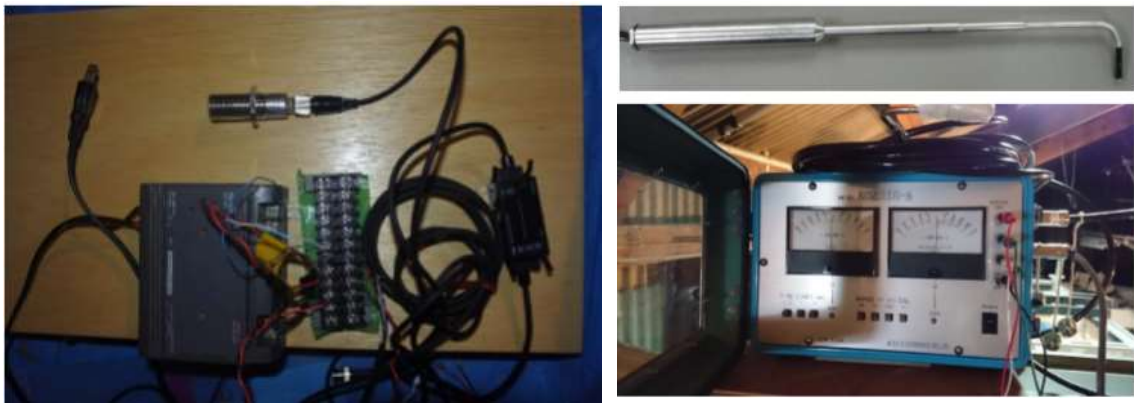


Fig.3.6 Measurement equipment used in the experiment. Left: OMRON's ultrasonic water level sensor; Right: KENECK's L type electromagnetic velocity meter

3.2.3 Results and Discussions

a) Longitudinal Velocity

Fig.3.7 shows the variation of dimensionless longitudinal velocity vectors $(\frac{\bar{u}}{U}, \frac{\bar{w}}{U})$ at a distance 0.11m away from the right bank. These figures indicates that the magnitude of longitudinal velocity ($\frac{\bar{u}}{U}$) vector varies from -0.09 to 1.1 within the spur dike zone. All the cases confirmed that just after passing the spur dike the downward component became stronger (Fig.3.8). Within the spur dike zone, the non-dimensional vertical velocity component was higher in 60° cases (the range varies between -0.20 to 0.16). No significant variation was observed between the squared type and staggered type cases in the distribution of the vertical velocity component. However, comparing the Fig.3.7 and Fig.3.8 it can be said that the longitudinal component worked as a significant component in this type of structure. However, as the permeability of the spur dikes are quite high, no strong recirculating flow was observed which was the similar observation of previous studies on permeable spur dikes. This observation is similar to Gu et al. (2011) and Kang et al. (2011). Kang et al. (2011) found no recirculation when the permeability over 60%. The maximum of average the magnitude of $\frac{\bar{u}}{U}$ was found in case 1 (Experimental: average=0.88, maximum=1.07). The minimum of average the magnitude of $\frac{\bar{u}}{U}$ was showed by case 4 (average=0.56, maximum=0.70,). Almost in all the cases, the squared type of installation showed almost 6% higher longitudinal velocity confirmed from both simulation and experiment. Within the spur dike zone, in perpendicular (case 1,case 2) and deflecting cases (case 5,case 6), the experimental results confirmed that the highest longitudinal velocity were observed around the first spur dike from the upstream but for the attracting cases the location of highest longitudinal velocity were different. For case 3, it was found after the 0.02m downstream of the fifth spur dike from the upstream. On the other hand, for case 4 it was found at 0.02m upstream of the first spur dike. This difference was happened due to the different installation position.

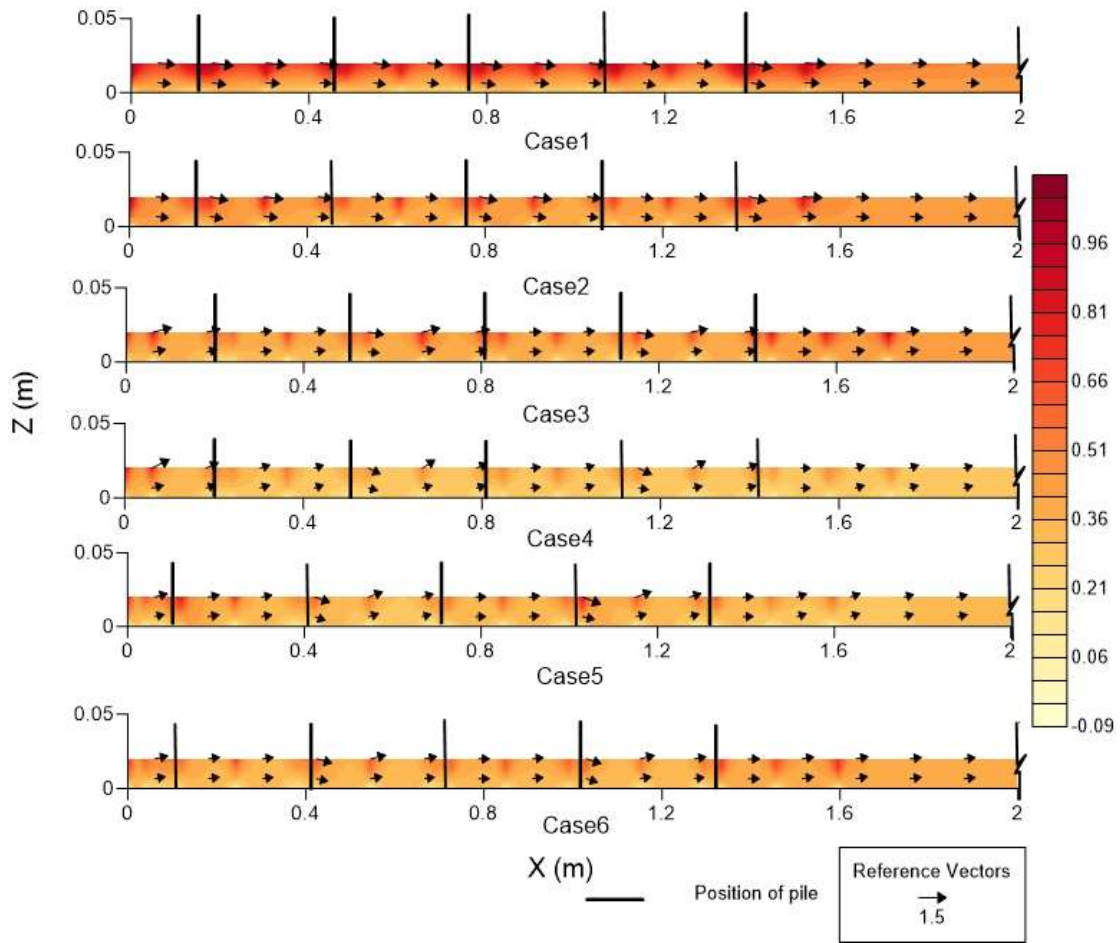
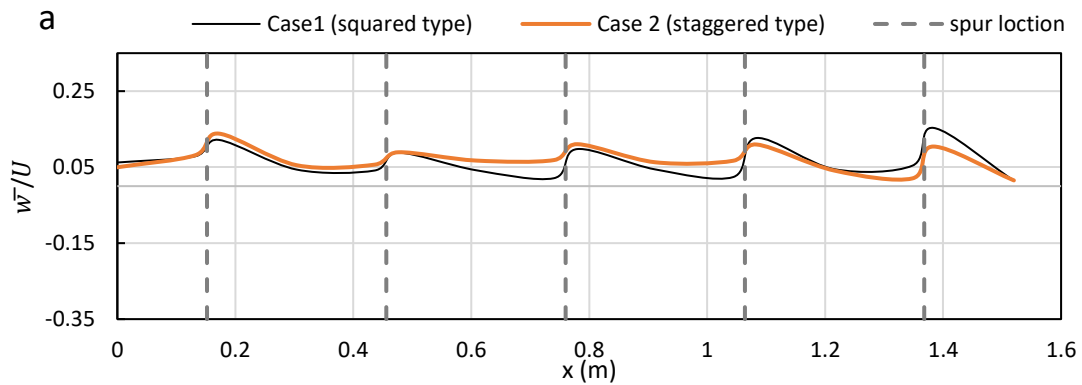


Fig.3.7 Dimensionless longitudinal velocity vector, $(\frac{\bar{u}}{U}, \frac{\bar{w}}{U})$ 0.11m away from the right bank. The contour shows the magnitude of the longitudinal velocity component ($\frac{\bar{u}}{U}$)



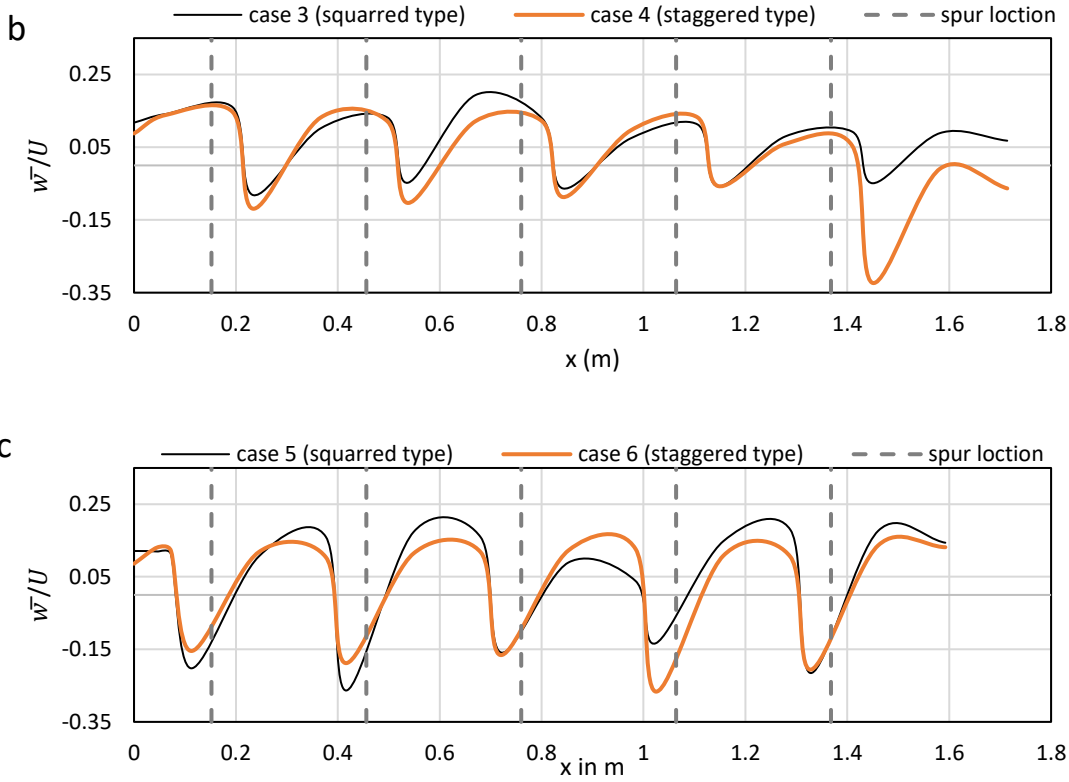


Fig.3.8 Longitudinal Distribution of non-dimensional Vertical Velocity Profile $\frac{\bar{w}}{U}$ at $z=0.01\text{m}$ of (a) 90° (b) 120° and (c) 60° aligned spur dike field

b) Transverse Velocity

Fig.3.9 shows the variation of the non-dimensional transverse velocity vector at 0.02 m upstream of the third spur dike. This figure indicates that the magnitude of dimensionless transverse velocity component $(\frac{\bar{v}}{U})$ varies from -0.035 to 0.3. The deflecting cases showed the higher transverse velocity and within the spur dike zone. The highest dimensionless transverse velocity was found in case 5. It is obvious from the figure that in case of transverse velocity, recirculation zone were observed in all the cases. In general, two recirculation zone were observed; one was near to the bottom and another was upper than that. For the perpendicular position of spur dikes (case 1, case 2) two clockwise rotating circulation was observed between which near bank circulation was smaller. For attracting cases (case 3 and case 4) the near bank circulation cell seemed to be larger compared to the perpendicular cases. In deflecting cases (case 4, case 5) one recirculation zone was observed with the spur dike zone. This pattern of the recirculating cell indicates

the presence of horse-shoe vortex and detached shear layer within the spur dike zone as indicated by previous researches (Koken and Constantinescu 2011; Melville and Coleman 2000; Safarzadeh et al. 2016; Zhang et al. 2013). The transverse distribution of vertical velocity profile along the same section has been plotted in Fig.3.10. Comparing the Fig.3.9 and Fig.3.10 it can be said that in the recirculating zone the upward vertical velocity component tends to increase. Fig.3.10 also indicates that in case of staggered type installation on the vertical velocity component lowered on an average 1.08 times.

c) Flow Depth

Fig.3.11 shows the variation of dimensionless water depth (d/h) (interpolated) around the spur dikes in the considered areas of the flume. It is evident from this figure that the depth of flow increases just upstream of the spur dike compared to immediately downstream of the spur dike in all cases. At the tip of the spur dike, the experimental results showed more variations than the simulated one because of the difficulties in measuring the rapid and sharp variation of water depth. However, the maximum dam-up was found in case 3 (experiment: 1.37). The squared type and staggered type of arrangement showed no significant difference (The difference in d/h between the staggered and squared type of installation was experiment: 0.06 and simulation: 0.22).

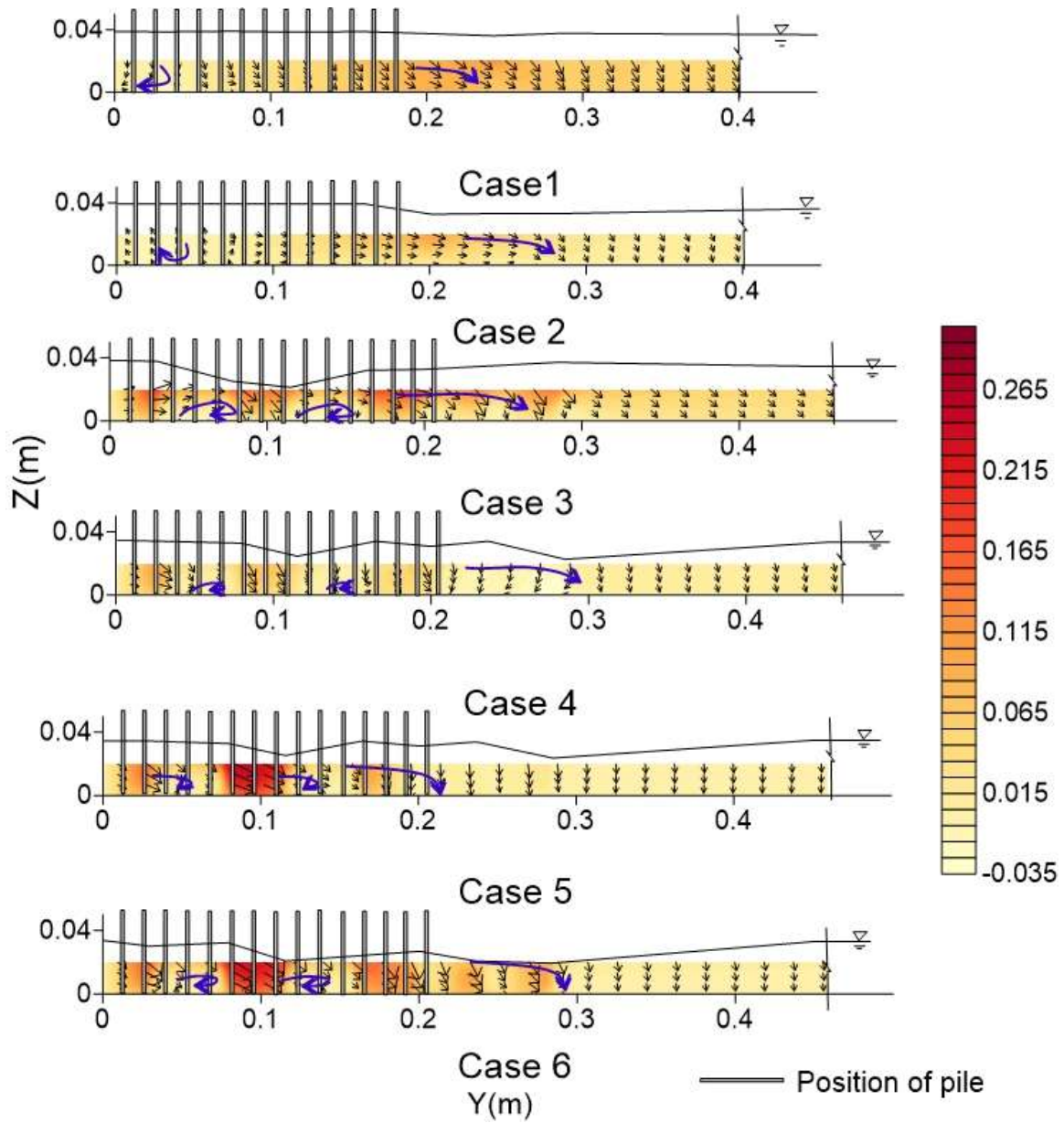


Fig.3.9 Dimensionless transverse velocity vector $(\frac{\bar{v}}{U}, \frac{\bar{w}}{U})$ at 0.02m upstream of third spur dike form the upstream. The contour shows the magnitude of the transverse velocity component $(\frac{\bar{v}}{U})$

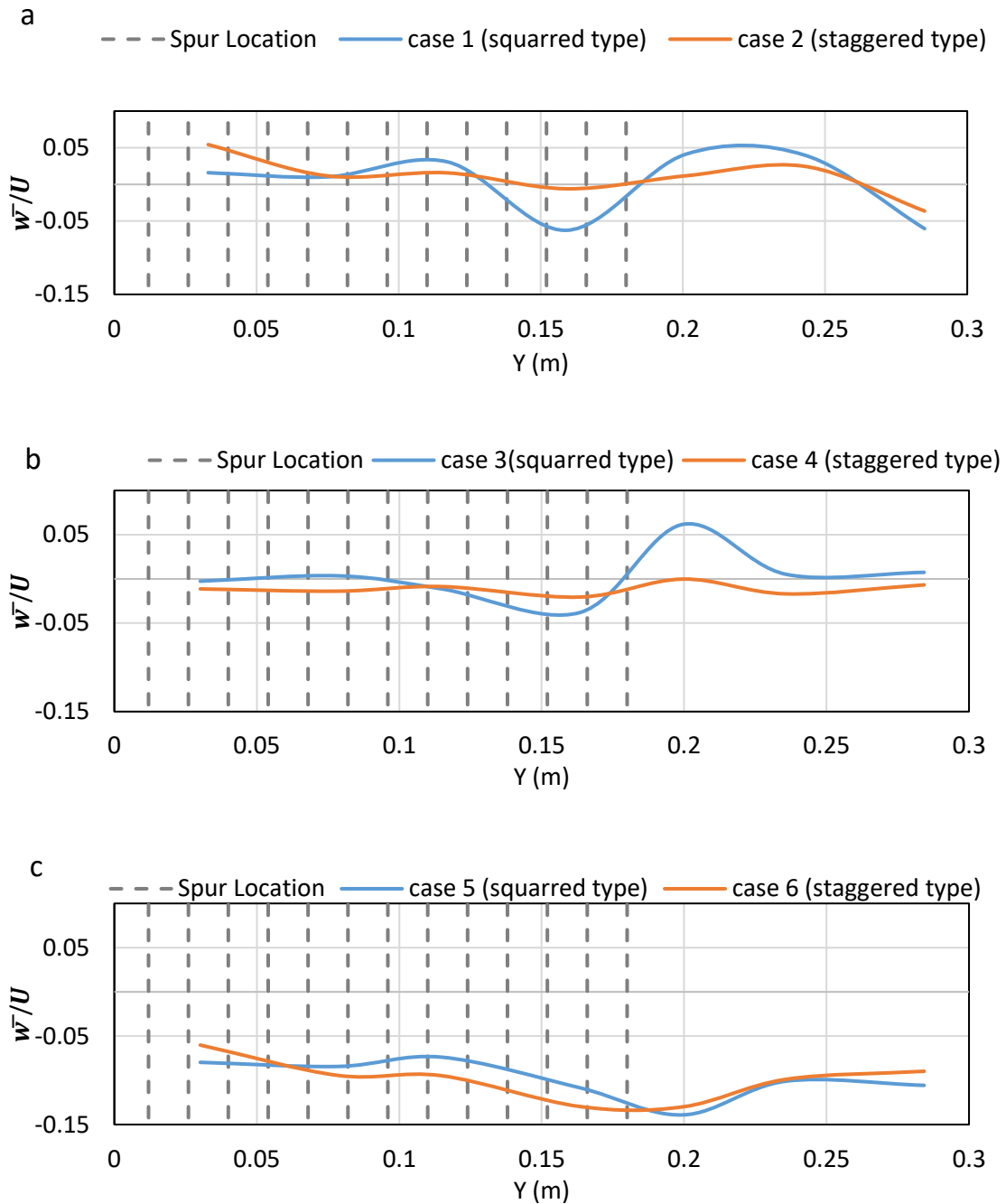


Fig.3.10 Transverse Distribution of non-dimensional Vertical Velocity Profile $\frac{\bar{w}}{U}$ at $z=0.01$ m of (a) 90° (b) 150° and (c) 60° aligned spur dike field

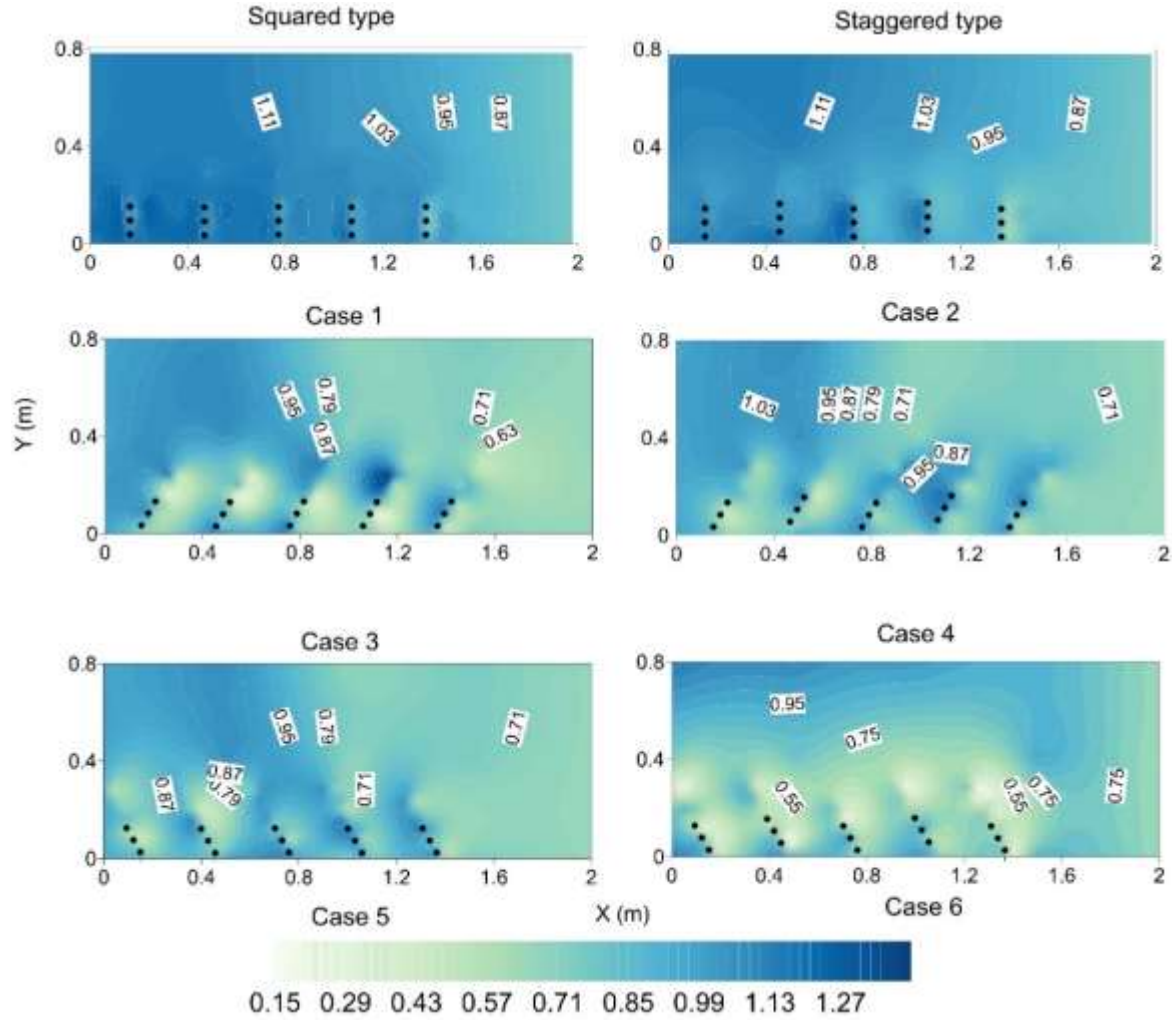


Fig.3.11 Spatial distribution of dimensionless water depth (d/h) of different cases

3.3 Three dimensional numerical model for experimental results

3.3.1 Governing equations

The numerical model was based on the three dimensional Reynolds averaged Navier-Stokes (RANS) equations with free surface as shown equation 3.1 and 3.2

$$\nabla \cdot \mathbf{U} = 0 \quad (3.1)$$

$$\frac{\partial \rho \mathbf{U}}{\partial t} + \nabla \cdot (\rho \mathbf{U} \mathbf{U}) = -\nabla p + \nabla \cdot \boldsymbol{\tau} + \rho \mathbf{g} + \rho \mathbf{f}_\alpha \quad (3.2)$$

Here, ∇ = gradient operator for three-dimensional region; \mathbf{U} = flow velocity vector; ρ = flow density; p = pressure; \mathbf{g} = gravitational acceleration vector and $\boldsymbol{\tau}$ = stress tensor,

and \mathbf{f}_α = the surface tension effects at the free surface. The equation 3.2 consists of the time-dependent and convective terms of the velocity on the left side, whereas the viscosity and the external forces on the right. The stress tensor can be obtained from the molecular and turbulent viscosity and given by the equation 3.3

$$\boldsymbol{\tau} = \mu_m (\nabla \mathbf{U} + (\nabla \mathbf{U})^T) + \rho \mathbf{R} \quad (3.3)$$

μ_m and \mathbf{R} are dynamic molecular viscosity and Reynolds stress tensor calculated from turbulence closure models respectively. It is needed to be mentioned that in RANS model the Reynolds decomposition of the velocity, \mathbf{U} into its mean, $\bar{\mathbf{u}}$ and fluctuating contributions, $\hat{\mathbf{u}}$ was done as shown in equation 3.4

$$\mathbf{U}(x, t) = \bar{\mathbf{u}}(x, t) + \hat{\mathbf{u}}(x, t) \quad (3.4)$$

Where the mean of the fluctuating component is defined as zero, $\overline{\hat{\mathbf{u}}} = 0$. The Reynolds stress tensor \mathbf{R} is obtained from the fluctuating velocity component using equation 3.5

$$\mathbf{R} = \overline{\hat{\mathbf{u}}\hat{\mathbf{u}}} \quad (3.5)$$

Assuming the Boussinesq eddy viscosity assumption, the momentum transfer caused by turbulent eddies can be modelled with an eddy viscosity as well as the momentum transfer caused by the molecular motion can be described by the molecular viscosity. And the Reynolds stress tensor is further divided into isotropic and deviatoric anisotropic contributions using equation 3.6

$$\mathbf{R} = \frac{2}{3} k \mathbf{I} + \mathbf{R}_{dev} \quad (3.6)$$

Here k is the turbulent kinetic energy, \mathbf{I} is unit tensor and \mathbf{R}_{dev} can be obtained using equation 3.7. Only the anisotropic contribution, \mathbf{R}_{dev} of the Reynolds stress tensor transports momentum (in equation 3.2), whereby the isotropic contribution, $\frac{2}{3} k \mathbf{I}$ was added to the mean pressure.

$$\mathbf{R}_{dev} = \vartheta_t (\nabla \mathbf{U} + (\nabla \mathbf{U})^T) - \frac{2}{3} k \mathbf{I} \quad (3.7)$$

Where ϑ_t denotes turbulent kinematic eddy viscosity.

$k - \omega$ SST model (Menter, 1994; Hellsten, 1998; Menter et al, 2003) was applied for turbulence closer. The turbulent kinetic energy, k ; the specific dissipation rate, ω ; and the turbulent kinematic eddy viscosity, ϑ_t were calculated by using equations 3.8, 3.9, and 3.10

$$\frac{\partial(\rho k)}{\partial t} + \rho[\nabla \cdot (kU)] = S_k - \beta^* \rho k \omega + \nabla[(\mu + \alpha_k \vartheta_t) \nabla(\rho k)] \quad (3.8)$$

$$\frac{\partial(\rho \omega)}{\partial t} + \rho[\nabla \cdot (\omega U)] = S_\omega - \beta \rho \omega^2 + \nabla[(\vartheta + \alpha_k \vartheta_t) \nabla(\rho \omega)] + (1 - F_1) \rho CD_\omega \quad (3.9)$$

$$\vartheta_t = \frac{a_1 k}{\max(a_1 \omega, SF_2)} \quad (3.10)$$

Where

$$S_k = \min(G_k, c_1 \rho \beta^* k \omega) \quad (3.11)$$

$$G_k = \vartheta_t S^2 \quad (3.12)$$

$$S_\omega = \frac{\gamma}{\vartheta_t} G_k \quad (3.13)$$

$$CD_\omega = 2\alpha_{\omega 2} \frac{1}{\omega} \nabla k \nabla \omega \quad (3.14)$$

Here S_k and S_ω denotes effective rate of production k and ω respectively. Where the two blending functions were estimated using equation 3.15 and 3.16 and $F_1=0$ in free stream and $F_1=1$ at any wall boundary layer. $\alpha_{k1}, \alpha_{k2}, \alpha_{\omega 2}, \beta^*, \beta, \gamma, c_1, a_1$ are turbulent model coefficient constant shown in

Table 3.4

$$F_1 = \tanh \left[\left(\min \left\{ \min \left(\max \left(\frac{\sqrt{k}}{\beta^* \omega y}, \frac{500 \vartheta}{y^2 \omega} \right), \frac{4\alpha_{\omega 2} k}{CD_{k\omega}^+ y^2} \right), 10 \right\} \right)^4 \right] \quad (3.15)$$

$$F_2 = \tanh \left[\left\{ \min \left(\max \left(\frac{2\sqrt{k}}{\beta^* \omega y}, \frac{500 \vartheta}{y^2 \omega} \right), 100 \right) \right\}^2 \right] \quad (3.16)$$

Where

$$CD_{k\omega}^+ = \max(CD_{k\omega}, 1e^{-10}) \quad (3.17)$$

$$\alpha_k = \alpha_{k1} F_1 + \alpha_{k2} F_2 \quad (3.18)$$

Table 3.4 Turbulent model constant

α_{k1}	α_{k2}	$\alpha_{\omega 1}$	$\alpha_{\omega 2}$	β^*	β	γ	c_1	a_1
0.85	1.0	0.5	0.856	0.9	0.075	0.5532	10	0.31

The volume of fluid (VOF) method was used to capture the free surface flow as described by Hirt and Nichols (1981). Therefore, along with the continuity and momentum equations, another transport equation (equation 3.19) which represents the volume fraction of one phase is solved simultaneously with these equations.

$$\frac{d\alpha}{dt} + \nabla \cdot (\alpha \mathbf{U}) = 0 \quad (3.19)$$

The phase fraction, α ranges from $0 \leq \alpha \leq 1$ e.g., $\alpha = 0$ for air and $\alpha = 1$ for water. The free surface was assumed on the volume fraction of 0.5. As the air and water were considered as two immiscible fluid, the physical properties of fluids are calculated based on the weighted average distribution of the liquid volume fraction. For example, the density of each cell was calculated using the equation 3.20

$$\rho = \rho_w \alpha + (1 - \alpha) \rho_f \quad (3.20)$$

Here, ρ_a and ρ_f denotes density of air and flow respectively. In equation 3.1 f_α represents the surface tension effects at the free surface which is calculated by using the equations 3.21 and 3.22. Where k_α is the curvature of the interface and σ_T is the coefficient of surface tension.

$$f_\alpha = \sigma_T k_\alpha \nabla \alpha \quad (3.21)$$

$$k_\alpha = -\nabla \cdot \left(\frac{\nabla \alpha}{|\nabla \alpha|} \right) \quad (3.22)$$

However, in free surface simulation the mass conservation should be confirmed in each phase and the surface curvature which is required for the determination of the surface tension and the pressure gradient across the free surface (Zhou 2017). Therefore, to ensure the mas conservation of the phase fraction, a modified transport equation is solved in as proposed by (Weller 2002) shown as equation 3.23.

$$\frac{d\alpha}{dt} + \nabla \cdot (\alpha \mathbf{U}) + \nabla \cdot \alpha \mathbf{U}_r (1 - \alpha) = 0 \quad (3.23)$$

Here, \mathbf{U}_r is the relative velocity as expressed as $\mathbf{U}_r = \mathbf{U}_f - \mathbf{U}_a$. The additional convective term in equation 3.23 is names as compression term and it serves an artificial contribution to the convection to make the free surface sharper (Berberović et al. 2009).

The term contains non-zero value within the interface region hence possess no influence in the single phase regions.

3.3.2 Discretization Procedure

Discretization is needed in order to transform the flow equations described in section 3.3.1 into a system of algebraic equations. The space is also needed to divide into a finite number of discrete regions, named as control volumes. Here Finite Volume method (FVM) of discretization was used. FVM methods discretize the integral form of governing equations over the control volume guaranteeing the conservation of mass and momentum at the discrete level. Equations are solved assuming a fixed Cartesian coordinate system on the immovable mesh. The method is supposed to be applicable to both steady and unsteady state calculations. The control volumes is a general polyhedral (prismatic and hexahedra) in shape with an adaptable number of neighbors, thus creating an unstructured mesh. The details of the procedure are described below. Here, firstly the discretization of space and then time will be described over a typical control volume.

The discretization of the solution domain composes discretization of time and space. It produces a computational mesh on which the governing equations are needed to be solved in space and time. A typical control volume is shown in Fig.3.12. The computational point P is located at the centroid of the control volumes which can be expressed as

$$\int_{v_p} (x - x_p) dV = 0 \quad (3.24)$$

The CV is bounded by a set of faces and each face is shared with only one face of neighboring CV. The cell faces can be separated into internal faces (between two control volumes) and boundary faces, which coincide with the boundaries of the domain. \mathbf{S} represents the face area vector which is constructed as normal for each face. Its direction is outward from the cell with the lower label to upper one and has the magnitude equal to the area of the face. The cell with the lower label is called the "owner" (whose centroid is shown by P) and upper label is named as the "neighbor" (centroid is shown by N). f represents the mid-point of the considered face.

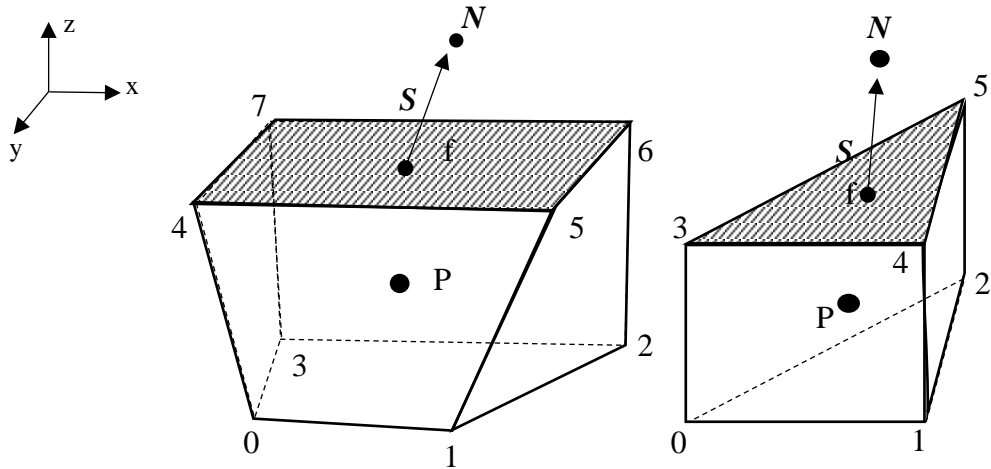


Fig.3.12 A typical control volume

The standard form of the transport equation for a scalar property ϕ can be written as equation 3.25

$$\underbrace{\frac{\partial}{\partial t}(\rho\phi)}_{\text{temporal term}} + \underbrace{\nabla \cdot (\rho U\phi)}_{\text{convective term}} = \underbrace{\nabla \cdot (\Gamma\nabla\phi)}_{\text{diffusion term}} + \underbrace{S_\phi(\phi)}_{\text{source term}} \quad (3.25)$$

The function ϕ was assumed to be linearized both in time and space and the accuracy achieved was in second order i.e. it is assumed that

$$\phi(x) = \phi_p + (x - x_p) \cdot (\nabla\phi_p) \quad (3.26)$$

$$\phi(t + \Delta t) = \phi^t + \Delta t \left(\frac{\partial\phi}{\partial t} \right)^t \quad (3.27)$$

Here $\phi(p) = \phi(x_p)$ and $\phi^t = \phi(t)$

The FVM requires the integration over a 3-D control volume V_p for the calculation point p for the time limit t to t + Δt , such that:

$$\int_t^{t+\Delta t} \left[\int_{V_p} (\rho\phi) dV + \int_{V_p} \nabla \cdot (\rho U\phi) dV \right] dt = \int_t^{t+\Delta t} \left[\int_{V_p} \nabla \cdot (\Gamma\nabla\phi) dV + \int_{V_p} S_\phi(\phi) \right] dt \quad (3.28)$$

For the discretization of spatial terms of equation 3.28 the generalized form of Gauss' theorem was used throughout the discretization. Therefore using the variation mentioned equation 3.26 the second order accurate discretized form of Gauss theorem can be expressed as

$$(\nabla \cdot \phi)V_p = \sum_f \mathbf{S} \phi_f \quad (3. 29)$$

Here, by \mathbf{S} is the outward pointing surface area vector and subscript f implies the value of the variable is in the middle of the face (the detail derivation of Gauss theorem in FVM can be seen in Jasak (1996)).

Discretization of convection term

Using the equation 3.29 the convection term of equation 3.28 can be written as

$$\int_{V_p} \nabla \cdot (\rho \mathbf{U} \phi) dV = \sum_f \mathbf{S} (\rho \mathbf{U} \phi)_f = \sum_f \mathbf{F} \phi_f \quad (3. 30)$$

Where \mathbf{F} is the mass flux through the face and can be expressed as

$$\mathbf{F} = \mathbf{S} \cdot (\rho \mathbf{U})_f \quad (3. 31)$$

The equation 3.17 and 3.18 requires the face value of ϕ in cell centers which can be obtained by the convection differencing scheme. As the convection differencing scheme, the second order accurate ‘‘Gauss linear’’ scheme was used which was bounded between 1 to 0.5.

Discretization of diffusion term

Similarly using the equation 3.29 the diffusion term of equation 3.28 can be written as follows

$$\int_{V_p} \nabla \cdot (\rho \Gamma \nabla \phi) dV = \sum_f (\rho \Gamma)_f \mathbf{S} \cdot (\nabla \phi)_f \quad (3. 32)$$

For discretization of equation 3.32 requires a selection of both an interpolation scheme for the diffusion coefficient Γ , and a surface normal gradient scheme $\nabla \phi$. For the interpolation, ‘‘central differencing’’ scheme was chosen and for the surface normal gradient scheme unbounded, second order, conservative ‘‘Gauss linear’’ scheme was applied.

Discretization of source term

All other terms of the original equation that cannot be expressed as convection, diffusion or temporal terms are treated as sources (Jasak 1996). The source term, S_ϕ , is generally a function of ϕ and should be linearized prior to discretization as follows:

$$S_\phi(\phi) = S_u + S_p \quad (3.33)$$

Here S_u, S_p are also the function of ϕ . Using the Gauss theorem the volume integral can be written as

$$\int_{V_p} S_\phi(\phi) dV = S_u V_p + S_p V_p \phi_p \quad (3.34)$$

Discretization of temporal term

To achieve temporal discretization, a linear variation in time is assumed. Hence, for any value ϕ can be expressed as

$$\phi^{t+\Delta t} = \phi^t + \Delta t \left(\frac{\partial \phi}{\partial t} \right)^t \quad (3.35)$$

Again considering the integral form of equation 3.28 and using the equations from 3.29 to 3.34, the equation 3.28 can be expressed as follows

$$\int_t^{t+\Delta t} \left[\left(\frac{\partial \phi}{\partial t} \right)_p V_p \sum_f F \phi_f \right] dt = \int_t^{t+\Delta t} \left[\left(\sum_f (\rho \Gamma)_f S \cdot (\nabla \phi)_f \right) + (S_u V_p + S_p V_p \phi_p) \right] dt \quad (3.36)$$

The above mentioned equation is usually called as the "semi-discretized" form of the transport equation (Hirsch C 2007). However several discretization methods are available to discretize these type of equations such as Crank-Nicholson, explicit discretization method, Euler Implicit method, Backward Differencing etc.

3.3.3 Pressure-Velocity Solution Procedure

The most commonly used pressure-velocity coupling procedure in fluid dynamics are pressure-implicit split-operator (PISO) (Issa 1985) algorithm, the semi-implicit method for pressure-linked equations (SIMPLE) algorithm (Patankar and Spalding 1972) and a combination both PIMPLE algorithm.

In SIMPLE algorithm, it is not necessary to fully resolve the linear pressure-velocity coupling. Through the solution of momentum equation, an approximation of the velocity field is attained. The pressure gradient term is calculated using the pressure distribution from the previous iteration. Then new pressure equation is formulated and solved for that time step. Velocities are corrected according to this and a new set of conservative fluxes is calculated (Zhou 2017). In this method the discretized momentum equation and pressure correction equation are solved implicitly, where the velocity correction is solved explicitly.

PISO algorithm is known for solving the PISO loop. Firstly the momentum equation is solved to calculate the velocity field using the initial pressure gradient values commonly known as 'Momentum Predictor' step. The velocity field obtained in the first step and then corrected using the updated estimate of the pressure field. This estimation-correction iterative procedure are repeated until the difference some threshold value. Lastly the new conservative fluxes are calculated (Zhou 2017).

When using PISO algorithm, to ensure the stability of the simulation the time step should be limited by Courant number, $Co < 1.0$. It is very computationally expensive to solve a real time problem with very complex geometries. In order to accelerate the simulation, a combination of SIMPLE and PISO algorithms is conceivable which allows the time step to reach $Co \geq 1.0$ and is named as the PIMPLE algorithm. In the PIMPLE algorithm the looping is controlled by different user defined parameters. For example the iteration number of pressure-velocity loop, explicit non-orthogonal correction etc.

As a summery it can be said that in this study the PIMPLE algorithm was used to couple pressure and momentum quantities. The PIMPLE algorithm was chosen for better stability of the model while using larger time step compared to PISO or SIMPLE algorithm. For numerical scheme of time derivatives, Euler methods was used. Gaussian scheme combined with van Leer method was used as the divergence scheme. For laplacian scheme Gauss linear (limited) was used. The numerical analysis was performed by using open source interFoam solver within the open source software code of OpenFOAM (version 4.1).

3.3.4 Rough Wall Treatment

For any turbulent flow conditions, the velocity profile can be divided into three major layers - the viscous sublayer, the logarithmic or turbulent layer and the velocity defect layer (Fig.3.13) (Kalitzin et al. 2005). Between the viscous and turbulent sublayer there exists one buffer layer. In general the extent and the outer edge of the turbulent layer depends on the Reynolds number and is well defined. However, in a quasi-equilibrium boundary or buffer layer, the profiles of the flow variables collapse when scaled with the friction velocity u_s and molecular viscosity. This universality allows the derivation of wall functions. However, the wall functions used in this study is presented below.

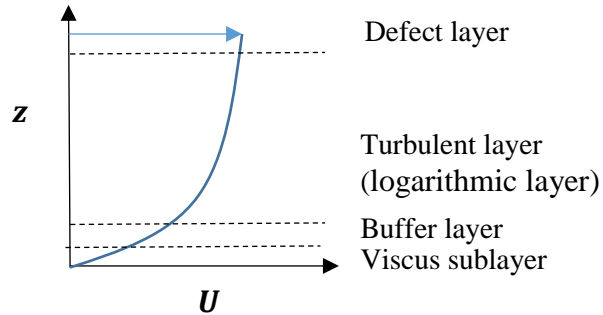


Fig.3.13 Schematic diagram of vertical velocity distribution

Near-wall region should be defined for appropriate use of wall functions. Some parameters which be used to introduce the near wall region

$$y^+ = \frac{y \times u_*}{\nu} \quad (3.37)$$

Here, y is the distance to the wall and y^+ is a non-dimensional parameter. The value of y^+ of the first cell is essential to know its location. The dimensionless velocity is given by

$$u^+ = \frac{u}{u_*} \quad (3.38)$$

In the viscous sublayer ($y^+ < 5$), $y^+ = u^+$

In the logarithmic area ($30 < y^+ < 200$), $u^+ = \frac{1}{\kappa} \ln(Ey^+)$

E is smooth wall constant

In the Buffer layer viscous and turbulent stresses are of similar magnitude. The treatment used here is using the linear relation as that in viscous sublayer and use logarithmic function as that in logarithmic region. In this study the following wall functions are used.

kqRWallfunction: This is a boundary condition for k field which is actually a zero gradient condition

omegaWallfunction: It provides a wall constraint on turbulence specific dissipation ω for turbulence models. In the near wall cells, the values for ω are calculated as

$$\omega_{vis} = \frac{6(\mu_m + \vartheta_t)}{\beta z_p^2} \quad (3.39)$$

$$\omega_{log} = \frac{\sqrt{k}}{C_\mu^{1/4} \kappa z_p^2} \quad (3.40)$$

z_p is the distance from the wall to the first center near the wall; C_μ denotes turbulence closure coefficient.

nutRoughWallfunction: This is a boundary condition for ϑ_t field. The kinematic eddy viscosity in the grid cells closest to the wall is therefore calculated by

$$\vartheta_t = \mu_m \left[\frac{y^+ \kappa}{\ln \left\{ \frac{E}{1 + C_s k_s^+} \right\}} - 1 \right] \quad (3.41)$$

C_s defines roughness constant of wall function, k_s is the Equivalent roughness height.

3.3.5 Model schematizationin

Hybrid mesh consisting triangles, quadrangles and prisms were used in the simulations. An example of a computational is shown in Fig.3.14. Five domain patches are considered- inlet, outlet, bed, atmosphere and wall (which includes spur dikes). The simulation conditions were kept same as of the experimental conditions. Table 3.5 shows the boundary conditions used in the simulations for all cases. A detailed description and definitions of the boundary types can be found in the (Weller et al. 1998; OpenCFD 2009; NEXT Foam 2013). The calculation condition was as same as the experiments as variable height velocity induced by the $0.01\text{m}^3/\text{s}$ supply of discharge at upstream was given at the inlet (variableHeightFlowRateInletVelocity), enabling the free water level oscillation (variableHeightFlowRate) and a constant total pressure in the outlet, p_0 . No slip condition was applied to the walls as a velocity boundary. The upper surfaces of the mesh was considered as atmosphere, therefore the flow was allowed to enter and leave the into main domain freely by applying pressureInletOutletVelocity condition as velocity and

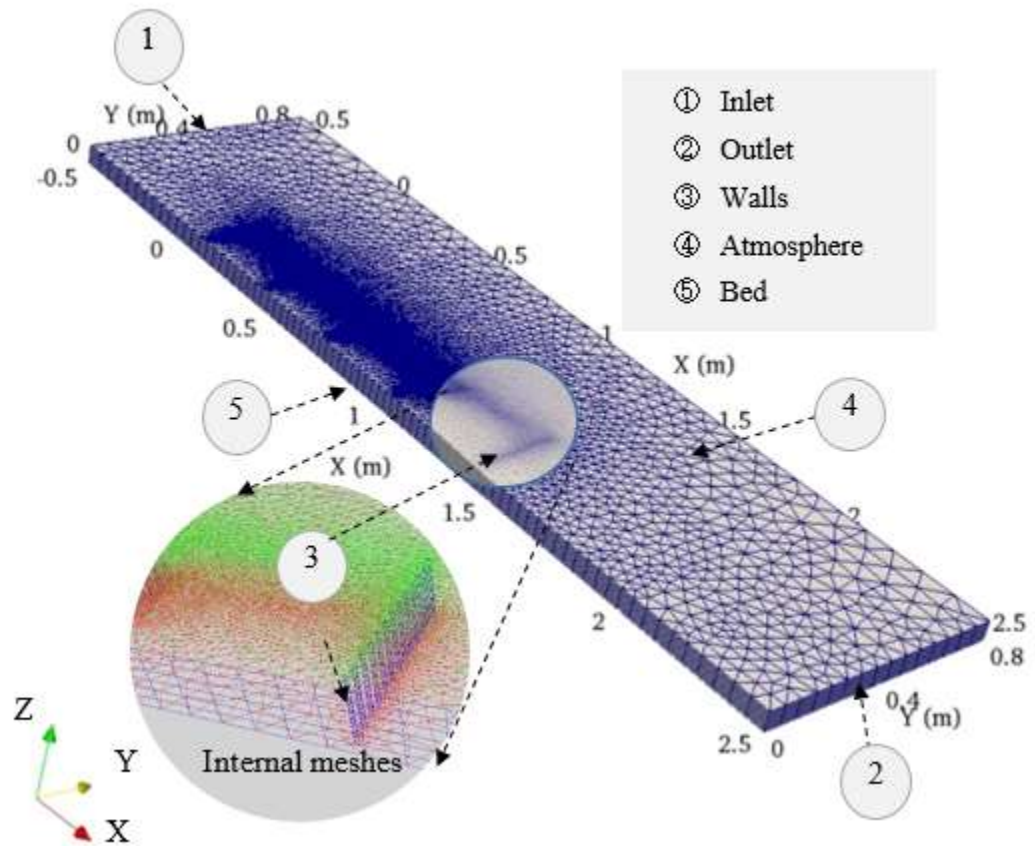


Fig.3.14 An example of computational mesh (case 1)

flow domain near the wall like structure. `kqRWallFunction`, `omegaWallFunction`, `nutUSpaldingWallFunction` were applied to the walls as the turbulent boundary conditions.

Table 3.5 Boundary conditions of the simulations

Domain Patch	Velocity, U	Pressure, p	Turbulent kinetic energy, k	Specific dissipation rate, ω	Turbulent kinematic eddy viscosity, ν_t	Phase fraction, α
Inlet	variableHeightFlowRateInletVelocity	zero gradient	Uniform fixed value	Uniform fixed value	Uniform fixed value	variable HeightFlowRateInlet
Outlet	pressureInletOutletVelocity	totalPressure	internalField	Uniform fixed value	Calculated from other patch fields	inletOutlet
Walls	noSlip	zero gradient	kqRWallFunction	omegaWallFunction	nutUSpaldingWallFunction	zero gradient
Atmosphere	pressureInletOutletVelocity	totalPressure	uniform fixed value	inletOutlet	Calculated from other patch fields	inletOutlet
Bed	noSlip	zero gradient	kqRWallFunction	omegaWallFunction	nutUSpaldingWallFunction	zero gradient

3.3.6 Model verification

The numerical simulation was verified with the measured experimental data. An example of a comparison of surface velocity derived from PIV method and simulation of case 1 is shown in Fig.3.15. This figure indicates that the numerical model is capable to capture the surface flow direction, like as the experimental velocity the numerical simulation also showed the lower velocity in the spur dike zone. However, the comparison of three-dimensional velocity ($\bar{u}, \bar{v}, \bar{w}$) and water depth were also made for each data measuring location and an example of that are shown in Fig.3.16. Fig.3.16(a) shows the comparison of longitudinal velocity (\bar{u}, \bar{w}) at 0.117 m ($Z=0.02$ m) away from the right bank inside the spur dike zone and Fig.3.16(b) transverse velocity (\bar{v}, \bar{w}) magnitude at 0.02m ($Z=0.02$ m) upstream from the third spur dikes. Fig.3.16(c) shows the water depth at the identical location with the transverse velocity. In spite of some differences these,

figure indicates satisfactory agreement between the two. However, the performance of the model was assessed using the equation 3.42 and the value of PBIAS of all measuring points for water depth and velocity are shown in Table 3.6.

$$PBIAS = \left(\frac{\sum_{i=1}^n S_i - \sum_{i=1}^n O_i}{\sum_{i=1}^n O_i} \right) * 100 \quad (3.42)$$

Here S_i represented the simulated values and O_i represents the experimental values.

Previous researchers (D. N. Moriasi et al. 2007; Santhi et al. 2002; Bracmort et al. 2006) reported the satisfactory range of PBIAS is $0 \leq PBIAS \leq 25\%$. By comparing with Fig.3.16 it can be said that all the cases discussed here showed the results within this acceptable range. However, In case of water depth, the simulation result was under estimated in case 1 but the other cases showed slight over estimation (maximum 11.8%). The velocity magnitude results of the simulations showed overestimation in case 4 and 5 but the other cases showed underestimation (maximum 18.1%). It should be considered at the same time that PBIAS only indicates the average tendency of simulated data to be greater or smaller than the experimental data (Gupta et al. 2001).

Table 3.6 PBIAS of the considered cases

Cases	Water Depth	Velocity magnitude
Case1	-5.063	-11.058
Case2	3.314	-18.120
Case3	1.339	-15.928
Case4	8.766	3.791
Case5	9.830	8.684
Case6	11.825	-6.279

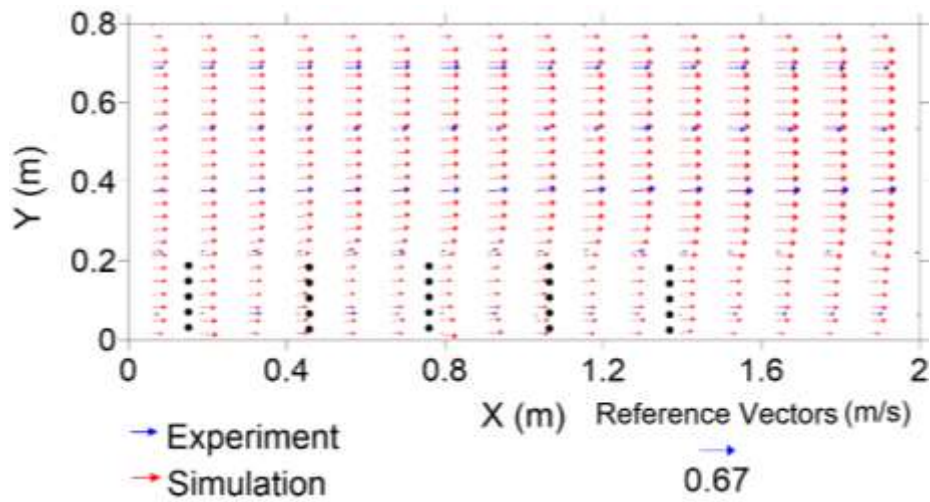
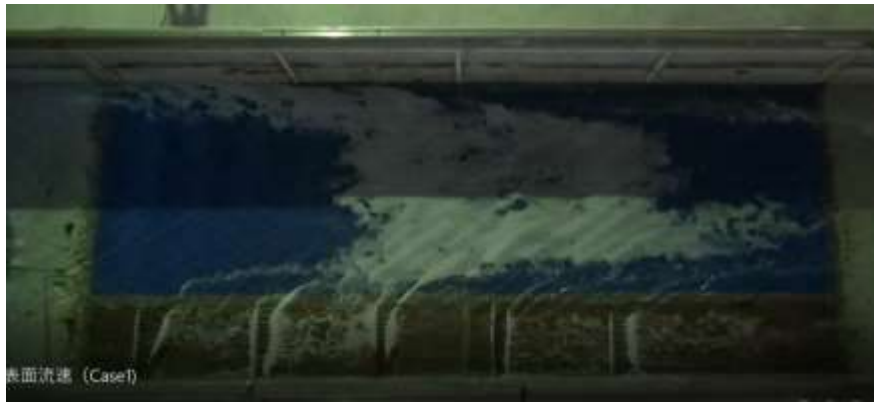
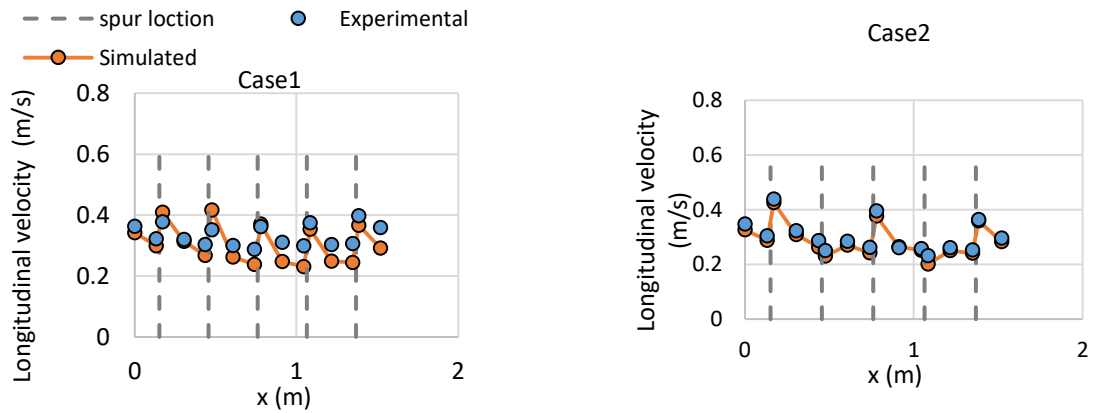
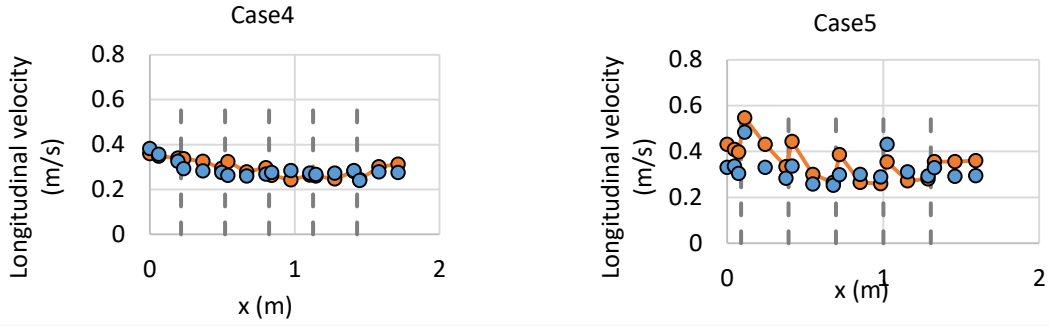
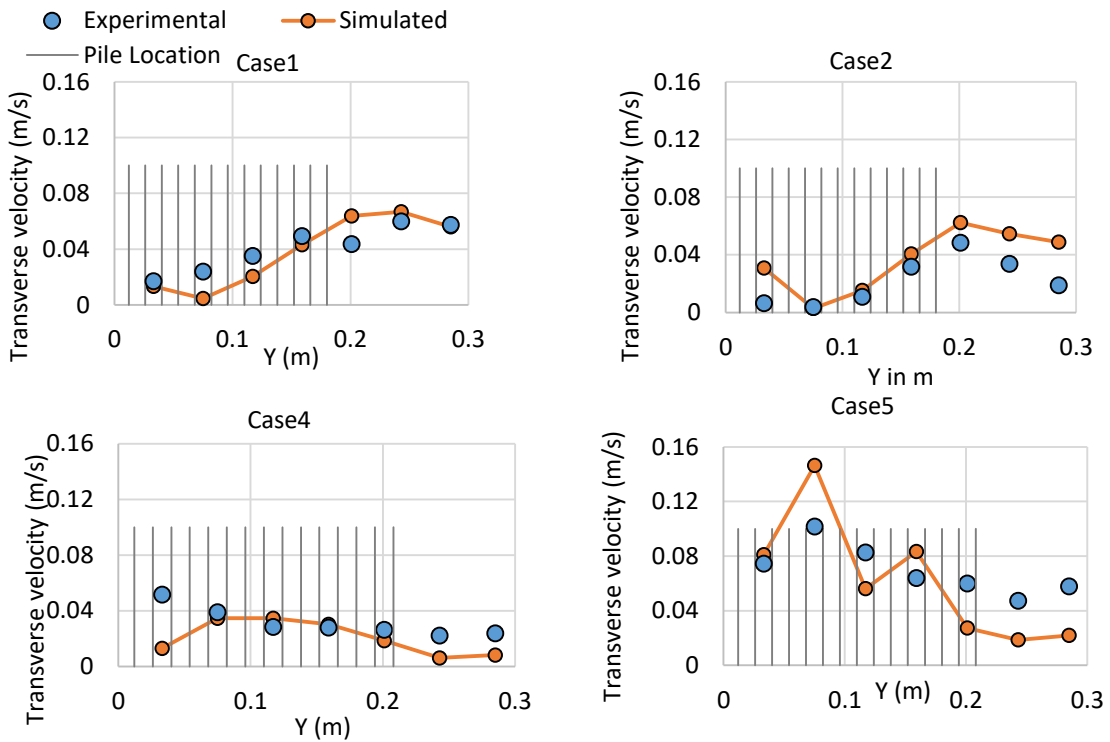


Fig.3.15 Comparison of experimental and simulated surface velocity in case 1

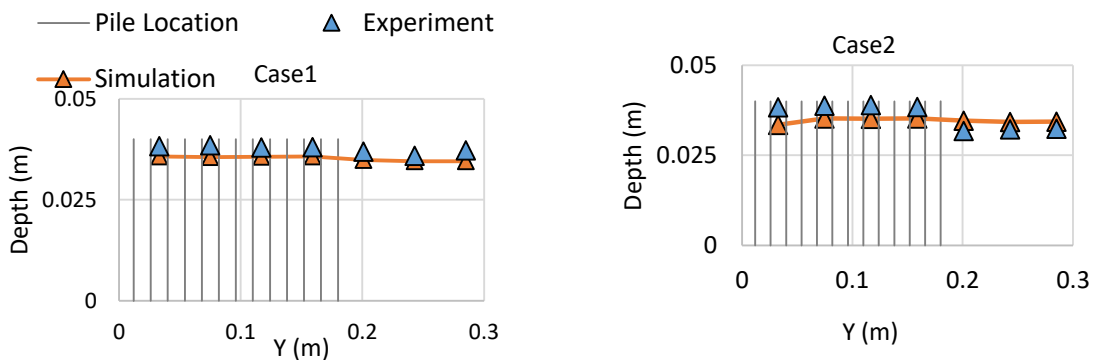


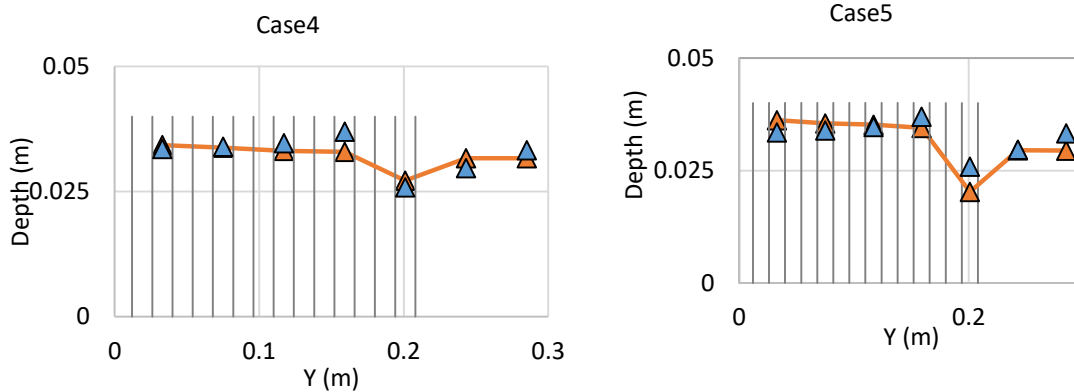


(a) Longitudinal velocity magnitude ($= \sqrt{\bar{u}^2 + \bar{w}^2}$) at $x=0.114$ m, $z=0.02$ m



(b) Transverse velocity magnitude ($= \sqrt{\bar{v}^2 + \bar{w}^2}$) at 0.02m upstream of third spur dike, $z=0.02$ m





(c) Flow depth at 0.02m upstream along the third spur dike from upstream

Fig.3.16 Comparison of experimental and simulated three-dimensional velocity and water depth

3.3.7 Results and Discussions

a) Longitudinal and Transverse velocity

Fig.3.17 and Fig.3.18 showed the comparison between the experimental and simulated velocity. These figures shows good agreement with experimental and simulated velocity. As from the experiment along the tip of spur high vertical velocity component was observed. Fig.3.19 shows the an example of vortical system present in the spur dike zone which confirms that near the spur dike region different types of vortex were formed. The near bottom recirculation was mainly due to the overlapped Horseshoe vortex (HV) while the upper one was due to Detached shear layer (DSL). Though the magnitude of this type of recirculation is very lower compared to the impermeable spur dikes (e.g. Safarzadeh et al. (2016)).

b) Spatial Velocity

Fig.3.20 shows the distribution of calculated dimensionless spatial velocity $(\frac{\bar{u}}{U}, \frac{\bar{v}}{U})$ at different flow depth such as surface, 0.02m and 0.01m respectively. This figure reveals that the magnitude dimensionless of spatial velocity $(\frac{\bar{u}}{U})$ vector varies from -0.05 to 2.2 within the considered zone of the flume. The maximum magnitude of spatial velocity was

found at 0.02m flow depth. The average magnitude of dimensionless spatial velocity within the

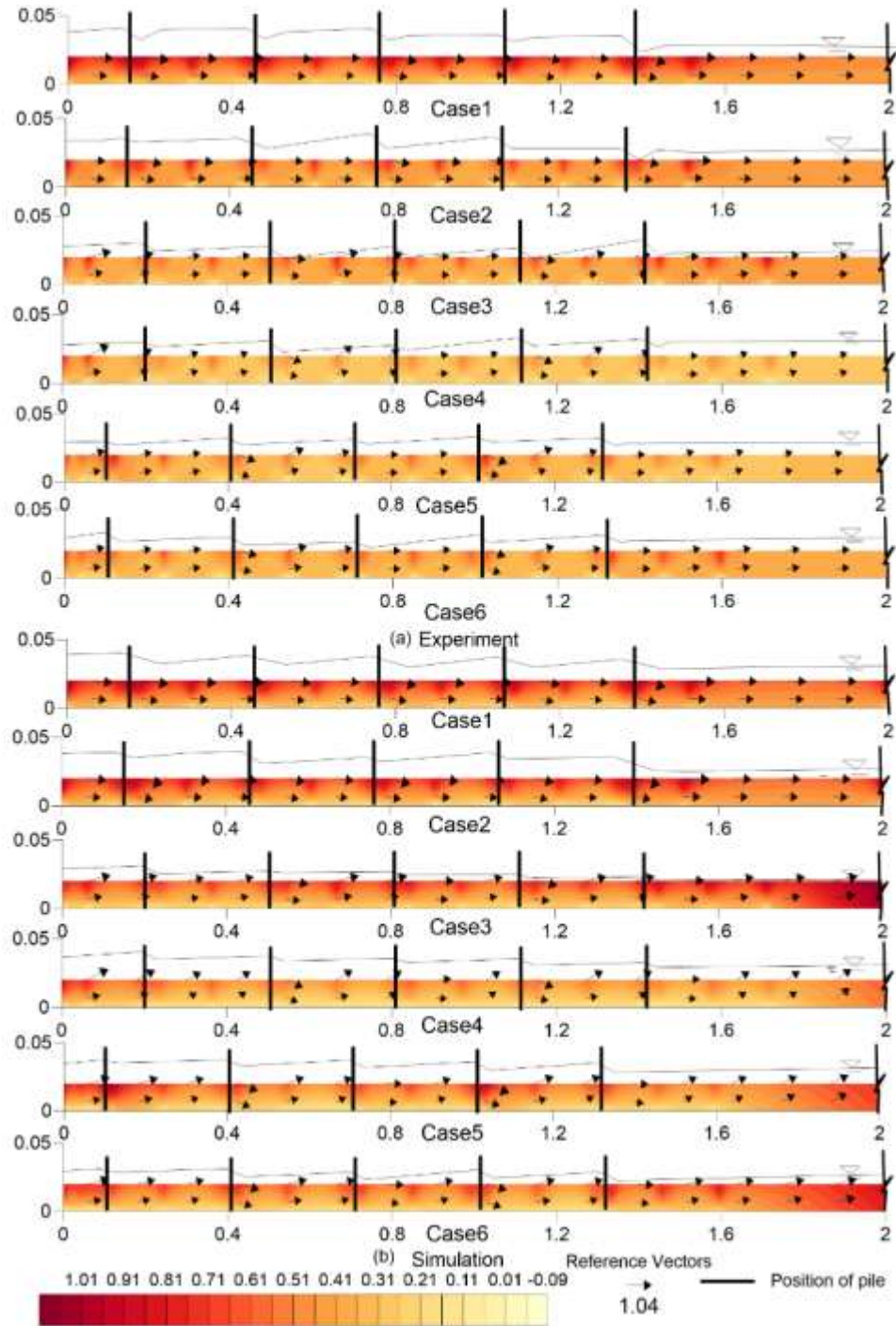


Fig.3.17 Dimensionless longitudinal velocity vector, $(\frac{\bar{u}}{U}, \frac{\bar{w}}{U})$ 0.11m away from the right bank. The contour shows the magnitude of longitudinal velocity component $(\frac{\bar{u}}{U})$

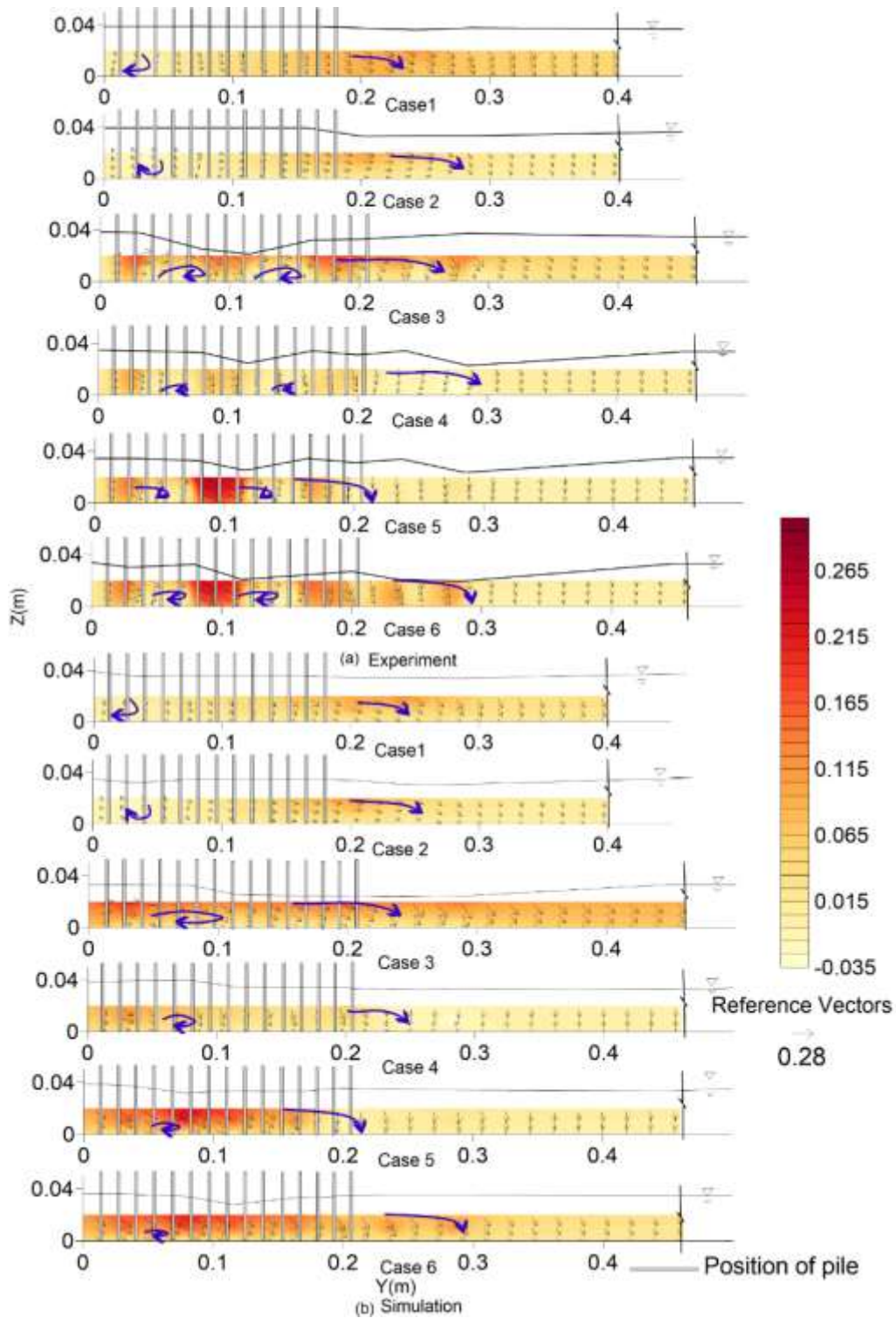


Fig.3.18 Dimensionless transverse velocity vector $(\frac{\bar{v}}{U}, \frac{\bar{w}}{U})$ at 0.02m upstream of third spur dike form the upstream. The contour shows the magnitude of transverse velocity component $(\frac{\bar{v}}{U})$

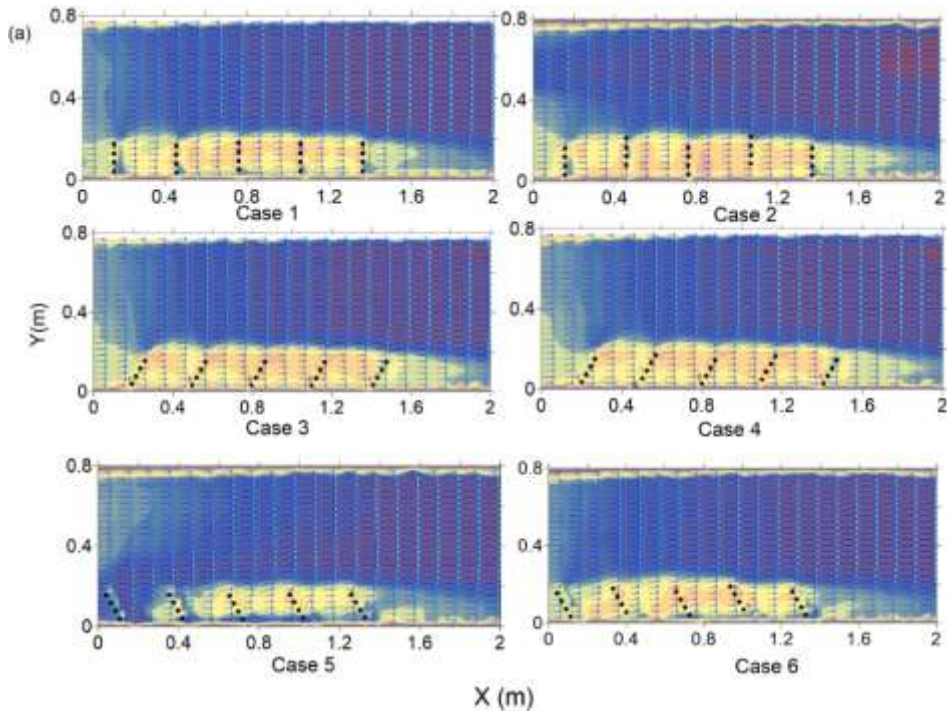


Fig.3.19 Visualization of the vortical structure of the mean flow using Q criterion of case 2.

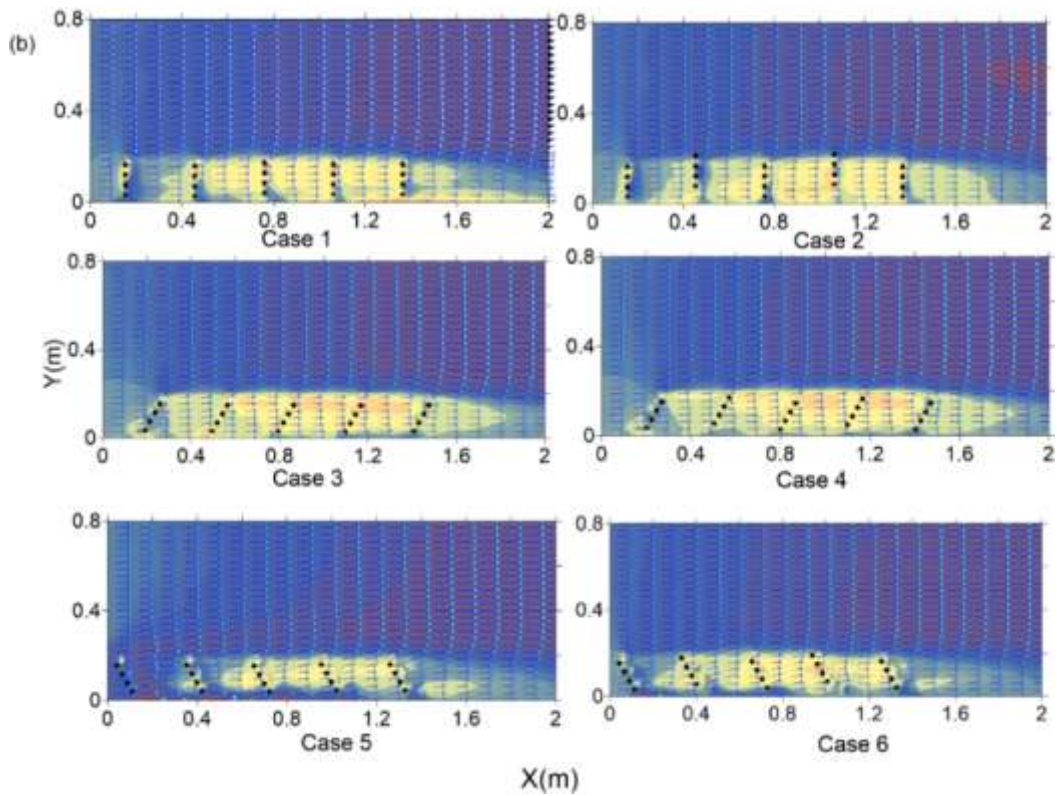
main channel was 1.10 while near the spur dike zone area the velocity was 0.77. Inside the main channel the maximum velocity was obtained in case 2 (1.51) and minimum in case 4 (0.82) at $Z=0.02\text{m}$. Inside the spur dike zone the spatial velocity was almost 6.5% lower in staggered type of installation. Table 3.7 shows the velocity increment (in percentage) in the main channel due to the installation of different types of spur dikes. It is obvious from the figure that the average spatial velocity in the main channel was higher in staggered type of installation. The reason behind that as the tip of the spur dike in staggered case, the second and third spur were was 0.05 m protruded than the squared type installation. Therefore, they acted as one system and deflected more flow towards the main channel.

Table 3.7 Spatial velocity increment in main channel due to the spur dike

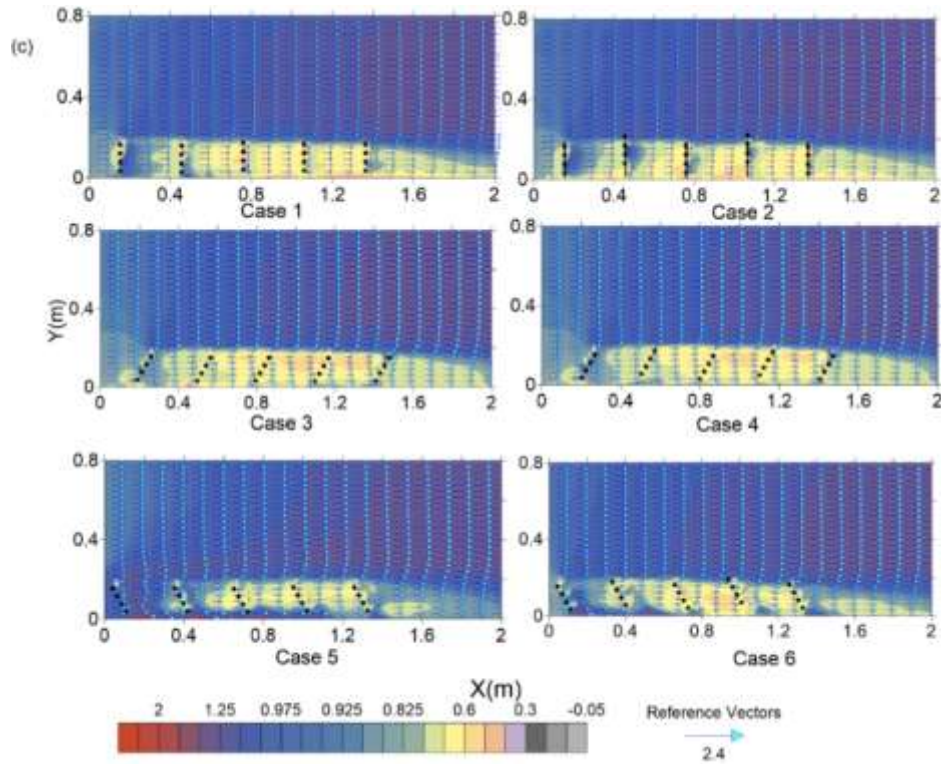
Unit	Case 1	Case 2	Case 3	Case 4	Case 5	Case 6
Percentage (%)	27.60	32.83	33.71	34.48	24.69	29.97



(a) Dimensionless spatial velocity $(\frac{\bar{u}}{U}, \frac{\bar{v}}{U})$ at surface



(b) Dimensionless spatial velocity $(\frac{\bar{u}}{U}, \frac{\bar{v}}{U})$ at $Z=0.02m$



(c) Dimensionless spatial velocity $(\frac{\bar{u}}{U}, \frac{\bar{v}}{U})$ at $Z=0.01m$

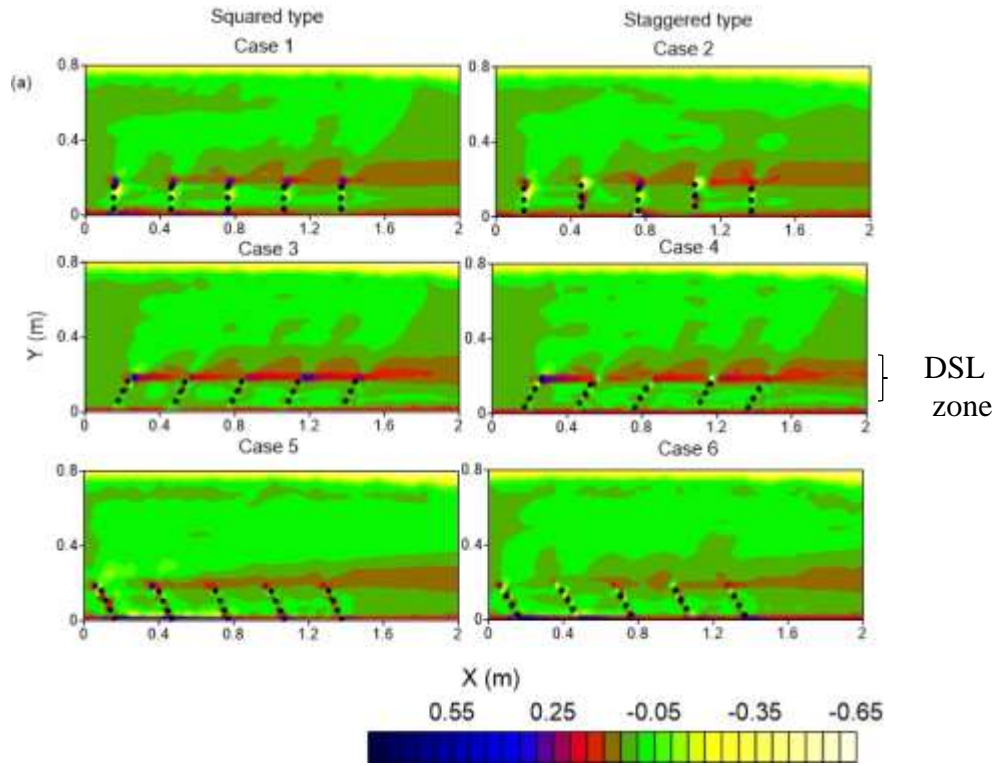
Fig.3.20 Distribution of Dimensionless spatial velocity $(\frac{\bar{u}}{U}, \frac{\bar{v}}{U})$ at different depths. The contour shows the magnitude of longitudinal velocity component $(\frac{\bar{u}}{U})$

c) Reynolds Stresses: Consideration for Sediment Transport

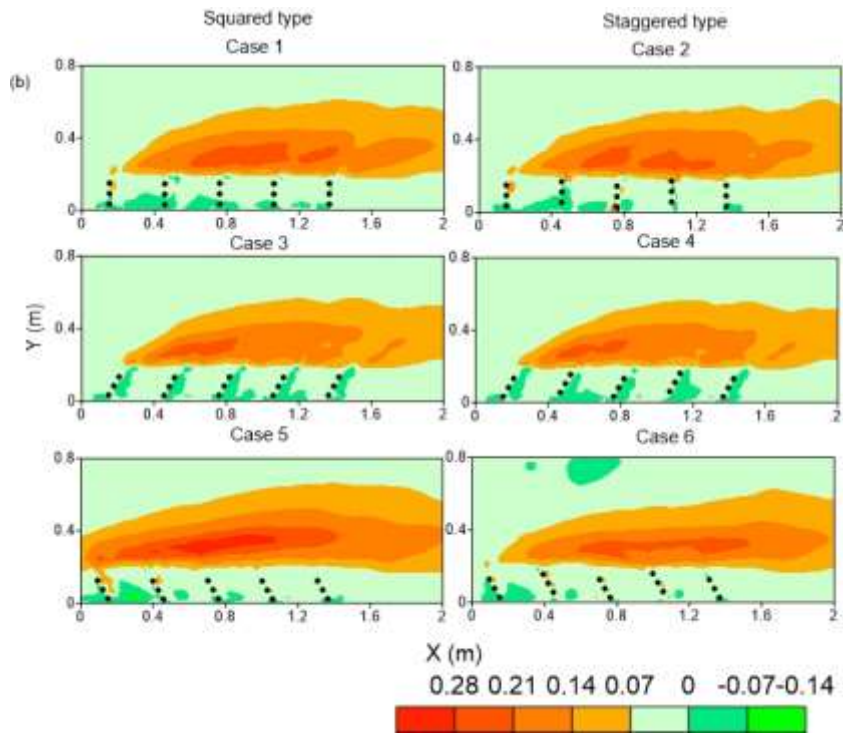
In general, the alluvial river are composed of mix sediment, hence the sorting of sediment near the scour hole is a common phenomenon. Being the part of suspended load, fine sand, silt and clay usually transport by a water column and settle down in weaker turbulence intensified area. The bed material transport rate acts as a function of bed shear stress (Van Rijn 1984). Previous researchers (Duan 2009; Gu et al. 2011; Nakagawa and Nezu 1977) showed that the area where the sediment entrainment rate is high belongs in the positive Reynolds stress area. As this research was done in fixed bed condition; for getting an indication on sediment transport the Reynolds Stresses were discussed in the next paragraphs.

Fig.3.21 shows the distribution of near bed ($Z=0.01m$) dimensionless Reynold's shear stresses. Fig.3.21 (a) shows the distribution of $\frac{-\rho\overline{uv}}{\rho U_*^2}$. This figure indicates intense shear stress happened in the region of detached shear layer (DSL) zone found in transverse velocity. The $\frac{-\rho\overline{uv}}{\rho U_*^2}$ stress varies from -1.63 to 1.29. For case 1 the highest Reynolds stress (0.72) was found around the tip of the first spur dike while in case 2 the Reynolds share stress was lower (0.31) in that region but the highest stress (0.45) was found at the tip of the third one. In case 3 and case 4 the maximum $\frac{-\rho\overline{uv}}{\rho U_*^2}$ (0.91) was found at the tip of the first spur dike. Although in case 3 at the tip of the other spur high shear stress was found which varies from 0.31 to 0.67 but in case 4 the magnitude of stress at the same location was lower (0.21 to 0.28). For case 5 and case 6 at the tip of the first spur the $\frac{-\rho\overline{uv}}{\rho U_*^2}$ value was 0.71 and 0.54 respectively. However, in deflecting cases high shear stress was also found at the attachment area of first spur and right bank.

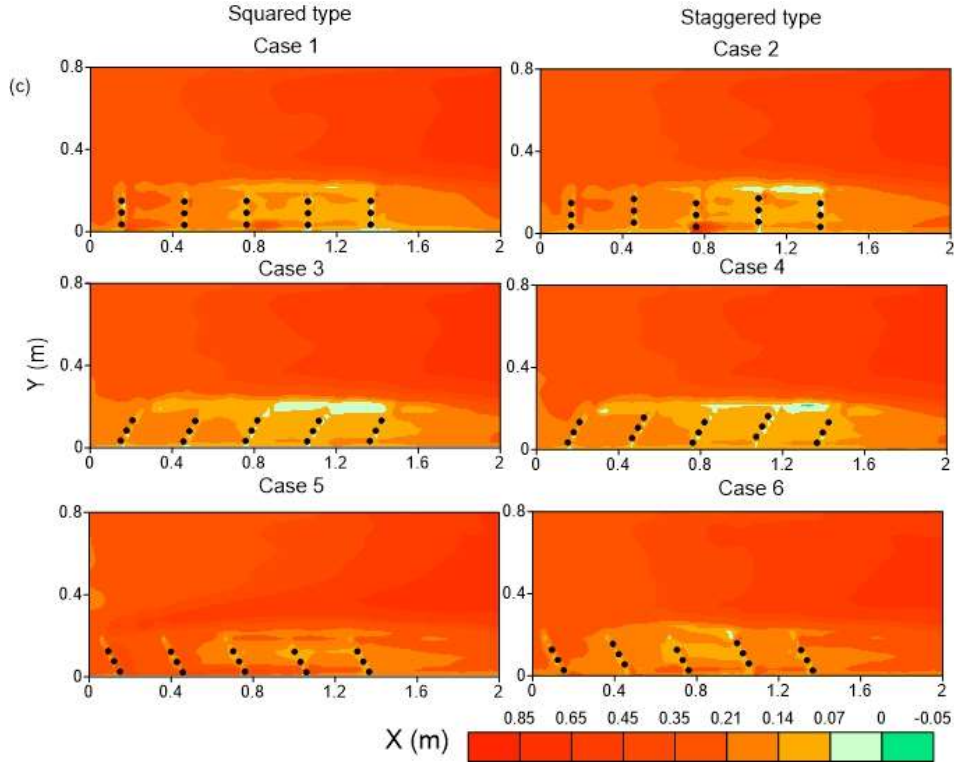
The other two Reynold's shear stress $\frac{-\rho\overline{vw}}{\rho U_*^2}$ and $\frac{-\rho\overline{wx}}{\rho U_*^2}$ are plotted in Fig.3.21 (b) and (c). Through the laboratory measurement, Duan et al. (2009) showed that turbulent burst event contributed to the $\frac{-\rho\overline{vw}}{\rho U_*^2}$ and $\frac{-\rho\overline{wx}}{\rho U_*^2}$ while the positive value implies sweep or ejection event and negative values are associated with inward or outward interaction. The values of $\frac{-\rho\overline{vw}}{\rho U_*^2}$ and $\frac{-\rho\overline{wx}}{\rho U_*^2}$ were positive in the primary flow region which implies sediment is being entrained from this areas. The value of $\frac{-\rho\overline{vw}}{\rho U_*^2}$ ranges from -0.14 to 0.31. Besides the main channel in perpendicular and deflecting cases near the tip of the first and second groin it shows positive value which implies scouring in these region. However, the maximum positive value is found in case 5 (0.31). The area of maximum positive value differs from staggered type and squared installation. $\frac{-\rho\overline{wx}}{\rho U_*^2}$ Shows positive value almost in all region and the value varies from -0.05 to 0.85; having maximum at the main channel (case 5, value 0.75). The distribution of maximum value of $\frac{-\rho\overline{wx}}{\rho U_*^2}$ at spur tip between squared type and staggered type are quite similar as of $\frac{-\rho\overline{vw}}{\rho U_*^2}$.



(a) Contours of normalized Reynolds longitudinal shear stress, $\frac{-\rho \overline{u'v'}}{\rho U_*^2}$



(b) Contours of normalized Reynolds transversal shear stress, $\frac{-\rho \overline{v'w'}}{\rho U_*^2}$



(c) Contours of normalized Reynolds vertical shear stress $\frac{-\rho\overline{w'x'}}{\rho U_*^2}$ at $Z=0.01m$

Fig.3.21 Contours of normalized Reynolds shear stress at $Z=0.01m$

d) Bed Shear Stress

Here, the bed shear stress was calculated from Reynolds stress tensor near the bed. The longitudinal component was calculated by using $\tau_b^x = -(\rho\overline{w'u'} + \rho\overline{v'u'})_{bed}$ (u', v', w' are fluctuation in velocity in the longitudinal, transverse and vertical direction) and the transverse component was calculated by using $\tau_b^y = -(\rho\overline{w'v'} + \rho\overline{u'v'})_{bed}$ and the bed shear stress, $\tau_b = \sqrt{((\tau_b^x)^2 + (\tau_b^y)^2)}$ and the distribution of which The distribution of dimensionless bed shear stress was shown in Fig.3.22. Within the entire zone the dimensionless bed shear varies, from 0.02 to 2.2. For case 1 the tip of the first two spur dikes show the maximum bed shear 1.17 (at $X=0.16 m, Y=0.154 m$) and 1.37 ($X=0.46 m, Y=0.54 m$) respectively. For case 2 at the same location, the bed shear stresses were 0.95 and 0.82 respectively. However, in case 2 the maximum share stress was 1.06 found in near the attachment area of the bank and third spur dike (at $X=0.76 m, Y= 0.03 m$). In case 3

the maximum dimensionless bed shear stress (1.56) was found at $X=0.26$ m, $Y=0.18$ m, at the tip of the first spur dike. In case 4 the location of the maximum shear was same as case 3 but the value was 7% higher. In case 5 an intense shear stress zone was observed near the first spur dike where the maximum value reaches up to 2.09. Similar type of shear stress pattern was also observed in case 6 but the maximum value was 1.57; almost 24% lower than case 5.

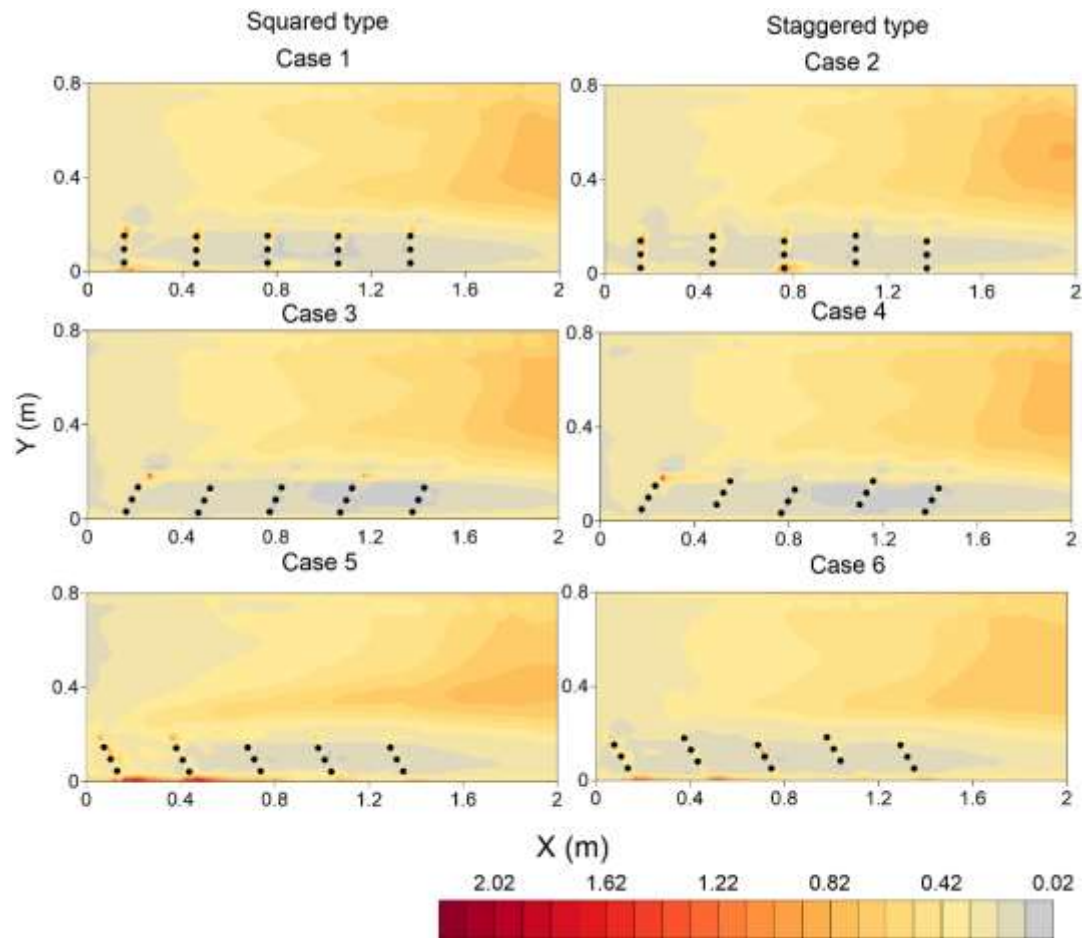


Fig.3.22 Dimensionless bed shear stress calculated from Reynolds stress

3.4 Non-structural measures of bank protection for braided network

3.4.1. Managing the bifurcation to control bank attached channels

In management strategies of braided river geomorphological properties of bank attached channel of the braided river (by mining of gravel or sand or other means) is considered as a common practice in the expansion phase of the braided river (Piégay et al. 2006). The discussion of section 1.5 of this thesis clearly explained that the river Brahmaputra-Jamuna has a tendency of widening through bank erosion in the recent age. Hence by controlling the hydraulic property of the bank attached channel by managing the bifurcation can be an option to protect the river bank. In this section, a natural bifurcation of Brahmaputra-Jamuna firstly analyzed numerically which switch into one channel naturally. Using the bathymetry and hydraulic condition of that channel prior to switching, several synthetic options have been tested to check the critical condition of bifurcation switching.

Bifurcation is one of the major “building block” element of braided river network (Mosley 1976). Being generated by mid-channel bar, bifurcation regulates the flow and sediment transport to the downstream branches and thus play a major role in the morphology of the braided network (Ferguson 1993; Sambrook et al. 2009; Schuurman and Kleinhans 2015). Bifurcation plays a significant role in the development process of these compound bars too. Merging with other bars, dissection of the bar through crossbar channels during the high stage, loosing of connection or local narrowing of adjacent branch channels causes non-uniformity in the growth of these type of bars and these processes are strongly related with the dynamics of bifurcation (Schuurman et al. 2013). Switching of bifurcation is a key process in the development stage of these type of bar as this process allows the bar to be merged with other bars.

Previous studies (Bertoldi and Tubino 2007; Bolla Pittaluga et al. 2003b; Federici and Seminara 2003; Kleinhans et al. 2006; Wang et al. 1995) showed the process of bifurcation but most of them are based on the nodal point concept rather than the network formation process of the braided river (Schuurman and Kleinhans 2015). In spite of the greater simplifications of the real process, these models can predict the major aspects of

bifurcation dynamics (Bolla Pittaluga et al. 2003b). Through the laboratory experiment of Bertoldi and Tubino (2007) gave direct validation of the model of Pittaluga et al. (2003b). Most of the work is focused to characterize the symmetrical bifurcation with steady flow condition. But in nature, most of the bifurcation are asymmetrical and experience unsteady flow (Ashmore 1991). Based on field observation, lab experiment and numerical simulation it was explained that either the planform of the bifurcation or the hydraulic property of upstream channel plays the major role in case of closing one channel (Kleinhans et al., 2006; Federici and Paola, 2003). Here, focuses were made to know what controls the switching phenomenon of bifurcation in a small branch of Brahmaputra-Jamuna River showing Fig.3.23 was flowing along the left side of a cluster of bars but in 2013 the right-sided channel became larger (Fig.3.23 b and c). This phenomenon was reproduced by varying the upstream discharge or downstream water level using unsteady flow condition through numerical simulation. The main objective of this section is to find out what accelerate the switching phenomenon, upstream control or downstream one in unsteady flow condition. Several cases were considered for this purposes which have been described in the next sections. Then attempt had been made to investigate the relationship of the upstream channel and downstream mid-channel bar geometry with the switching phenomenon. The effect of bifurcation angle on the switching process has also been studied through this section.

3.4.2. Two dimensional Morphodynamic model of bifurcation

Fig.3.23 showed a 17 km long braided-loop of Brahmaputra-Jamuna river that experienced switching process of bifurcation from 2011 to 2013. The dry season satellite image showed that in 2011 a relatively larger channel (channel A compared to channel B) The same numerical model used in chapter 2 for calculating bed evolution was used in this section and applied to the 17 km long river reach (Fig.3.23 d). The considered cases are showing in and Fig.3.24. The total simulation period was 137days which reflects only the peak stage of the river. Four cases were considered including the base condition. Base condition was fixed on basis of the hydraulic condition of the year 2011. Then in Case 1 the discharge was increased 1.5 times of the base condition which was identical of the real river discharge of the year 2013 but keeping the downstream water level at the same as of the year 2011. In case 2 discharge was kept same as of the base condition but decreasing the water level 0.90 times of base condition to match with the water level of the river of 2013. The boundary condition of case 3 was almost similar to the hydraulic condition of the river during the year of 2013.

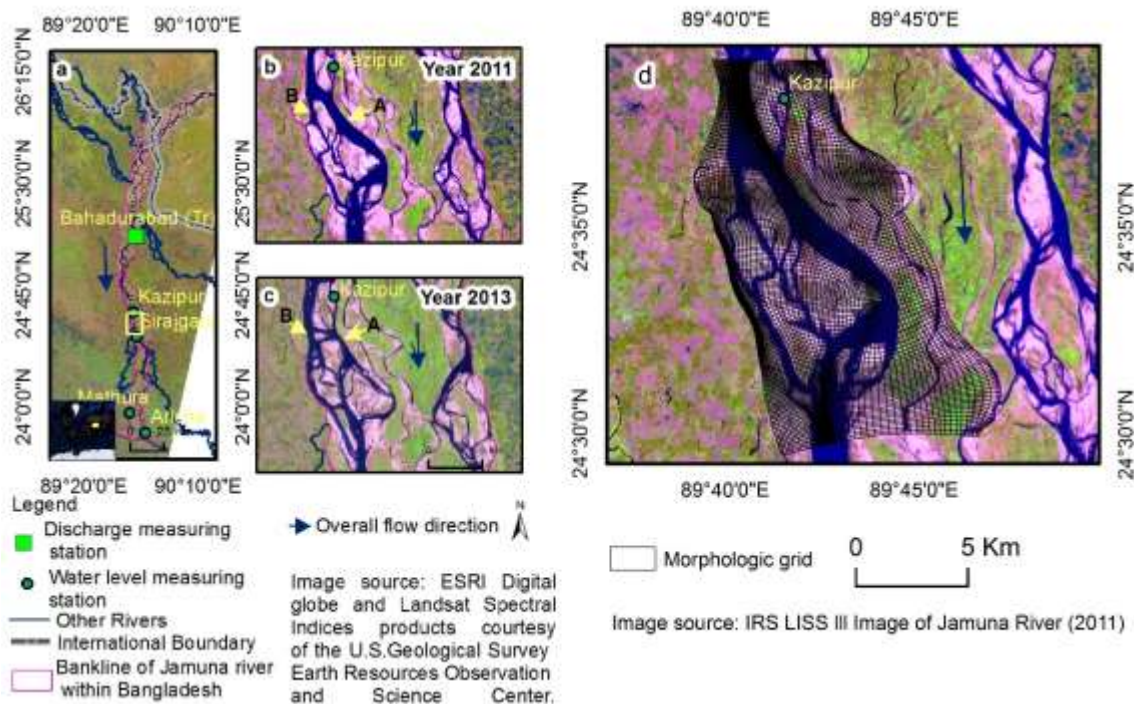


Fig.3.23 (a) Map showing the study area; (b) and (c) changes of the study area over time (d) Model domain of the numerical simulation

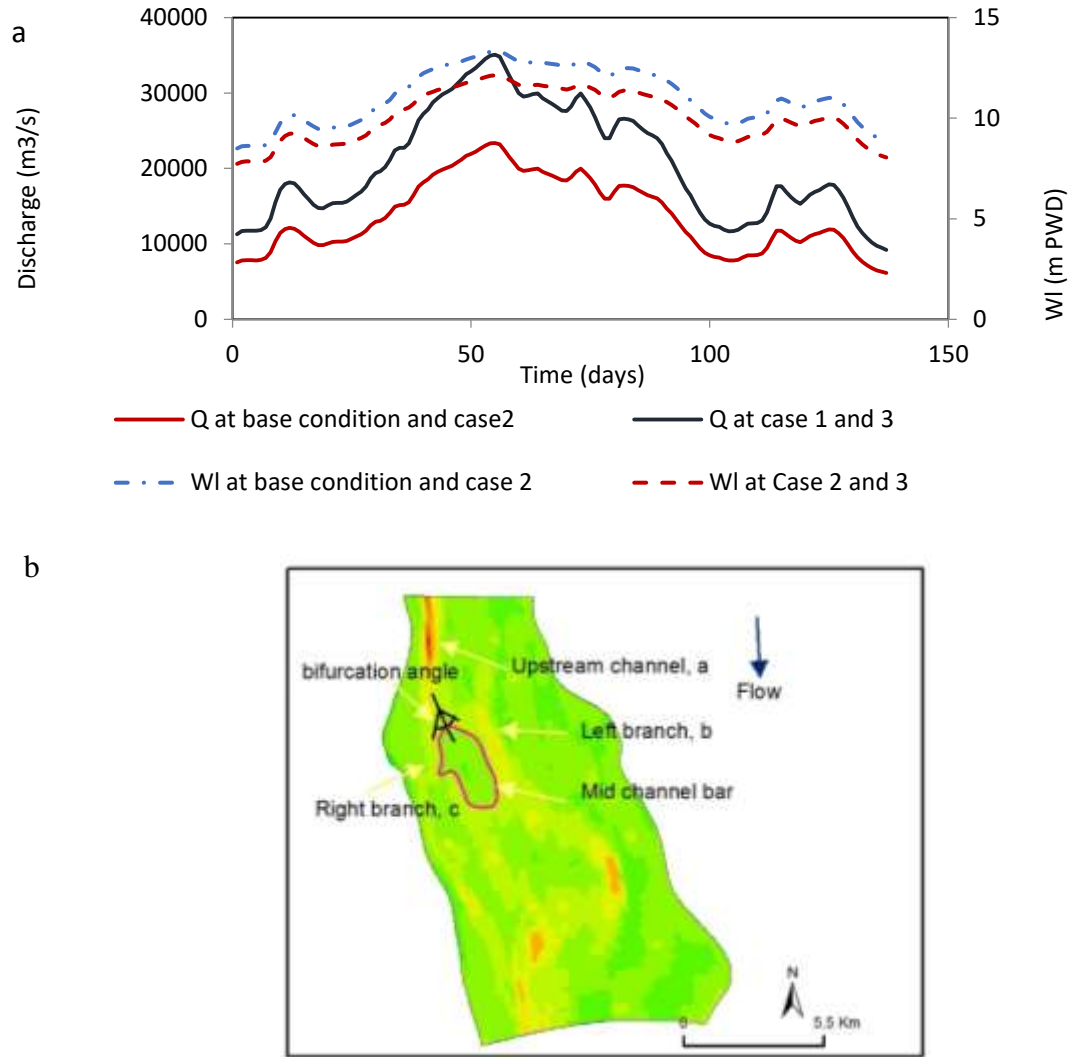


Fig.3.24 (a) Boundary Condition of the considered cases (b) Definition and terminology used in model result analysis

In case of braided river during high stage, generally the flow covers the full width of the river. In that time it is difficult to define the left and right branches. The active channel area was considered where the sediment transport was higher (more than 25%) than the average channel sediment transport as branches during peak flow. In case of defining the other parameter, we followed the definitions of previous research's (Pittaluga et al., 2003; Bertoldi and Tubino, 2007). So, the upstream channel aspect ratio β_a , Shields stress v_a is defined by equation 3.43 and 3.44 respectively

$$\beta_a = \frac{W_a}{2D_a} \quad (3.43)$$

$$v_a = \frac{\tau_a}{(\rho_s - \rho_f)gD_s} \quad (3.44)$$

Where, W_a is the upstream channel width, D_a is the upstream channel depth τ_a is the average bed shear stress (Fig.3.24 b shows the location of channels and other definition). Bar aspect ratio, α_b is defined by the bar length to width ratio. The discharge ratio, r_q is the ratio of discharge of branch b to branch c.

3.4.3. Results and Discussions

a) Switching of channel

The changes of discharge ratio, r_q between the branch b to c are shown in Fig.3.25a. This figure indicates that in case of base condition and case 2 no bifurcation switch were happened but during case 1 and case 3 switching was happened. The minimum value of r_q was 0.64 which was happened in case 3 and the maximum value was 1.79 in case of case 1. As response of unsteady flow during the peak time the discharge ratio decrease in all cases but with the decrease of total discharge this ratio increases.

Fig.3.23 (b) shows the final bed elevation of different cases. This figure indicates that in case of case 1 and 3 the changes of planform is higher (more channels were visible) compared to case 2 and base condition. Though the channel width of branch c (right branch) was not vary (average width was 362.83 m) largely but during the case 1 and case 3 the channel deepening was happened. The lowest elevation happened in case of case 3 and the value was -1.19 m PWD; about 1.25 times lower than the initial value of 3.86 m PWD.

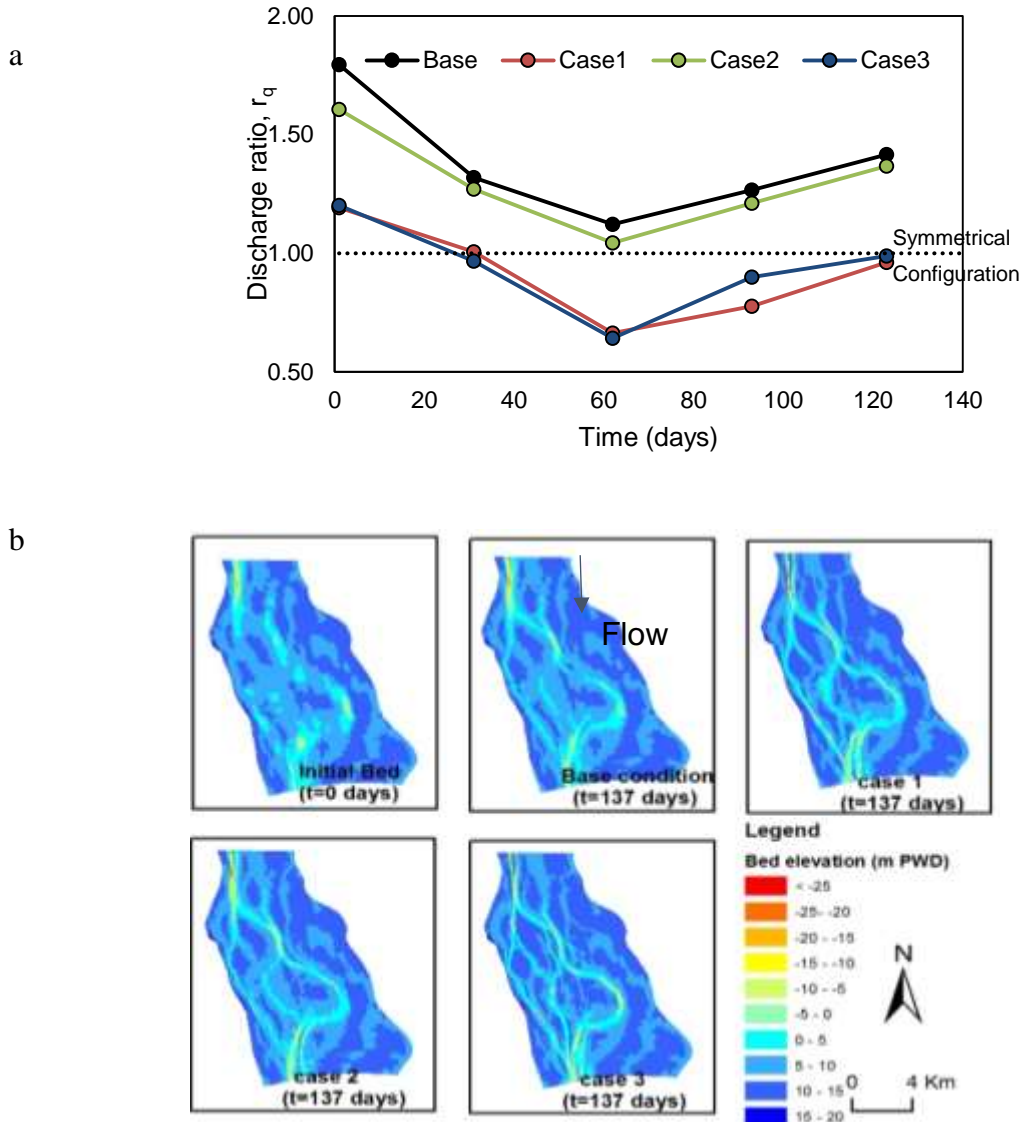


Fig.3.25 (a) Changes of discharge ratio, r_q over time (b) Final bed elevation of the considered cases

b) Relation between bifurcation switch and upstream channel geometry and hydraulic condition

The relationship between the upstream channel geometry change and the bifurcation switching phenomenon is shown in Fig.3.26, Fig.3.27 and Fig.3.28. During the all cases the upstream channel aspect ratio changes from 27.54 to 50.54. The switching occurred relatively small value of aspect ratio (here was 27.56). This figure also indicate that once switching was happened, the r_q tends to be stable even with high aspect ratio.

Bed share stress is an indicator of to predict the morphological evolution of the channel. Fig.3.27 shows the bed share stress at the day of peak flow and this figure indicated that during case 1 and 3 bed share stress is higher in right branch (the value was 7.34N/m^2 and 10.11 N/m^2 in case 1 and 3 respectively). The relationship between shield stress and discharge ratio is shown in Fig.3.28. For this particular case the value of shields stress varies from 0.07 to 0.63 with an average value of 0.22. It indicates higher the asymmetry in the discharge ratio, the value of shields stress becomes lower. This figure clearly shows the distinction between switching and non-switching bifurcations. It shows switching was happened only when the shield stress in the upstream channel higher than 0.2.

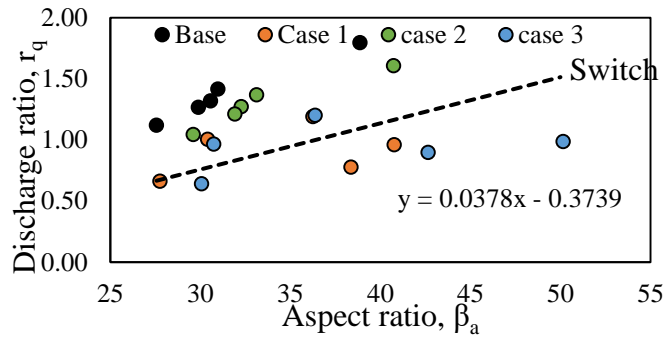


Fig.3.26 Changes of Discharge ratio, r_q with upstream channel aspect ratio, β_a

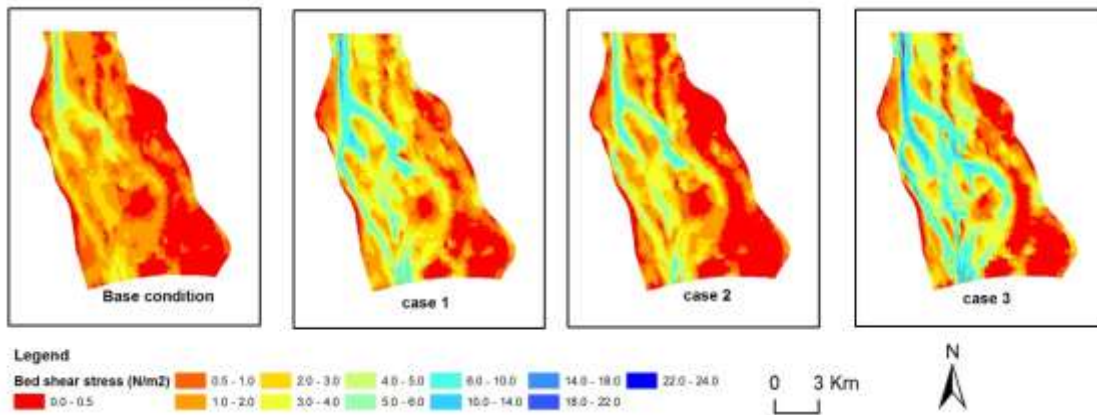


Fig.3.27 Bed share stress of the considered cases at of peak flow

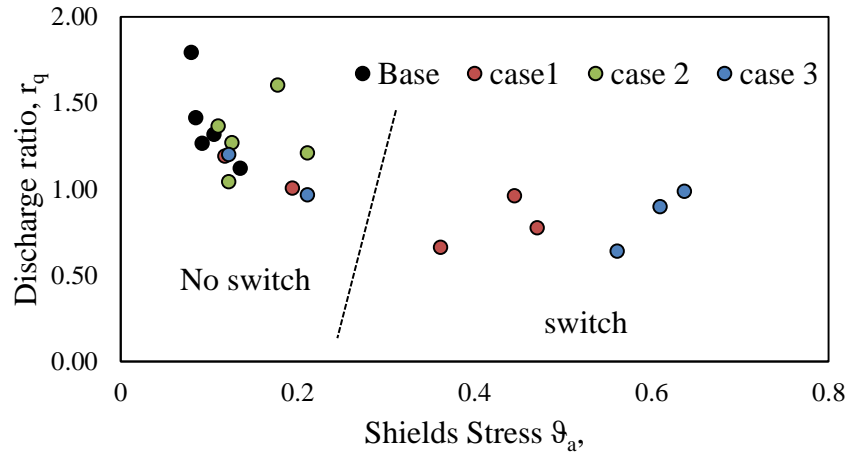


Fig.3.28 Change of discharge ratio with the change of upstream channel shield stress

c) Bifurcation switch and downstream mid channel bar

The relationship between r_q and angle of bifurcation was estimated from the model results. This relationship is shown in Fig.3.29(a). This figure indicates no specific relationship exists between these parameters. Fig.3.29(b) describes the relationship between r_q and the aspect ratio of downstream mid-channel bar. The aspect ratio of bar varies from 1.3 to 3.5 with an average value of 2.4. Though with the increment of aspect ratio of downstream mid-channel bar, the r_q tends to decrease but it did not show any particular trend with the switching phenomenon.

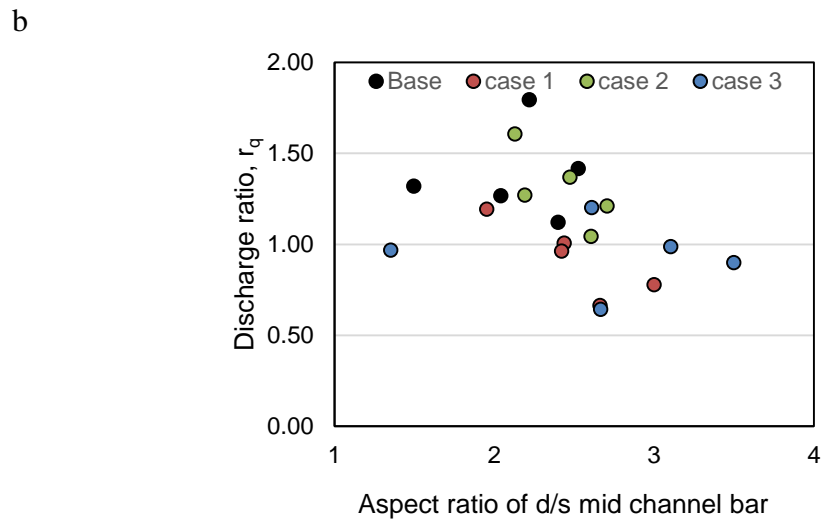
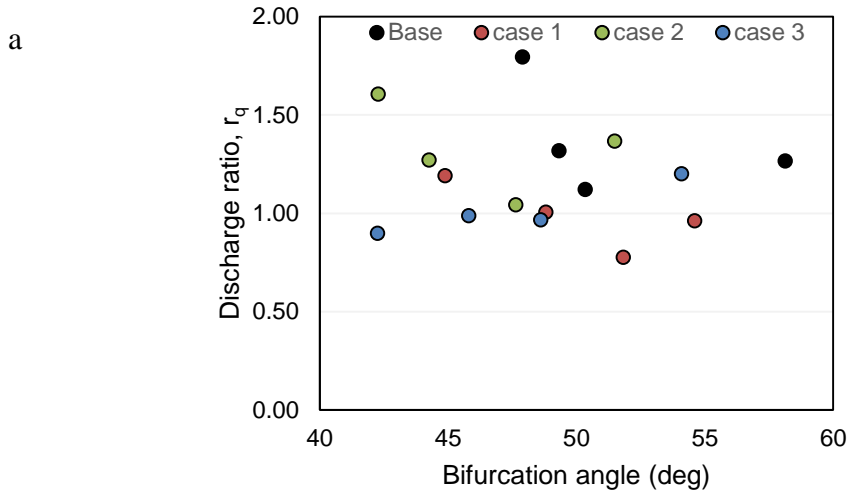


Fig.3.29 Relationship between (a) r_q and angle of bifurcation (b) r_q and aspect ratio of mid channel bar

Here, the numerical simulation was done only for one peak period. Morphological update has been accelerated by applying Morphological acceleration factor. But in reality such change may take several years to happen or even it can be happened quicker than that of the simulation. In this research four cases were considered. Assuming one as the base condition the upstream and downstream boundaries have been changed to assess the response of process.

The first observation is normally the configuration of bifurcation was asymmetrical in all cases. Upstream control play the major role in switching phenomenon of the channel as the switch happened only in case 1 and 3 when discharge were higher.

In the lab experiment, Bertoldi and Tubino (2007) found higher the aspect ratio of upstream channel, higher the asymmetry. But in this study we found this statement is true upto a threshold near the symmetrical configuration; after that switching happened. The unbalance is higher in very low shields stress which is also similar by the lab experiment of Federici and Paola (2003); Bertoldi and Tubino (2007) but after switching; the discharge ratio became stable even if the shields increased further in the upstream channel. No specific relationship with the bifurcation angle and switching phenomenon or discharge asymmetry was fund. But Fedrerici and Simenara (2003) and Van der Mark and Moselman (2013) indicated that there may be an acceptable relationship between these two. Downstream mid channel bar aspect ratio were not directly related to the switching phenomenon but there exist a correlation with the upstream channel aspect ratio and downstream channel mid channel bar (Fig.3.30).

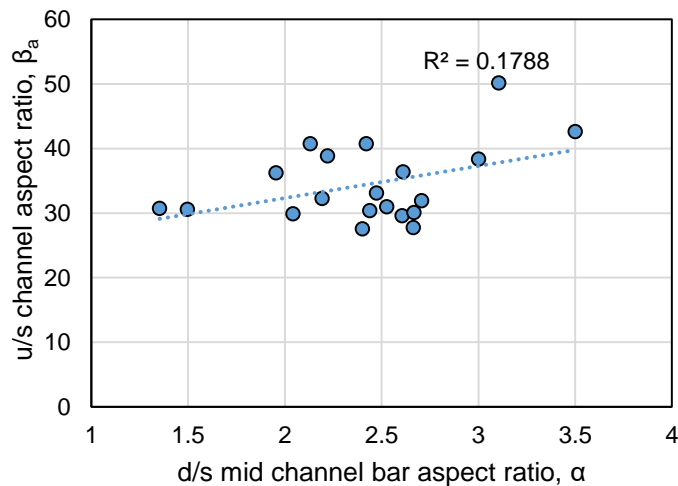


Fig.3.30 The relation between u/s channel aspect ratio to d/s mid-channel bar aspect ratio

3.5 Summary

This chapter discuss about the probable bank protection measures for the Brahmaputra-Jamuna River. Firstly the performance of previously built countermeasures were discussed. Then the performance of the proposed structure of this research “slit type spur dike field” was elaborated by laboratory experiment. Numerical model was developed to reproduce the laboratory results. Lastly, through the numerical simulation switching phenomenon of braided channel was examined which can be used to manage the braided channels. The results of the analyses can be summarized as follows:

The performance of the previously built protruding type of structure in the Brahmaputra-Jamuna River indicated that the structures generally failed due to the local modification of flow by producing high bed shear stress. Hence, low bed shear stress producing “slit type spur dike field” is suggested in this study. Through the laboratory experiments and numerical simulation, this study investigated the flow structure around slit type permeable spur dike field including several layout alternatives for practical use. Using 3D RANS coupled with $k-\omega$ SST turbulence closures and the VOF method for capturing the free water surface; the hydrodynamic model showed good agreement with the experimental results in reproducing the flow structure around very permeable pile spur dike field. This study revealed that using slit type permeable spur dike as a field, the approach velocity of flow can be reduced into a considerable amount within the spur dike zone. Attractive type of spur dike seems to be a better choice in reducing the longitudinal velocity within the spur dike region. However, deflecting type of spur were more successful in producing transverse flow to the opposite bank. This study also indicated that arranging the pile in a staggered grid within different spur brought better functionality in the spur dike field in terms of reducing the bed shear stress and creating quasi-uniform turbulence zone. However, high bed shear stress at the spur tip, especially for the initial spur, cannot be avoided in this type of spur dike field too. Hence, for field application of this type of structure, better protection measure should be taken for the initial spurs.

Bifurcation switching/ abandonment is a very basic mechanism in the development process of compound bars of the braided river. Through this part of research the bifurcation switching phenomenon using unsteady flow condition and natural river bathymetry was analyzed. In case of bifurcation switching, upstream control (discharge) has more effect

compared to the downstream control (water level). Unbalance in discharge is higher in case of high aspect ratio of upstream channel. At lower shields stress higher asymmetry of discharge distribution is observed. Towards the symmetrical configuration, shields stress is become higher. After the switch discharge ratio become stable with the fluctuation of shields stress. The dimension of the downstream mid-channel bar affect the switching phenomenon by affecting the upstream channel's aspect ratio not directly influencing the discharge distribution.

Chapter 4

Field application of slit type permeable spur dike in Brahmaputra-Jamuna

4.1 Background

This chapter discusses the effectiveness of slit type spur dike in a small bank attached channel of the Brahmaputra-Jamuna River. The slit type spur dike model discussed in chapter 3 has been examined numerically using the real field data. Two cases have been selected one is without the spur the natural flow condition and another is with the spur dike. The best possible model of the spur was chosen from the laboratory experimental results. The same numerical model used in the experimental flume was used here. In the next paragraphs, the location of the study site and model details have been described.

From the 2D model described in chapter 2, a small portion of the river channel was chosen for applying the 3D model. The location of the river reach is shown in Fig.4.1. It is evident from this figure that the river bank during the period of 2011 to 2013 the river reach experienced 457.74 m bank erosion. It is evident from the results of the 2D model that during the flood of 2011, the channel experienced the maximum peak discharge of 27395 m³/s with the maximum flow depth of 5 to 10 m. The calculated bed shear stress and flow direction from the 2D model in this area are shown in Fig.4.2 a. In the bank attached channel, the bed shear stress varies from 3.4 to 8.9 N/m² during the maximum peak discharge of 2011. Using the above mention situation as background the 3D model with two cases were constructed shown in Fig.4.2 (c) and (d).

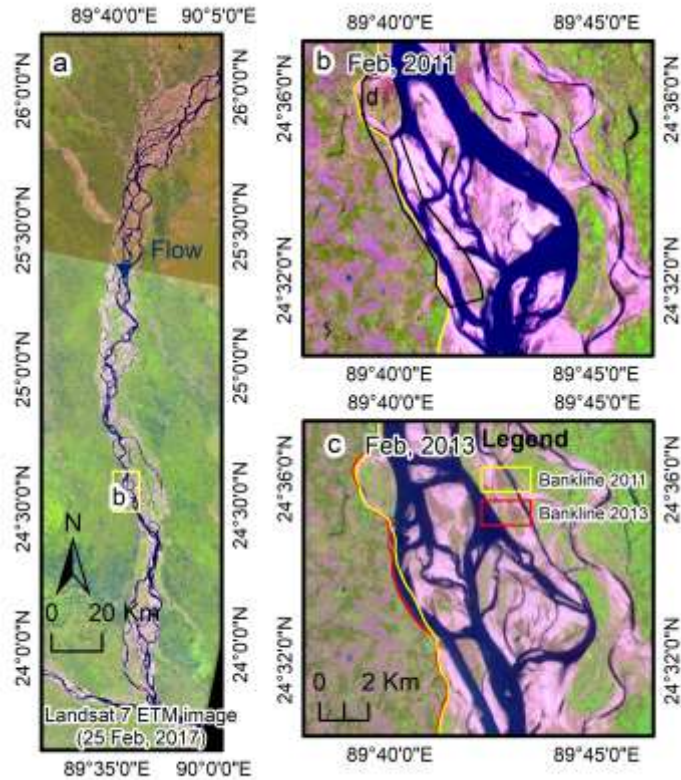


Fig.4.1 Map showing the study area. (a) The Brahmaputra-Jamuna river reach in Bangladesh (b) and (c) planform and bank line changes in the study area during the year 2011 to 2013.

4.2 Model Schematization

The experimental results and numerical simulations described in chapter 3 suggests that the attracting spur with staggered installation produce the lowest bed shear stress among the considered cases. Hence, this arrangement was chosen as the best possible solution. Therefore, the laboratory model has been scale-up according to the river width/depth ration and installed in the numerical model with the bathymetry of Brahmaputra-Jamuna (bathymetry is shown in Fig.4.1 b).

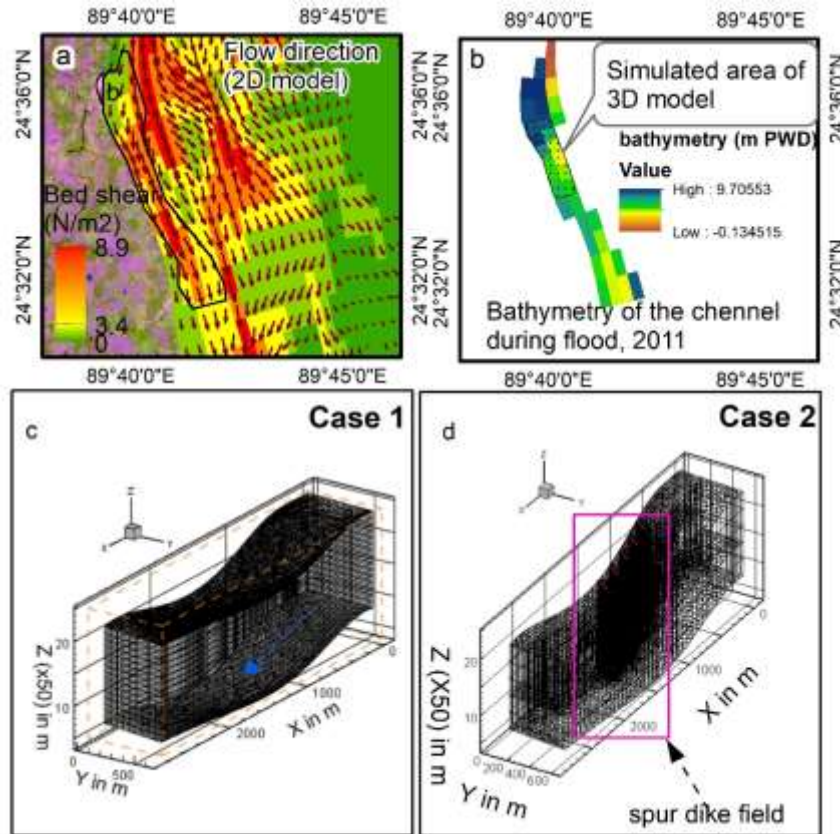


Fig.4.2 The flow direction and bed shear stress calculated from the 2D model (d) the bathymetry of the study channel (e) without structure finite element mesh used for numerical simulation

However, the details of the spurs are shown in Fig.4.3 . Five spurs, aligned 120° with the flow were installed with the permeability of 71% keeping similarity with laboratory experiment (Fig.4.3a). Each spur dike consists of fifteen individual unsubmerged piles. The pile diameter was 2.5 m and the gap between the piles was 6.25 m (Fig.4.3b and c). The spacing between spur was 187.46 m while the length was 113.75 m. from the upstream end the distance of the spur dike field was nearly 900 m and 1300 m apart from the downstream end. For the multiphase 3D simulation five patches were considered as shown in Fig.4.3d – bed, atmosphere, inlet, outlet and wall which includes the spur dike. The generation of 3D finite volume mesh for non-regular surface i.e. river bathymetry is challenging. Hence in this case a combination of prismatic mesh and hexahedra mesh was considered (see Fig.4.3).

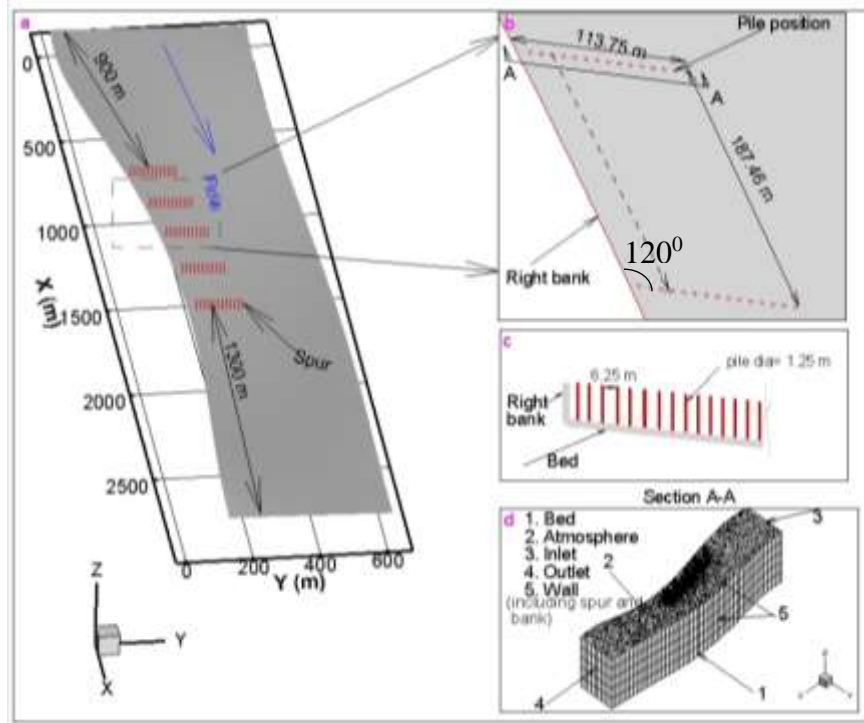


Fig.4.3 The details of the spur dike

The details of the considered meshes were shown in

Table 4.1. The total cell volume used in without spur case varies from 123.99 m³ to 1521.02 m³ while in case of with spur they varied from 0.52 m³ to 9797.61 m³. Such variation was necessary to accurately model the spur dike's pile.

Table 4.1 Mesh details of the considered cases

Characteristics	Case 1 (Without Spur)	Case 2 (With Spur)
Number of mesh	prisms: 56850	hexahedra: 45930 prisms: 12750
Max aspect ratio	31.92	17.17
Face area	Min: 14.55 Max : 1521	Min: 0.17 max:3265.94
Non-orthogonality	Max: 33.88 Avg: 5.9	Max: 52.75 Avg: 4.46
Skewness	Max: 0.55 Min:123.99	Max:4.60 Min:0.52
Cell volume	Max: 1521.02. Total: 2.07e+07.	Max: 9797.61 Total 2.07e+07.

4.3 Boundary conditions

The boundary condition was kept similar to the flood of the year 2011 in that channel which implies the constant discharge of $Q=27395 \text{ m}^3/\text{s}$ at the upstream and zero gradients for the outlet at pressure boundary to confirm uniform flow depth. A detailed description and of the boundary types can be found in Table 4.2. As the boundary condition, at inlet, the flow velocity was calculated using $U_{avg} = \frac{Q}{\alpha_{1,S}}$ (variableHeight-FlowRateInletVelocity function) initially (see Table 1). When the pressure, p is known, U is evaluated from the flux, normal to the patch. The patch pressure is estimated from $p = p_0 - \frac{1}{2}|\mathbf{U}|$ where p_0 was total pressure. No slip condition was applied to the walls as a velocity boundary. Wall function approach was used to link the turbulent flow near the wall like structure i.e. bank and spur. kqRWallFunction, omegaWallFunction, nutUSpaldingWallFunction were applied to the walls as the turbulent boundary conditions. The details description about the boundary function can be found in OpenCFD (2009).

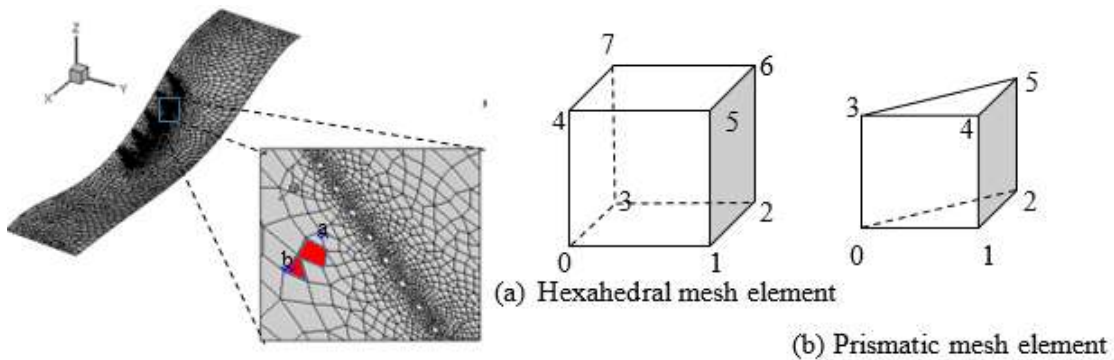


Fig.4.4 Mesh used in the simulation

Table 4.2 Boundary condition of the simulation

Domain Patch	Bed	Atmosphere	Wall (Spur dike)	Outlet	Inlet
Velocity, U	noSlip	pressureInletOutletVelocity	noSlip	pressureInletOutletVelocity	variableHeightFlowRateInletVelocity
Pressure, p	zero gradient	totalPressure	zero gradient	Zero gradient	For $\Omega = 27395$ zero gradient
Turbulent kinetic energy, Specific dissipation rate,	kqRWallFunction on omegaWallFunction	uniform fixed value inletOutlet	kqRWallFunction on omegaWallFunction	internalField Uniform fixed value	Uniform fixed value Uniform fixed value
Turbulent kinematic eddy viscosity, ν_t	nutUSpaldingWallFunction allFunction	Calculated from other patch fields inletOutlet	nutUSpaldingWallFunction allFunction	Calculated from other patch fields inletOutlet	Uniform fixed value Uniform fixed value
Phase fraction, α	zero gradient	inletOutlet	zero gradient	inletOutlet	variableHeightFlowRate

4.4 Results and Discussions

4.4.1 Longitudinal velocity

The magnitude of longitudinal flow velocity component, \bar{u} at near bed (bed level, $z=10$ m), mid-depth ($z=14$ m) and near surface ($z=19$ m) in case 1 (without spur) and case 2 (with spur) are shown in in Fig.4.5. At $z=19$ m The longitudinal flow velocity, \bar{u} ranges from 0.5 m/s to 9.69 m/s. Due to the placement of spur dike the longitudinal velocity reduce from 7.69 m/s to 4.09 m/s. This figure indicates that due to the installation of spur the near bed velocity increased along the tip of the spur dikes. For example, upstream of the third spur dike, near the bank ($X=1389.75$ m, $Y=190.50$ m) the \bar{u} was found 2.71 m/s where at the tip the of the same spur the velocity was 5.68 m/s almost 2.09 times higher. This velocity increment was due to the pressure gradient within the exchange flow zone of spur dike and main channel. Fig.4.6 shows the distribution of pressure gradient around the tip of third spur indicating the variation of pressure gradient from 442 Pa/m along the bank side of the spur where it varies 852 Pa/m at the tip of the spur. The vortex system near the bed also responsible for these increments. Considering all the spurs the magnitude of near bed velocity increase 4.89% at tip compared to the mid-section of the spur dike.

However, at mid-depth ($Z=10$ m) the increment of velocity continues along the tip (the average value was found 6.15 m/s). Near the bed ($z=10$ m) similar patterns were observed. The tip velocity was intensified. For example at the tip of the 3rd spur it was 6.61m/s.

Fig.4.7 shows the distribution of longitudinal velocity (\bar{u}, \bar{w}) along a within arbitrary long section along the Z plane (section center: $X=1426.49$ m, $Y=225$ m) shown in the bottom. This figure reveals that in case 1 the longitudinal velocity, \bar{u} varies from -0 to 6.5 m/s having an average of 4.97 m/s while in case 2, it ranges from -0.5 to 6.3 m/s with the average to 3.11 m/s. Like impermeable spur, no strong recirculation zone was observed. However, within the spur dike zone the mean velocity was 5.09 m/s in case 1, while in case2 was 2.94 m/s almost 1.7 times lower than without spur case.

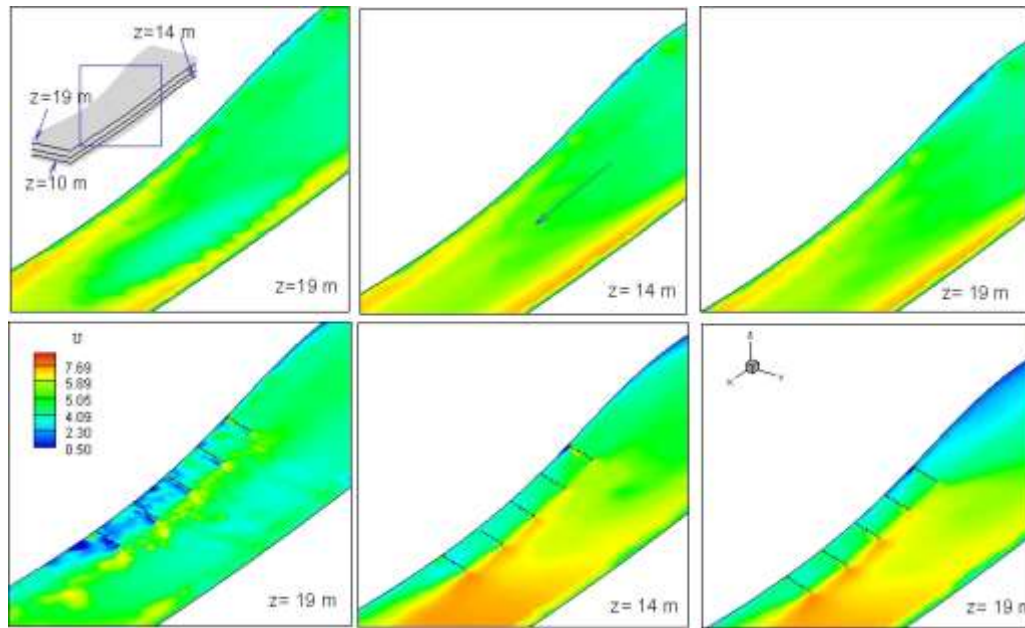


Fig.4.5 Distribution of Longitudinal velocity, \bar{u} (in m/s) at different bed level from the bottom. Top: Case 1 (without spur), Bottom: Case 2 (with spur).

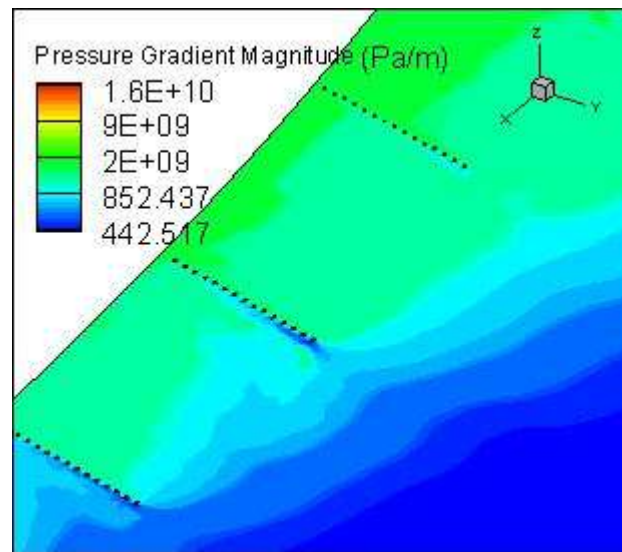


Fig.4.6 Pressure gradient magnitude near the 3rd spur

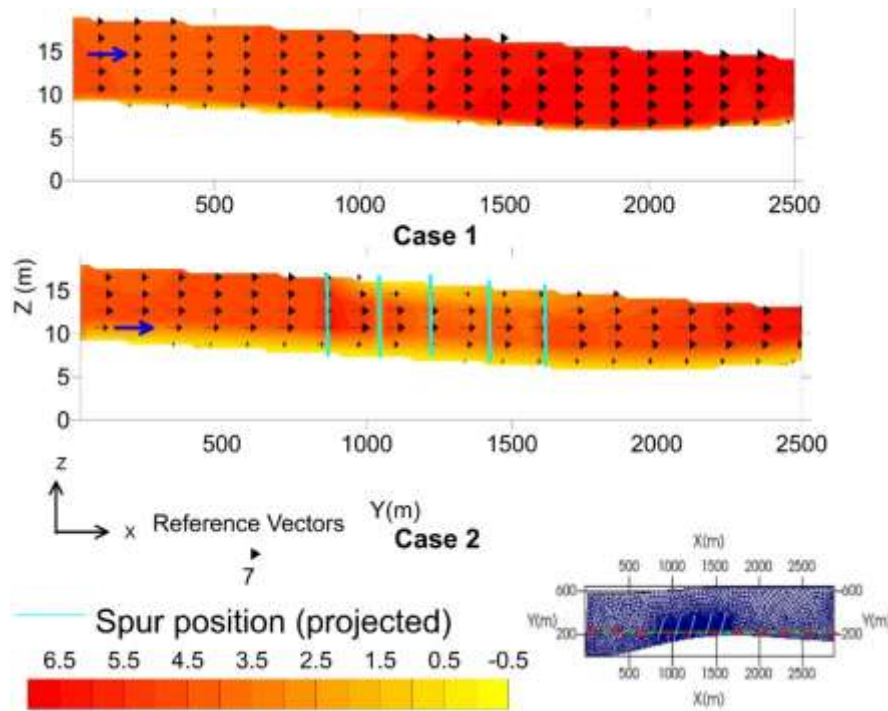


Fig.4.7 The distribution of longitudinal velocity (\bar{u} , \bar{w}) in m/s along the long section. Contours showing the magnitude of transverse velocity, \bar{u} in m/s.

4.4.2 Transverse velocity

The distribution of the transverse velocity \bar{v} and (\bar{v}, \bar{w}) at different cross-sections are shown in Fig.4.8. The sections were taken nearly parallel to the spur with an average distance of 200 m away from the spur (Fig.4.8 down). The transverse velocity ranges from -1.1 to 1.6 m/s. Along the tip of the spur, the magnitude of transverse velocity seems to increase in each section (shown by dotted circle in Fig.4.8). This increment indicates the presence of a detached shear layer along the tip of the spur.

4.4.3 Dam-up

Due to the installation of a spur dike, at the upstream the local water depth increased. This phenomenon, known as dam-up, and the rising of flow depth near the spur (locations are shown in Fig.4.8 bottom image) compared to the averaged water depth in the domain was calculated and shown in Table 4.3. The water depth in the domain was found to be 7.8 m. It shows that the relative dam-up was relatively low before the 2nd and 4th spur. As the position of

these two spur was not parallel with the other three within the spur dike zone, the average relative dam-up was found 0.74 m.

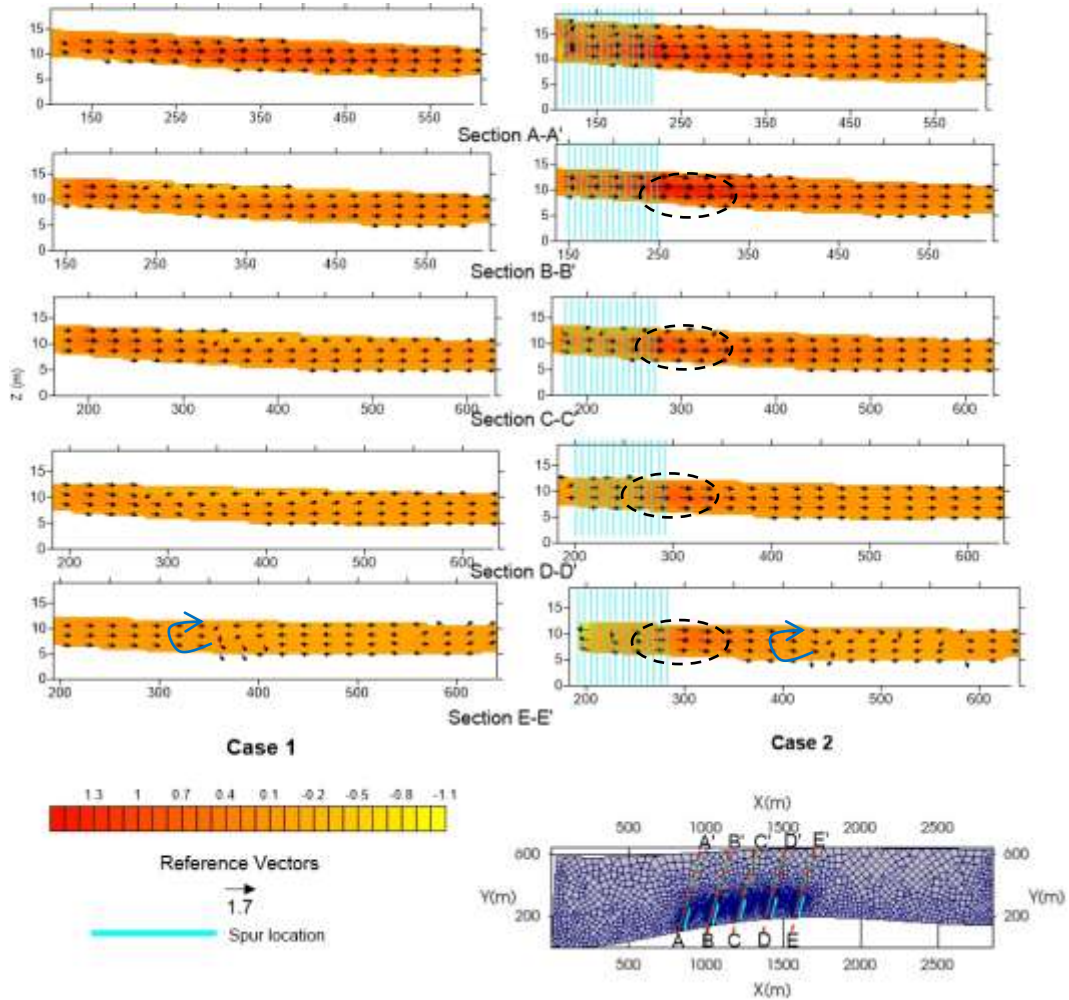


Fig.4.8 The distribution of transverse velocity (\bar{v} , \bar{w}) in m/s along the long section. Contours showing the magnitude of transverse velocity, \bar{v} in m/s.

Table 4.3 Relative dam-up around the spur

Spur	1st	2nd	3rd	4th	5th
Relative Dam-up (m)	0.97	0.62	0.68	0.64	0.78

4.5 Summary

In this part of the research, the effectiveness of slit type spur dike as a bank protection measures in a channel of the sand-bed braided stream was assessed using three-dimensional finite volume numerical simulation. Based on the analysis the conclusion goes as follows:

Using slit type permeable spur dikes as a field, the three-dimensional velocity near the bank can be reduced in the braided channel. However, attention should be given to the flow features generated by the variation of bed geometry as the slit type permeable spur are not fully capable to eradicate the effect of velocity fluctuation due to channel geometry, especially in the longitudinal direction.

By installing the spurs, the bank attacking velocity can be reduced but at the same time, vortical structures are generated due to the installation of the spur. Therefore, prior to installation of this type of structure special precaution should be taken in the zone of the detached shear layer and horseshoe vortex zone.

Slit type permeable spurs produce average relative dam-up near the structure around 0.74 m. At the same time near bed shear stress was also reduced almost 1.4 times compared to without spur case. However, it also increases bed shear stress in the opposite bank.

Like other sand bed braided river, the bed topography of Brahmaputra-Jamuna is very uneven and the channel bed plays a significant role in the distribution of three-dimensional velocity. Hence, prior to design any structure for such channels the analysis for flow features are very crucial.

Chapter 5

Conclusions and recommendations

This study was focused on the management of braided river to mitigate the river bank erosion disaster. Firstly the behavior of the river bed and planform was analyzed through the numerical simulation. Laboratory experiment and numerical study have been conducted on the permeable slit type spur dike as a solution measure. The conclusions of the research have been discussed in the following paragraphs.

5.1 Conclusions

Bed evolution

The bed evolution model of braided river calculated the bed and planform change during one monsoon flood in a compound bar dominated reach of the braided river. The calculation of bed evolution considered two options one is uniform bed sediment and other is considering bed composition of sediment mixture of two different diameter of sediment. Based on the simulations and analysis, the following conclusion can be drawn.

- Using the 2D morphological model the bed evolution of a compounded bar dominated braided river can be done with considerable accuracy. The consideration of bed sorting phenomenon results in better vertical accuracy.
- When the braided river is in expansion phase like the river Brahmaputra-Jamuna, the frequency of deposition on the river bed or braided plain is higher compared to the erosion due to the response of unsteady discharge and water level change during the wet season.
- The development of bar in the vertical direction (here the bar height) behaves similarly to the straight or meandering river but spatial growth (here the bar length) behaves

differently. The dimensionless bar property analysis indicates the spatial growth of braided bar can be skillfully controlled by controlling the width-depth ratio and channel discharge.

- The migration rate of the bars in a compound bar dominated reach of braided river naturally recedes with its growth. Hence, this phenomenon can also be used for better management of the braided river.

Bank erosion countermeasures

This study focusses the countermeasures in an eco-friendly manner hence the focus was to the lowest possible flow obstruction type countermeasure as well as controlling the bifurcation unit of the braided river so that the bank attached channel can be controlled.

Structural Countermeasure

The previous example of hydraulic structure especially the protruding type of structure in sand-bed braided river showed that the failure of structure happened due to local modification of flow that initiates the local scour. As this type of river carries fine noncohesive sediment, hence the local scour triggers the transverse gradient which attracts the braided channel towards the structure and eventually the channel becomes wider and the structure fails. To solve this type of problem lowest possible flow obstruction type countermeasure- slit type permeable spur dike has been suggested and examined through laboratory experiments and numerical simulations. Based on the laboratory experiment and numerical simulation, the following conclusion can be drawn.

- Through the laboratory experiments and numerical simulations, this study investigated the flow structure around slit type permeable spur dike field including several layout alternatives for practical use. The hydrodynamic model consisting 3D RANS equations coupled with $k-\omega$ SST turbulence closures and the VOF method showed good agreement with the experimental results in reproducing the flow structure around very permeable pile spur dike field.
- This study revealed that using slit type permeable spur dike as a field, the approach velocity of flow can be reduced into a considerable amount within the spur dike zone.

- Attractive type of spur dike seems to be a better choice in reducing the longitudinal velocity within the spur dike region. However, deflecting type of spurs were more successful in producing transverse flow to the opposite bank.
- This study also indicated that arranging the pile in a staggered grid within different spur brought better functionality in the spur dike field in terms of reducing the bed shear stress and creating quasi-uniform turbulence zone. However, high bed shear stress at the spur tip, especially for the initial spur, cannot be avoided in this type of spur dike field too. Hence, for field application of this type of structure, better protection measure should be taken for the initial spurs.

Non-Structural Countermeasure

As a non-structural countermeasure, the control of bifurcation by switching one single channel has been proposed. The 2D model developed in chapter 2 has been used in this analysis. The geometry of the upstream channel prior to bifurcation plays the major role in switching by distributing the discharge. However, the characteristics of mid-channel bar seem indirect effect on switching but the geometry of the upstream channel influence greatly by the properties of mid-channel bar.

Based on the simulations and analyses, the conclusions go as follows

- In the wide sand-bed braided river the cross-sectional variation of the water level has been observed but in case of switching this variation does not have any effect. In the case of bifurcation switching, upstream control (discharge) has more effect compared to the downstream control (water level);
- Unbalance in discharge is higher in case of the high aspect ratio of the upstream channel. It lowered down as it approached the symmetrical configuration. But as it reaches its threshold the switching happened;
- At lower shield stress higher asymmetry of discharge distribution is observed. Towards the symmetrical configuration, shields stress becomes higher. After the switch discharge ratio become stable with the fluctuation of shields stress;
- This research indicates there may not be any plausible relationship between bifurcation angle and the switching phenomenon;

- The dimension of the downstream mid-channel bar affects the switching phenomenon by affecting the upstream channel's aspect ratio not directly influencing the discharge distribution.

Application of slit-type spur in a braided channel

In this part, the effectiveness of slit type spur dike as a bank protection measures in a finite volume numerical channel of the sand-bed braided stream has been assessed using the three-dimensional model developed in chapter 3. Based on the analysis we conclude the following:

- Using slit type permeable spur dikes as a field, the three-dimensional velocity near the bank can be reduced in the braided channel. However, attention should be given to the flow features generated by the variation of bed geometry as the slit type permeable spur are not fully capable to eradicate the effect of velocity fluctuation due to channel geometry, especially in the longitudinal direction.
- The results of without spur case give a clear indication that in this braided channel the transverse velocity is large enough to initiate the local scour. By installing the spurs, the bank attacking transverse velocity can be reduced but at the same time, vortical structures are generated due to the installation of the spur. Therefore, prior to installation of this type of structure special precaution should be taken in the zone of the detached shear layer and horseshoe vortex zone.

5.2 Recommendations for future study

- ✓ Prediction of the complex growth of compound bar can be done using 2D morphodynamic model. But finer bathymetry data is needed for simulating some small-scale property (e.g. formation of chute channel over the bar).
- ✓ In this study 1D, bed sorting phenomenon has been considered. In the real field, the large dune possesses coarser sediment in its trough and finer sediment along its crest. When the dune migrates distribution pattern is nearly 2D. Hence, it can be considered as future research.
- ✓ Fixed river bank has been assumed here. The more accurate result can be produced by considering the adaptable bank.

- ✓ The laboratory experiment was conducted on a fixed bed and clear water condition. But movable bed condition will produce a better understanding of sediment distribution.
- ✓ The 3D model only contains the hydrodynamic part. Adding the sediment will be more useful for future research.
- ✓ In the 3D model, the turbulence closer RANS equations were used to match with the experimental data. During the experiment, layer-wise mean velocity was measured. But the measurement of the turbulent component is also suggested for future research. Hence, in that case, Large Eddy Simulation (LES) or Direct Numerical Simulation (DNS) is preferable.
- ✓ The presented 3D model uses standard wall function approach to resolve the wall-bounded area which can be improved by possible integration through the viscous sub-layer and includes the wall roughness more flexible.
- ✓ The study river is characterize with variable bed forms. At the same time, it contains very high suspended sediment concentration which tends to accumulate for building bars/islands or scouring of them with smaller work-done. Hence for stability of any hydraulic structure in this river, smooth passing to the bed form and suspended load should be confirmed.

Reference

- Ackers, P., and White, W. . (1973). "Sediment Transport: New Approach and Analysis." *Journal of the Hydraulics Division, ASCE*, 99(HY11), 204–254.
- Ali, M. S., Hasan, M. M., and Haque, M. (2017). "Two-Dimensional Simulation of Flows in an Open Channel with Groin-Like Structures by iRIC Nays2DH." *Mathematical Problems in Engineering*, 2017.
- Anderson, A. G. (1967). "On the development of stream meanders." *Proceedings of IAHR*.
- Ashida, K., and Michiue, M. (1972). "Study on Hydraulic Resistance and Bed-Load Transport Rate in Alluvial Streams." *Proceedings of the Japan Society of Civil Engineers*, 1972(206), 59–69.
- Ashida, K., and Shiomi, Y. (1966). *Study on the hydraulic behaviors of dunes (meander) in channels*. Disaster Prevention Research Institute Annuals.
- Ashmore, P. (1982). "Laboratory modelling of gravel braided stream morphology." *Earth Surface Processes and Landforms*.
- Ashmore, P. (1991). "How do gravel-bed rivers braid?" *Canadian journal of earth sciences*.
- Ashworth, P. J. (1996). "Mid-channel bar growth and its relationship to local flow strength and direction." *Earth Surface Processes and Landforms*, 21(2), 103–123.
- Ashworth, P., Smith, G. S., and Best, J. (2011). "Evolution and sedimentology of a channel fill in the sandy braided South Saskatchewan River and its comparison to the deposits of an adjacent compound bar."
- Bagnold, R. A. (1956). "The Flow of Cohesionless Grains in Fluids." *Proc. Royal Soc. Philos.Trans.*, 249.
- Bagnold, R. A. (1966). "An Approach to the Sediment Transport Problem From General Physics." *Geological Survey Professional Paper*, 422(I), 1–37.
- Baki, A. B. M., and Gan, T. Y. (2012). "Riverbank migration and island dynamics of the braided Jamuna River of the Ganges-Brahmaputra basin using multi-temporal Landsat images." *Quaternary International*, Elsevier, 263, 148–161.
- Bakker, W. T., Hulsbergen, C. H., Roelse, P., De Smit, C., and Svasek, J. N. (1984). "Permeable groynes: experiments and practice in the Netherlands." *Coastal Engineering*, 649–660.
- Bartley, R., and Rutherford, I. (2005). "Measuring the reach-scale geomorphic diversity of streams: Application to a stream disturbed by a sediment slug." *River Research and Applications*, 21(1), 39–59.

- Berberović, E., Van Hinsberg, N. P., Jakirlić, S., Roisman, I. V., and Tropea, C. (2009). “Drop impact onto a liquid layer of finite thickness: Dynamics of the cavity evolution.” *Physical Review E - Statistical, Nonlinear, and Soft Matter Physics*, 79(3).
- Bertoldi, W., and Tubino, M. (2007). “River bifurcations: Experimental observations on equilibrium configurations.” *Water Resources Research*, 43(10).
- Bertoldi, W., Zanoni, L., and Tubino, M. (2009). “Planform dynamics of braided streams.” *Processes and Landforms*.
- Best, J. (2005). “The fluid dynamics of river dunes: A review and some future research directions.” *Journal of Geophysical Research: Earth Surface*, 110(4), 1–21.
- Best, J. L., Ashworth, P. J., Bristow, C. S., and Roden, J. (2003a). “Three-Dimensional Sedimentary Architecture of a Large, Mid-Channel Sand Braid Bar, Jamuna River, Bangladesh.” *Journal of Sedimentary Research*, 73(4), 516–530.
- Best, J. L., Ashworth, P. J., Bristow, C. S., and Roden, J. (2003b). “Three-Dimensional Sedimentary Architecture of a Large, Mid-Channel Sand Braid Bar, Jamuna River, Bangladesh.” *Journal of Sedimentary Research*, 73(4), 516–530.
- Best, J. L., Ashworth, P. J., Sarker, M. H., and Roden, J. E. (2007). “The Brahmaputra-Jamuna River , Bangladesh.”
- Best, J., Woodward, J., Ashworth, P., and Smith, G. (2006). “Bar-top hollows: A new element in the architecture of sandy braided rivers.” *Sedimentary*.
- Bhuiyan, A. F., Hossain, M. M., and Heyl, R. (2002). “Bank erosion and protection on the Brahmaputra (Jamuna) River.” *Hydraulic Information Management*, C. A. Brebbia and W. R. Blain, eds., 10.
- Blom, A. (2008). “Different approaches to handling vertical and streamwise sorting in modeling river morphodynamics.” *Water Resources Research*, 44(3), 1–16.
- Bolla Pittaluga, M., Repetto, R., and Tubino, M. (2003a). “Channel bifurcation in braided rivers: Equilibrium configurations and stability.” *Water Resources Research*, 39(3), 1–13.
- Bolla Pittaluga, M., Repetto, R., and Tubino, M. (2003b). “Channel bifurcation in braided rivers: Equilibrium configurations and stability.” *Water Resources Research*, 39(3), 1–13.
- Bracmort, K. S., Arabi, M., Frankenberger, J. R., Engel, B. a, and Arnold, J. G. (2006). “Modeling Long-Term Water Quality Impact of Structural BMPs.” *Transactions of the American Society of Agricultural and Biological Engineers*, 49(2), 367–374.
- Brice, J. C., Blodgett, J. C., and Others, A. (1978). *Countermeasures for hydraulic problems at bridges*. Washington, DC.
- Bryant, S., and Mosselman, E. (2017). “Taming the Jamuna: effects of river training in Bangladesh.” *NCR days 2017, Book of abstracts*, A. J. F. Hoitink, T. V. de Ruijscher, T. J. Geertsema, B. Makaske, J. Wallinga, J. H. J. Candel, and J. Poelman, eds., NCR

- publication 41-2017, 114.
- Cao, X., Gu, Z., and Tang, H. (2013). "Study on spacing threshold of nonsubmerged spur dikes with alternate layout." *Journal of Applied Mathematics*, 2013.
- Coleman, J. M. (1969). "Brahmaputra river: Channel processes and sedimentation." *Sedimentary Geology*, 3(2-3), 129-239.
- Colombini, M., Seminara, G., and Tubino, M. (1987). "Finite-amplitude alternate bars." *Journal of Fluid Mechanics*, 181(1), 213.
- Copeland, R. R. (1983). *Bank protection techniques using spur dikes (No. WES/MP/HL-83-1)*.
- DHI, and Hydraulics, D. (1996). *Floodplain levels and bankfull discharge*. Dhaka.
- Duan, J. G. (2009). "Three-dimensional Mean Flow and Turbulence around a Spur Dike." *Journal of Hydraulic Engineering*, 135(10), 803-811.
- Duan, J. G., He, L., Fu, X., and Wang, Q. (2009). "Mean flow and turbulence around experimental spur dike." *Advances in Water Resources*, Elsevier Ltd, 32(12), 1717-1725.
- Einstein, H. A., and Shen, H. W. (1964). "A study on meandering in straight alluvial channels." *Journal of Geophysical Research*, 69(24), 5239-5247.
- Engelund, F., and Hansen, E. (1967). *A Monograph on Sediment Transport in Alluvial Streams*. Teknisk forlag- Copenhagen, Teknisk Forlag, Copenhagen, Denmark.
- Engelund, F., and Skovgaard, O. (1973). "On the origin of meandering and braiding in alluvial streams." *Journal of Fluid Mechanics*, 57(2), 289-302.
- Exner, F. M. (1925). "On the interaction between water and sediment in rivers." *Akad. Wiss. Wien Math. Naturwiss. Klasse*, 134(2a), 165-204.
- FAP 24. (1996). *River Survey Project, Special Report 9*.
- Federici, B., and Paola, C. (2003). "Dynamics of channel bifurcations in noncohesive sediments." *Water Resources Research*, 39(6), n/a-n/a.
- Federici, B., and Seminara, G. (2003). "On the convective nature of bar instability." *Journal of Fluid Mechanics*, 487, S0022112003004737.
- Ferguson, R. I. (1993). "Understanding braiding processes in gravel-bed rivers: progress and unsolved problems." *Geological Society, London, Special Publications*, 75(1), 73-87.
- Filip Schuurman. (2015). "Bar and channel evolution in meandering and braiding rivers using physics-based modeling." Utrecht University.
- Fredsøe, J. (1978). "Meandering and braiding of rivers." *Journal of Fluid Mechanics*, 84(4), 609-624.
- Fujita & Muramoto. (1982). "Experimental Study on Stream Channel in Alluvial Rivers."

- Bulletin of the Disaster Prevention Research Institute*, 32(288), 49–96.
- Fujita Y. (1989). “Bar and channel formation.” in Ikeda, S., and Parker, G., eds., *River Meandering: Washington D.C., American Geophysical Union*, Water Reso, 417–462.
- Fukuoka, S., Watanbe, A., Kawaguchi, H., and Yasutake, Y. (2000). “A study of permeable groins in series installed in a straight channel. Annual Journal of Hydraulic Engineering.” *Annual Journal of Hydraulic Engineering*, 44(1), 1047–1052.
- Ghodsian, M., and Vaghefi, M. (2009). “Experimental study on scour and flow field in a scour hole around a T-shape spur dike in a 90° bend.” *International Journal of Sediment Research*, International Research and Training Centre on Erosion and Sedimentation and the World Association for Sedimentation and Erosion Research, 24(2), 145–158.
- Gissoni, C., and Hager, W. H. (2008). “Spur Failure in River Engineering.” *Journal of Hydraulic Engineering*, 134(2), 135–145.
- Goodbred, S. L., and Kuehl, S. A. (2000). “(Goodbred etal 2000) The significance of large sediment supply, active tectonism, and in ganga Bramhaputra delta.pdf.” 133, 227–248.
- Goswami, D. (1985). “Brahmaputra River, Assam, India: Physiography, Basin Denudation, and Channel Aggradation.” *Water Resources Research*, 21(7), 959–978.
- Gu, Z. peng, Akahori, R., and Ikeda, S. (2011). “Study on the transport of suspended sediment in an open channel flow with permeable spur dikes.” *International Journal of Sediment Research*, International Research and Training Centre on Erosion and Sedimentation and the World Association for Sedimentation and Erosion Research, 26(1), 96–111.
- Gupta, A. (2007). *Large rivers : geomorphology and management*. John Wiley & Sons.
- Gupta, H. V., Sorooshian, S., and Yapo, P. O. (2001). “Status of Automatic Calibration for Hydrologic Models: Comparison With Multilevel Expert Calibration.” *Journal of Hydrologic Engineering*, 4(2), 135–143.
- Hansen, E. (1967). *On the formation of meanders as a stability problem*.
- Hellsten, a. (1998). “k-omega SST Turbulence Model 29th AIAA Fluid Dynamics Conference.” *AIAA Fluid Dynamics Conference*, 2–12.
- Hirano, M. (1971). “River bed degradation with armoring.” *Proceedings of the Japan Society of Civil Engineers*, 1971(195), 55–65.
- Hirsch C. (2007). *Numerical computation of internal & external flows: fundamentals of numerical discretization*. (Butterworth-Heinemann, ed.), Elsevier.
- Hirt, C. W., and Nichols, B. D. (1981). “Volume of fluid (VOF) method for the dynamics of free boundaries.” *Journal of Computational Physics*, 39(1), 201–225.
- Howard, A. D., Keetch, M. E., and Vincent, C. L. (1970). “Topological and Geometrical Properties of Braided Streams.” *Water Resources Research*, 6(6), 1674–1688.

- Ikeda, S. (1982). "Lateral bed load transport on side slopes." *Journal of the Hydraulics Division* 108, 108(11 (1982)), 1369–1373.
- Ikeda, S. (1984). "Prediction of Alternate Bar Wavelength and Height." *Journal of Hydraulic Engineering*, 110(4), 371–386.
- Ikeda, S., and Parker, G. (1989). "River Meandering." *Water Resources Monograph* 12, American Geophysical Union, 12, 379–416.
- Issa, R. I. (1985). "Solution of the implicitly discretised fluid flow equations by operator-splitting." *Journal of computational physics*, 62(1), 40–65.
- Jagers, H. (2003). "Modelling planform changes of braided rivers." Universiteit Twente.
- Jang, C.-L., and Shimizu, Y. (2005). "Numerical Simulation of Relatively Wide, Shallow Channels with Erodible Banks." *Journal of Hydraulic Engineering*, 131(7), 565–575.
- Jasak, H. (1996). "Error Analysis and Estimation for the Finite Volume Method with Applications to Fluid Flows." *PhD Thesis*, M(June), 394.
- Jowett, I. G., and Duncan, M. J. (2012). "Effectiveness of 1D and 2D hydraulic models for instream habitat analysis in a braided river." *Ecological Engineering*, Elsevier B.V., 48, 92–100.
- Kabir, M. R., and Ahmed, N. (1996). "Bed Shear Stress for Sediment Transportation in the River Jamuna." *Journal of Civil Engineering, The Institution of Engineers, Bangladesh*, 24(June), 55–68.
- Kalitzin, G., Medic, G., Iaccarino, G., and Durbin, P. (2005). "Near-wall behavior of RANS turbulence models and implications for wall functions." *Journal of Computational Physics*, 204(1), 265–291.
- Kang, J., Yeo, H., Kim, S., and Ji, U. (2011). "Permeability effects of single groin on flow characteristics." *Journal of Hydraulic Research*, 49(6), 728–735.
- Klaassen, G. J., Mosselman, E., and Brühl, H. (1993). "On the prediction of planform changes in braided sand-bed rivers." *Advances in Hydro-Science and -Engineering*.
- Klaassen, G. J., and Vermeer, K. (1988). "Confluence scour in a large braided river with fine bed material." *Proceedings of the International Conference on Fluvial Hydraulics*, International Association of Hydraulic Research, Budapest, Hungary, 395–408.
- Kleinhans, M. G., and van den Berg, J. H. (2011). "River channel and bar patterns explained and predicted by an empirical and a physics-based method." *Earth Surface Processes and Landforms*, 36(6), 721–738.
- Kleinhans, M. G., Ferguson, R. I., Lane, S. N., and Hardy, R. J. (2012). "Splitting rivers at their seams : bifurcations and avulsion."
- Kleinhans, M. G., Jagers, B., Mosselman, E., and Sloff, K. (2006). "Effect of upstream meanders on bifurcation stability and sediment division in 1D, 2D and 3D models." *River flow 2006 : proceedings of the International Conference on Fluvial Hydraulics*,

Lisbon, Portugal, 6-8 September 2006, 1355–1362.

- Koken, M., and Constantinescu, G. (2008). “An investigation of the flow and scour mechanisms around isolated spur dikes in a shallow open channel: 1. Conditions corresponding to the initiation of the erosion and deposition process.” *Water Resources Research*, 44(8), 1–19.
- Koken, M., and Constantinescu, G. (2011). “Flow and turbulence structure around a spur dike in a channel with a large scour hole.” *Water Resources Research*, 47(12), 1–19.
- Kuhnle, R. a, Alonso, C. V, and Shields, F. D. (2002). “Local Scour Associated with Angled Spur Dikes.” *Journal of Hydraulic Engineering*, 128(12), 1087–1093.
- Kuhnle, R., and Alonso, C. (2013). “Flow near a model spur dike with a fixed scoured bed.” *International Journal of Sediment Research*, International Research and Training Centre on Erosion and Sedimentation and the World Association for Sedimentation and Erosion Research, 28(3), 349–357.
- Leendertse, J. J., Alexander, R. C., and Liu, S.-K. (1977). *A three-dimensional model for estuaries and coastal seas. Volume I: Principles of Computations Report R-1417-OWRR, Rand Corporation, Santa Monica, CA. Volume II: Aspects of computation, R-1764-OWRT, Volum.* Santa Monica, CA.
- Leendertse, J. J., and Gritton, E. C. (1971). *A water quality simulation model for well mixed estuaries and coastal seas: Vol. II, Computation Procedures.* Santa Monica, CA.
- Leopold, L. B., Wolman, M. G. (1957). “River channel patterns: braided, meandering and straight.” *US Geological Survey Professional Papers*, 282B, 39–85.
- Leopold, B. L., and Wolman, M. G. (1957a). *River channel patterns: Braided, meandering, and straight.* Washington, D.C.
- Leopold, L. B., and Wolman, M. G. (1957b). *River channel patterns: braided, meandering, and straight.* Geological survey professional paper.
- Li, Y., and Altinakar, M. (2016). “Effects of a Permeable Hydraulic Flashboard Spur Dike on Scour and Deposition Yujian.” *World Environmental and Water Resources Congress 2016*, 399–409.
- Li, Z., Kohji, M., Maeno, S., Ushita, T., and Fujii, A. (2005). “Hydraulic characteristics of a group of permeable groins constructed in an open channel flow.” *Journal of Applied Mechanics, JSCE*, Vol. 8(1), 773–782.
- Melville, B. W., and Coleman, S. E. (2000). *Bridge scour.* Water Resources Publication, Littleton, Colo.
- Menter, F. R. (1994). “Two-equation eddy-viscosity turbulence models for engineering applications.” *AIAA Journal*, 32(8), 1598–1605.
- Menter, F. R., Kuntz, M., and Langtry, R. (2003). “Ten years of industrial experience with the SST turbulence model.” *Fourth international symposium on turbulence, heat and mass transfer*, Begell House, Antalya, Turkey, 625–632.

- Meyer-Peter, E., and Müller, R. (1948). "Formulas for bed-load transport." *IAHSR 2nd meeting*, Stockholm.
- Mioduszewski, T., and Maeno, S. (2005). "Three Dimensional Around a Porous Analysis Spur of Flow Dike." 8(August), 793–801.
- Moriassi, D. N., Arnold, J. G., Van Liew, M. W., Bingner, R. L., Harmel, R. D., and Veith, T. L. (2007). "Model Evaluation Guidelines for Systematic Quantification of Accuracy in Watershed Simulations." *Transactions of the ASABE*, 50(3), 885–900.
- Mosley, M. P. (1983). "Response of braided rivers to changing discharge." *Journal of Hydrology (New Zealand)*, 22, 18–67.
- Mosley, P. M. (1976). "An Experimental Study of Channel Confluences." *The Journal of Geology*, 84(5), 535–562.
- Mosselman, E. (2009). "Bank protection and river training along the braided Brahmaputra-Jamuna River, Bangladesh." *Braided Rivers: Process, Deposition, Ecology and Management*, G. Smith, J. Best, C. Bristow, and G. Petts, eds., Blackwell, Oxford, UK, 277–287.
- Murray, A. B., and Paola, C. (1994). "A cellular model of braided rivers." *Nature*.
- Nakagawa, H., and Nezu, I. (1977). "Prediction of the contributions to the Reynolds stress from bursting events in open-channel flows." *Journal of Fluid Mechanics*, 80(1), 99–128.
- Nakagawa, H., Zhang, H., Baba, Y., Kawaike, K., and Teraguchi, H. (2013). "Hydraulic characteristics of typical bank-protection works along the Brahmaputra/Jamuna River, Bangladesh." *Journal of Flood Risk Management*, 6(4), 345–359.
- Nanson, G., and Knighton, A. (1996). "Anabranching rivers: Their cause, character and classification." *Earth Surface Processes and Landforms*, 21(3), 217–239.
- Next Foam. (2013). "Boundary Conditions- OpenFOAM-2.3.0." *CFL 3D Manual*.
- Nicholas, A. P., Ashworth, P. J., Sambrook Smith, G. H., and Sandbach, S. D. (2013). "Numerical simulation of bar and island morphodynamics in anabranching megarivers." *Journal of Geophysical Research: Earth Surface*, 118(4), 2019–2044.
- Nones, M., and Di Silvio, G. (2016). "Modeling of River Width Variations Based on Hydrological, Morphological, and Biological Dynamics." *Journal of Hydraulic Engineering*, 142(7), 04016012.
- OpenCFD. (2009). "Programmer's Guide." *OpenFOAM, The Open Source CFD Toolbox*.
- Papanicolaou, A. N. T., Krallis, G., and Edinger, J. (2008). "Sediment Transport Modeling Review — Current and." 134(January), 1–14.
- Paper, C., Infor, G., and Education, W. (2011). "River bank protection measures in the Brahmaputra-Jamuna River : Bangladesh Experience." (May).
- Parker, G. (1976). "On the cause and characteristic scale of meandering and braiding in

- rivers. *Journal of Fluid Mechanics* 76: 459-480.” *Journal of Fluid Mechanics*, 76, 459–480.
- Patankar, S. V., and Spalding, D. B. (1972). *A calculation procedure for heat, mass and momentum transfer in three-dimensional parabolic flows. International Journal of Heat and Mass Transfer*, Pergamon Press, Ltd.
- Peaceman, D. W., and H. H. Rachford, J. (1955). “The numerical solution of parabolic and elliptic differential equations.” *J. Soc. Indust. Appl. Math.*, 3(1), 28–41.
- Piégay, H., Grant, G., Nakamura, F., and Trustrum, N. (2006). “Braided river management: from assessment of river behaviour to improved sustainable development.” *Braided Rivers*, 257–275.
- Przedwojski, B., Błażejowski, R., and Pilarczyk, K. W. (1995). “River training techniques: fundamentals, design and applications.” *River training techniques: fundamentals, design and applications.*, A.A. Balkema.
- Rajaratnam, N., and Nwachukwu, B. a. (1983). “Flow Near Groin-Like Structures.” *Journal of Hydraulic Engineering*, 109(3), 463–480.
- Raudkivi, A. J. (1996a). “Permeable Pile Groins.” *Journal of Waterway, Port, Coastal, and Ocean Engineering*, 122(6), 267–272.
- Raudkivi, A. J. (1996b). “Chapter 166.” *Journal of Waterway, Port, Coastal, and Ocean Engineering*, 122(6), 2142–2151.
- Reynolds, A. J. (1965). “Waves on an erodible bed.” *J. Fluid Mech.*, 22, 113–133.
- Ribberink, J. S. (1987). “Mathematical modelling of one-dimensional morphological changes in rivers with non-uniform sediment.” *Faculty of Civil Engineering*, Doctoral.
- van Rijn, L. C. (1993). *Principles of sedimentation and erosion engineering in rivers, estuaries and coastal seas*. Aqua publications.
- Van Rijn, L. C. (1984). “Sediment transport: bed load transport.” *Journal of Hydraulic Engineering--ASCE*, 110(10), 1431–1456.
- Van Rijn, L. C. (1993). *Principles of sediment transport in rivers, estuaries and coastal seas*. Amsterdam: Aqua publications.
- Roden, J. E. (1998). “The Sedimentology and Dynamics of Mega-Dunes , Jamuna by.” University of Leeds.
- Rodi, W. (2006). “DNS and LES of some engineering flows.” *Fluid Dynamics Research*, 38(2–3), 145–173.
- Roelvink, D., Lesser, G., and Wegen, M. van der. (2006). “Evaluation of the Long Term Impacts of an Infiltration BMP Drexel E-Repository and Archive (iDEA) Please direct questions to archives@drexel.edu.” *Proceedings of the 7 th International Conference on HydroScience and Engineering College of Engineering*, A. Welker and R. Traver, eds., 1–6.

- Rosgen, D. L. (1994). "A classification of natural rivers." *Catena*, 22, 169–199.
- Safarzadeh, A., Ali, S., Salehi, A., and Zarrati, A. R. (2016). "Experimental Investigation on 3D Turbulent Flow around Straight and T-Shaped Groynes in a Flat Bed Channel." *Journal of Hydraulic Engineering*, 142(2014), 1–15.
- Sambrook, G. H., Best, J. L., Bristow, C. S., and Petts, G. E. (2009). *Braided Rivers: Process, Deposits, Ecology and Management (Special Publication 36 of the IAS)*. Blackwell, Oxford, UK.
- Santhi, C., Arnold, J. G., Williams, J. R., Dugas, W. a., Srinivasan, R., and Hauck, L. M. (2002). "Validation of the SWAT model on a large river basin with point and nonpoint sources." *Journal of the American Water Resources Association (JAWRA)*, 37(5), 1169–1188.
- Sarker, M. H. (2008). "Morphological Response of the Brahmaputra-Padma-Lower Meghna River System to the Assam Earthquake of 1950." University of Nottingham.
- Sarker, M. H., Akter, J., and Ruknul, M. (2011a). "River bank protection measures in the Brahmaputra-Jamuna River: Bangladesh experience." *International Seminar on River, Society and Sustainable Development, Dibrugarh University, India*, (May).
- Sarker, M. H., Akter, J., and Ruknul, M. (2011b). "River bank protection measures in the Brahmaputra-Jamuna River: Bangladesh experience." *International Seminar on River, Society and Sustainable Development, Dibrugarh University, India*.
- Sarker, M. H., Huque, I., and Alam, M. (2003). "Rivers , chars and char dwellers of Bangladesh." 1(1), 61–80.
- Sarker, M. H., Thorne, C. R., Aktar, M. N., and Ferdous, M. R. (2014). "Morpho-dynamics of the Brahmaputra-Jamuna River, Bangladesh." *Geomorphology*, Elsevier B.V., 215, 45–59.
- Schumm, S. (1960). "The Shape of Alluvial Channels in Relation To Sediment Type." *Office*, 24.
- Schumm, S. A. (1963). "A tentative classification of alluvial river channels." *USGS Circular*, 477, 10p.
- Schumm, S. A. (1985). "Patterns of alluvial rivers." *Annual Review of Earth and Planetary Sciences*, 13(1), 5–27.
- Schuurman, F., and Kleinhans, M. G. (2015). "Bar dynamics and bifurcation evolution in a modelled braided sand-bed river." *Earth Surface Processes and Landforms*, 40(10), 1318–1333.
- Schuurman, F., Marra, W. A., and Kleinhans, M. G. (2013). "Physics-based modeling of large braided sand-bed rivers: Bar pattern formation, dynamics, and sensitivity." *Journal of Geophysical Research: Earth Surface*, 118(4), 2509–2527.
- Schuurman, F., Ta, W., Post, S., Sokolewicz, M., Busnelli, M., and Kleinhans, M. (2018). "Response to peak discharge in braiding Yellow River." *Earth Surface Processes and*

Landforms, (January).

- Shampa. (2015). “Dynamics of bar in the braided river Jamuna.” Bangladesh University of Engineering and Technology.
- Shampa, and Ali, M. M. (2018). “Interaction between the braided bar and adjacent channel during flood: a case study of a sand-bed braided river, Brahmaputra–Jamuna.” *Sustainable Water Resources Management*, Springer International Publishing, 1–14.
- Shampa, Hasegawa, Y., Nakagawa, H., Takebayashi, H., and Kawaike, K. (2017a). “Dynamics of sand bars in braided river : a case study of brahmaputra-jamuna river dynamics of sand bars in braided river : a case study of brahmaputra-jamuna river.” *Journal of Japan Society of Natural Disaster science*, 36(Special), 121–135.
- Shampa, Hasegawa, Y., Nakagawa, H., Takebayashi, H., and Kawaike, K. (2017b). “Dynamics of Sand Bars in Braided River: A Case Study of Brahmaputra-Jamuna River.” *自然灾害科学. Jsnds*, 36, 123–137.
- Shen, H. ., and Komura, S. (1968). “Meandering tendencies in straight alluvial channels.” *Journal of Hydraulic Division, Proceedings of American Society of Civil Engineering*, 94(HY4), 997–1016.
- Simpson, C. J., and Smith, D. G. (2001). “The braided Milk River, Northern Montana, fails the Leopold-Wolman discharge-gradient test.” *Geomorphology*, 41(4), 337–353.
- Stelling, G. S., and Leendertse, J. J. (1992). “Approximation of Convective Processes by Cyclic AOI Methods.” *Estuarine and Coastal Modeling*, ASCE, 771–782.
- Takebayashi, H., Egashira, S., and Okabe, T. (2003). “Numerical analysis of braided streams formed on beds with non-uniform sediment.” *Journal of Hydroscience and Hydraulic Engineering, Japan Society of Civil Engineering*, 47(2), 634–636.
- Thomas, R., and Nicholas, A. P. (2002). “Simulation of braided river flow using a new cellular routing scheme.” *Geomorphology* 43, 43(2), 179–195.
- Thorne, C. R., Russell, A. P. G., and Alam, M. K. (1993). “Planform pattern and channel evolution of the Brahmaputra River, Bangladesh.” *Geological Society, London, Special Publications*, 75(1), 257–276.
- Uijtewaal, W. S. (2005a). “Effects of Groyne Layout on the Flow in Groyne Fields: Laboratory Experiments.” *Journal of Hydraulic Engineering*, 131(September), 782–791.
- Uijtewaal, W. S. (2005b). *Water quality hazards and dispersion of pollutants*. (W. Czernuszenko and P. Rowinski, eds.), Springer, Boston, MA.
- Umitsu, M. (1993). “Late quaternary sedimentary environments and landforms in the Ganges Delta.” *Sedimentary Geology*, 83(3–4), 177–186.
- Wang, Z. B., De Vries, M., Fokkink, R. J., and Langerak, A. (1995). “Stability of river bifurcations in ID morphodynamic models.” *Journal of Hydraulic Research*, 33(6), 739–750.

- Watanabe, Y., Tubino, M., Zolezzi, G., and Hoshi, K. (2001). "Behavior of alternate bars under unsteady flow conditions." *Proceedings of 2nd IAHR Symposium on River, Coastal and Estuarine Morphodynamics*, 575–584.
- Weller, H. G. (2002). *Derivation, modelling and solution of the conditionally averaged two-phase flow equations. Technical Report TR/HGW/02.*
- Weller, H. G., Tabor, G., Jasak, H., and Fureby, C. (1998). "A tensorial approach to computational continuum mechanics using object-oriented techniques." *Computers in Physics*, 12(6), 620–631.
- Werner, P. G. (1951). "On the origin of river meanders." *Trans, American Geophysical Union*, 32(6), 898–902.
- Williams, R. D., Brasington, J., and Hicks, D. M. (2016). "Numerical Modelling of Braided River Morphodynamics: Review and Future Challenges." *Geography Compass*, 10(3), 102–127.
- Williams, R. D., Brasington, J., Hicks, M., Measures, R., Rennie, C. D., and Vericat, D. (2013). "Hydraulic validation of two-dimensional simulations of braided river flow with spatially continuous aDcp data." *Water Resources Research*, 49(9), 5183–5205.
- Wu, B., Asce, M., Wang, G., Ma, J., and Zhang, R. (2005). "Case Study: River Training and Its Effects on Fluvial Processes in the Lower Yellow River, China." 131(February), 85–96.
- Yalin, M. S. (1992). *River Mechanics*. Pergamon Press, Oxford.
- Zang, H. (2005). "Study on Flow and Bed Evolution in Channels with Spur Dykes." Kyoto University.
- Zhang, H., Nakagawa, H., Baba, Y., Kawike, K., Rahman, M., and Uddin, M. N. (2011). "Hydraulic and Morphological Consequences of Bank Protection Measures along the Jamuna." (January 2015), 477–496.
- Zhang, H., Nakagawa, H., Ogura, M., and Mizutani, H. (2013). "Experiment Study on Channel Bed Characteristics around Spur Dykes of Different Shapes." 69(2), 489–499.
- Zhou, L. (2017). "Numerical modelling of scour in steady flows."

List of Tables

Table 1.1 The sediment size d_{50} of Brahmaputra-Jamuna	12
Table 3.1 Performance of bank protection structure of Brahmaputra-Jamuna (till 2011) (Sarker et al. 2011a)	54
Table 3.2 Details of Experimental cases	60
Table 3.3 Details of Experimental Conditions	60
Table 3.4 Turbulent model constant	70
Table 3.5 Boundary conditions of the simulations	80
Table 3.6 PBIAS of the considered cases	81
Table 3.7 Spatial velocity increment in main channel due to the spur dike	87
Table 4.1 Mesh details of the considered cases	109
Table 4.2 Boundary condition of the simulation	111
Table 4.3 Relative dam-up around the spur	115

List of Figures

Fig.1.1 Satellite image of the Rio Negro, Branco and Unini River representing the different distinct planform of the river nearly in the same location (location: Manaus, Brazil, Oct 2018)	2
Fig.1.2 Negative impact caused by river in different parts of the world in 2018	2
Fig.1.3 Classification of the river [based on Schumm (1963, 1985)].....	4
Fig.1.4 Anabranching in braided (left: Brahmaputra-Jamuna River, Bangladesh) and meandering (right: Upper Meghna River, Bangladesh) river	5
Fig.1.5 Discharge-slope relationship to identify the river pattern [after (Leopold and Wolman 1957a; Nones and Di Silvio 2016; Simpson and Smith 2001)]	6
Fig.1.6 Major morphological element of the braided river (sand-bed, Brahmaputra).....	7
Fig.1.7 The decadal bank erosion of Brahmaputra-Jamuna River, Bangladesh.....	8
Fig.1.8 Map showing the study area (elevation data courtesy: Google Earth Pro v7.3.2.5491)	11
Fig.1.9 Time series representation of mean daily discharge of Brahmaputra-Jamuna at Bahadurabad station from the year 1956 to 2016	11
Fig.1.10 Average water surface slope at the date of the annual minimum water level [after (Shampa 2015)].....	12
Fig.1.11 Sieve analysis of sediment sample at Sirajganj [after Zhang et al. (2011)]	13
Fig.1.12 The bedforms along the cross-section of Bahadurabad station in May 2011.....	14
Fig.1.13 Examples of different types of the bar in Brahmaputra-Jamuna. CB: compound bar, UB: Unit bar and FB: Forced bar [after Shampa et al. (2017)]	15
Fig.1.14 Westward migration of Brahmaputra-Jamuna-Jamuna [reproduced from Sarker et al. (2014)].....	16
Fig.1.15 Length-averaged bankline migration of the Brahmaputra-Jamuna River [reproduced from Sarker et al. (2014)]	16
Fig.1.16 Yearly change of braided planform near the Bahadurabad station. The satellite images represents the month of February of the respected year	17

Fig.2.1 The types of model used to understand the braided river morphodynamics (Williams et al. 2016). The dashed purple-line indicate the numerical approaches which have conducted during this study.....	20
Fig.2.2 The comparison of bed-load computed using several formulas (Kabir and Ahmed 1996).....	25
Fig.2.3 Definition Sketch of a Vertical bed Profile	29
Fig.2.4 Mapping of physical space to computational space	33
Fig.2.5 The model domain and bathymetry	35
Fig.2.6 Boundary condition of the Model.....	37
Fig.2.7 Calibration of the model for the hydraulic condition of the year 2011 (a,b and c) and validation of the model for the hydraulic condition of the year 2012 (d)	39
Fig.2.8 A schematic definition figure for bar migration calculation from satellite images	41
Fig.2.9 Comparison of real and simulated plan form and time series bed level change ..	43
Fig.2.10 The comparison between initial and final bed level at Mathura due to mixed and uniform bed.....	43
Fig.2.11 Histogram of bed level change	44
Fig.2.12 Map showing an example of bar migration of one bar.....	46
Fig.2.13 Comparison of Bar migration rate derived from satellite image analysis and numerical simulation.....	46
Fig.2.14 Comparison of river erosion location between the satellite image and model...	47
Fig.2.15 Relation between dimensionless width-depth ratios to a) dimensionless bar height b) dimensionless bar length	47
Fig.2.16 Relationship between Dimensionless migration speed to a) width-depth ratio b) bar aspect ratio and c) channel speed stream power for the braided bar in terms of LW ratio	49
Fig.3.1 River bank protection structure used in Brahmaputra-Jamuna (Nakagawa et al. 2013; Sambrook et al. 2009).....	53
Fig.3.2 Conceptual description of flow distribution around a spur dike	55
Fig.3.3 Details of experimental flume	58

Fig.3.4 Spur dike model details	59
Fig.3.5 An example of experimental data measuring location (case 1).....	60
Fig.3.6 Measurement equipment used in the experiment. Left: OMRON’s ultrasonic water level sensor; Right: KENECK’s L type electromagnetic velocity meter	61
Fig.3.7 Dimensionless longitudinal velocity vector, $(\bar{u}/U, \bar{w}/U)$ 0.11m away from the right bank. The contour shows the magnitude of the longitudinal velocity component (\bar{u}/U)	63
Fig.3.8 Longitudinal Distribution of non-dimensional Vertical Velocity Profile wU at $z=0.01\text{m}$ of (a) 900 (b) 1500 and (c) 600 aligned spur dike field.....	64
Fig.3.9 Dimensionless transverse velocity vector $(\bar{v}/U, \bar{w}/U)$ at 0.02m upstream of third spur dike form the upstream. The contour shows the magnitude of the transverse velocity component (\bar{v}/U)	66
Fig.3.10 Transverse Distribution of non-dimensional Vertical Velocity Profile wU at $z=0.01\text{m}$ of (a) 900 (b) 1500 and (c) 600 aligned spur dike field.....	67
Fig.3.11 Spatial distribution of dimensionless water depth (d/h) of different cases.....	68
Fig.3.12 A typical control volume	73
Fig.3.13 Schematic diagram of vertical velocity distribution.....	77
Fig.3.14 An example of computational mesh (case 1).....	79
Fig.3.15 Comparison of experimental and simulated surface velocity in case 1.....	82
Fig.3.16 Comparison of experimental and simulated three-dimensional velocity and water depth.....	84
Fig.3.17 Dimensionless longitudinal velocity vector, $(\bar{u}/U, \bar{w}/U)$ 0.11m away from the right bank. The contour shows the magnitude of longitudinal velocity component (\bar{u}/U)	85
Fig.3.18 Dimensionless transverse velocity vector $(\bar{v}/U, \bar{w}/U)$ at 0.02m upstream of third spur dike form the upstream. The contour shows the magnitude of transverse velocity component (\bar{v}/U)	86
Fig.3.19 Visualization of the vortical structure of the mean flow using Q criterion of case 2.....	87
Fig.3.20 Distribution of Dimensionless spatial velocity $(\bar{u}/U, \bar{v}/U)$ at different depths. The contour shows the magnitude of longitudinal velocity component (\bar{u}/U) ..	89

Fig.3.21 Contours of normalized Reynolds shear stress at $Z=0.01\text{m}$	92
Fig.3.22 Dimensionless bed shear stress calculated from Reynolds stress.....	93
Fig.3.23 (a) Map showing the study area; (b) and (c) changes of the study area over time (d) Model domain of the numerical simulation	96
Fig.3.24 (a) Boundary Condition of the considered cases (b) Definition and terminology used in model result analysis	97
Fig.3.25 (a) Changes of discharge ratio, r_q over time (b) Final bed elevation of the considered cases.....	99
Fig.3.26 Changes of Discharge ratio, r_q with upstream channel aspect ratio, β_a	100
Fig.3.27 Bed share stress of the considered cases at of peak flow	100
Fig.3.28 Change of discharge ratio with the change of upstream channel shield stress.	101
Fig.3.29 Relationship between (a) r_q and angle of bifurcation (b) r_q and aspect ratio of mid channel bar	102
Fig.3.30 The relation between u/s channel aspect ratio to d/s mid-channel bar aspect ratio	103
Fig.4.1 Map showing the study area. (a) The Brahmaputra-Jamuna river reach in Bangladesh (b) and (c) planform and bank line changes in the study area during the year 2011 to 2013.....	107
Fig.4.2 The flow direction and bed shear stress calculated from the 2D model (d) the bathymetry of the study channel (e) without structure finite element mesh used for numerical simulation.....	108
Fig.4.3 The details of the spur dike.....	109
Fig.4.4 Mesh used in the simulation	110
Fig.4.5 Distrbution of Longitudinal velocity, u (in m/s) at different bed level from the bottom. Top: Case 1 (without spur), Bottom: Case 2 (with spur).	113
Fig.4.6 Pressure gradient magnitude near the 3rd spur.....	113
Fig.4.7 The distribution of longitudinal velocity (\bar{u}, \bar{w}) in m/s along the long section. Contours showing the magnitude of transverse velocity, \bar{u} in m/s.....	114
Fig.4.8 The distribution of transverse velocity (\bar{v}, \bar{w}) in m/s along the long section. Contours showing the magnitude of transverse velocity, \bar{v} in m/s.....	115

List of symbols

τ_a	Average bed share stress
∇	Gradient operator for three-dimensional region
S	Bed slope
Ω^*	Dimensionless stream power
S_0	Maximum scour depth
U_o	Monthly mean flow velocity
$ \bar{S}_{bed} $	Bed load transport rate
$(a_{max})_{bn}$	Area of minimum bounding rectangle of determined
\bar{S}_{sus}	Depth average suspended sediment transport vector
$\alpha_{k1}, \alpha_{k2}, \alpha_{\omega2}, \beta^*, \beta, \gamma, c_1, a_1$	Turbulent model coefficients;
Δ_r	Ripple height
$h_{dc,thr}$	Minimum threshold flow depth for reallocating the erosion in dry cell
h_m	monthly maximum water depth
A_f	Area of new compound bar
A_i	Area of old bars from which the compound bar is formed
C_{kmx}	Mass concentration of the sediment fraction in the reference cell
C_s	Roughness constant of wall function

C_μ	Turbulence closure coefficient
D_*	Dimensionless particle parameter
D_v, D_h	Vertical and horizontal diffusion coefficient at the bottom of the reference cell
E_k, D_k	Upward and downward suspended sediment transport flux near the bed for the size fraction k
F_ξ, F_η	Turbulent momentum flux in ξ and η direction respectively
J_ξ, J_η	Coefficients used to transform curvilinear to rectangular coordinates
S_i, O_i	Simulated and observed values, respectively;
S_k	Effective rate of production k
S_ω	Effective rate of production ω
U_*	Experimental Friction Velocity
a_j	Equal width segmented area to the mean flow direction
a_{max}	Area of the largest segment a_j
$c_{d,bs}$	Tuning factor for bed slope effect
c_d	Calibration constant.
c_{eq}	Depth-averaged equilibrium sediment concentration
d_{50}	Mean particle size
f_a	Van Rijn's reference height proportionality factor
f_s	Shape factor for the vertical distribution of suspended sediment
k_e	Current related effective roughness height
k_r	Relative availability of the sediment fraction at the bed
k_s	Equivalent roughness height

k_α	Curvature of the interface
l_{bn}	Longer side length of the minimum bounding rectangle
m_f	Morphological acceleration factor
p_o	Total pressure at outlet
q_{uk}, q_{vk}	Bed load transport vector for the size fraction k
$s_{s,r}$	Correction factor of suspension parameter
s_s	Suspension parameter
t_s	Adaptation time-scale respectively
$\acute{u}, \acute{v}, \acute{w}$	Fluctuation in velocity in the longitudinal, transverse and vertical directions, respectively;
$\bar{u}, \bar{v}, \bar{w}$	Time-averaged mean velocity in the longitudinal, transverse and vertical directions, respectively;
u_*	Bed share velocity
$u_{b,u}, u_{b,v}$ and $ u_b $	Local bottom-layer flow velocity components and magnitude.
ν_h	Kinetic eddy viscosity (horizontal)
z_p	Distance from the wall to the first canter near the wall
\mathbf{U}_a	Air velocity vector
\mathbf{U}_f	Flow velocity vector
\mathbf{U}_r	Relative velocity vector
f_α	Surface tension effects at the free surface
α_b	Bar aspect ratio

α_{bs}	bed slope correction factor
α_{tr}	Transverse bed slope correction factors
α_{tr}	Transversal bed slope correction factor
β_a	Upstream channel aspect ratio,
β_b	Width/depth ratio
β_v	Van Rijn's β factor
η_{bk}	Bed change due to size fraction k ;
$\theta_{dc,thr}$	Maximum fraction of erosion to reallocate from edge wet cells to surrounding dry
cell(s) h_{dcmax}	Flow depth in the wet cell at which the full $\theta_{dc,thr}$ will be reallocated
θ_{dc}	Fraction of erosion in an edge
μ_c	Ratio between the total bed roughness and the grain related bed roughness
μ_m	Molecular viscosity
ρ_a	Density of air;
ρ_f, ρ_s	Density of water and sediment particle respectively
σ_T	Coefficient of surface tension
τ_0	Approach Flow bed shear stress
τ_b	Total bed shear stress;
τ_b^*	Dimensionless bed shear stress;
τ_b^x, τ_b^y	Components of bed shear stress in longitudinal and transverse direction
v_a	Shields stress is defined by equation
ω_m	Migration amount of that particular bar per unit time

ω_s	Particle fall velocity of suspended sediment
ϑ_t	Kinematic (turbulent) viscosity;
ΔA	Newly accredited area of that particular compound bar
c	Mass sediment concentration
D_a	Upstream channel depth
F	Froude number
h	Flow depth
Q	Discharge
R	Reynolds number
r_q	discharge ratio between bifurcated channel
S	source and sink terms per unit area
W_a	Upstream channel width
Γ	Diffusion coefficient
Δz	Vertical distance from the reference level a to the center of reference cell
E	Smooth wall constant
H	Bar amplitude
L	Longest axis gave the length of the bar
T	nondimensional bed shear stress determined by Van Rijn (1993) method
W	Constant channel width of the river
a	Van Rijn's reference height
d	Depth below the reference plane ($h = d + \zeta$)
g	Acceleration due to gravity

k	Sediment size fraction
k	Turbulent kinetic energy
n	Manning's coefficient
p	Pressure
s	Specific density of sediment particle $\left(\frac{\rho_s}{\rho_f}\right)$
u, v	Depth average velocity in the x and y directions, respectively
ν	Kinematic viscosity coefficient $\left(\frac{\mu_m}{\rho}\right)$
\mathbf{U}	Flow velocity vector
\mathbf{g}	Gravitational acceleration vector
α	Phase fraction
ε	Dissipation rate of turbulent energy of Here,
ζ	Water level or free surface elevation above the reference plane (at $z = 0$)
θ	Internal angle of friction of bed material
κ	Constant of Von-Karman and
λ	Porosity
ξ, η	Curvilinear co-ordinates
ρ	Flow density
τ, τ_c	Bed shear stress and critical bed shear stress respectively
ψ	Coefficient related to the diffusion of sediment particles
ω	Turbulence specific dissipation rate
$\boldsymbol{\tau}$	Viscous stress tensor

Acronyms and abbreviations

BWDB	Bangladesh Water Development Board
CEGIS	Center for Environmental and Geographic Information Services
d/s	Downstream of a river
DEM	Digital Elevation Model
FAP-6	Flood Action Plan 6
m ³ /s	Cubic meter per second
PWD	Public Works Department
u/s	Upstream of a river
Dry period	January to March
Wet period	June to August
2D	Two-dimensional
3D	Three-dimensional
OpenFOAM	Open Field Operation and Manipulation
PISO	Pressure Implicit with Splitting of Operator
PIV	Particle Image Velocimetry
CFL	Courant–Friedrichs–Lewy
FVM	Finite Volume method

Curriculum Vitae

Name SHAMPA

Citizenship People's Republic of Bangladesh

Date of Birth November 13, 1988

Key Qualification

Ph.D. Student (2016 ~ 2019) Department of Civil and Earth Resources Engineering, Kyoto University, Kyoto, Japan

M. Sc. (part-time, 2011 ~ 2015) Department of Water Resources Engineering Bangladesh University of Engineering and Technology (BUET), Dhaka, Bangladesh

B. Sc. (2006 ~ 2011) Department of Water Resources Engineering Bangladesh University of Engineering and Technology (BUET), Dhaka, Bangladesh

Key Employment Record

From 2013 to Present (Study Leave during Ph.D.) Faculty member, Institute of Water and Flood Management (IWFm), Bangladesh University of Engineering and Technology (BUET), Dhaka, Bangladesh

From February 2011 to 2013 Employer: Center for Environmental and Geographic Information Services, Dhaka, Bangladesh

Paper based on the Thesis

Shampa, Hasegawa Y., Nakagawa H., Takebayashi H. and Kawaike K., (2017), Dynamics of Sand Bars in Braided River : A Case Study of Brahmaputra-Jamuna River, *Journal of Japan Society for Natural Disaster Science*, Vol.36 (Special Issue), September 2017, pp.123–137.

Shampa, Hasegawa Y., Nakagawa H., Takebayashi H. and Kawaike K., (2017), Switching of Bifurcation to Single Channel : Case of a Sand Bed Braided River, *In: E-proceedings of the 37th IAHR World Congress*, August 13-18, 2017, Kuala Lumpur, Malaysia, pp. 113–120.

Hasegawa, Y., Shampa, Hashizaki, T., Takebayashi, H., and Nakagawa, H. (2017). “Experimental Study on Sediment Deposition Effect of Slit Type Spur Dikes.” 6th International Conference on Water & Flood Management (ICWFM-2017), A. Haque, ed., Dhaka, 135.

Roy B., Shampa, Dustegir M.M., M., Islam M.R., Haque S., Rahman M.M., and Haque A., (2017), Simulation of Flow Field along the Jamuna River in Bangladesh, *In: Proceedings of 3rd International Conference on the Status and Future of the World’s Large Rivers*, April 18-21, 2017, New Delhi, India, pp. 2–3.

Shampa, Hasegawa Y., Nakagawa H., Takebayashi H. and Kawaike K., (2017), Numerical Simulation of River Bed Deformation due to Unsteady Flow of Large Sand-Bed Braided, *Annals of Disaster Prevention Research Institute, Kyoto Univ.*, No.60 B, June, 2017, pp.737-745.

Shampa, Hasegawa Y., Nakagawa H., Takebayashi H. and Kawaike K., (2018), Defining Appropriate Boundary Conditions of Hydrodynamic Model from Time Series Data, *Annals of Disaster Prevention Research Institute, Kyoto Univ.*, No.61 B, June, 2018, pp.648-654.

Shampa, Hashizaki T., Hasegawa Y., Nakagawa H., Takebayashi H. and Kawaike K., (2018), Installation effects on three-dimensional flow characteristics in a slit-type permeable spur dike field, *Journal of Hydraulic Engineering of ASCE* (under review).

Shampa, Hasegawa, Y., Takebayashi, H., & Nakagawa, H. (2017), Effectiveness of slit type permeable spur dike field on braided channel for river bank protection. In A. Haque (Ed.), *7th International Conference on Water & Flood Management (ICWFM-2019)* (submitted).